

SOLIDIFICATION KINETICS IN UNDERCOOLED PURE IRON AND IRON-BORON ALLOYS UNDER DIFFERENT FLUID FLOW CONDITIONS

DISSERTATION

zur

Erlangung des Grades

eines Doktors der Naturwissenschaften

in der Fakultät für Physik und Astronomie

der Ruhr-Universität Bochum

von

Christian Karrasch

aus

Bonn

Bochum 2016

1. Gutachter: Prof. Dr. Dieter M. Herlach
2. Gutachter: Prof. Dr. Kurt Westerholt

Datum der Disputation: 28. Januar 2016

TO KAROLINA AND MY FAMILY

*We are at the very beginning of time for human race.
 It is not unreasonable that we grapple with problems.
 But there are tens of thousands of years in the future.
 Our responsibility is to do what we can, learn what we can,
 Improve the solutions, and pass them on.*

RICHARD P. FEYNMAN (1918-1988)

CONTENTS

INTRODUCTION.....	1
1 THEORETICAL BACKGROUND: SOLIDIFICATION IN UNDERCOOLED LIQUIDS.....	5
1.1 Thermodynamics: Undercooling and Driving Force for Solidification.....	6
1.2 Thermodynamics of Binary Systems	7
1.3 Nucleation Theory	8
1.3.1 Homogeneous Nucleation.....	8
1.3.2 Heterogeneous Nucleation.....	13
1.3.3 Nucleation in Alloys	14
1.4 Solid-Liquid Interface	15
1.5 Local Equilibrium to Non-Equilibrium Solidification	18
1.5.1 GIBBS-THOMSON Effect and the Morphology of the Solid-Liquid Interface	18
1.5.2 Attachment Kinetics at the Solid-Liquid Interface	20
1.5.3 Solute Trapping.....	22
2 DENDRITIC GROWTH MODEL	25
2.1 Sharp Interface Model for Dendritic Solidification.....	26
2.2 Influence of Convection on Dendrite Growth	32
3 EUTECTIC GROWTH MODEL.....	35
3.1 Current Model for Concentrated Alloys with Non-Linear Phase Diagram (NLPD)	37
3.2 Model of Li and Zhou (LZ) for Dilute Alloys with Linear Phase-Diagram (LPD)	40
3.3 Kinetic Liquidus Slopes for Large Undercoolings	41
4 EXPERIMENTAL METHODS	45
4.1 Electromagnetic Levitation (1g-EML).....	45
4.2 Electromagnetic Levitation under Reduced Gravity (μ g-EML)	48
4.3 Melt-Fluxing in a Static Magnetic Field (MF)	51
4.4 Infrared Camera (IRC) versus High-Speed Camera (HSC).....	53
4.5 Microstructure Analysis.....	55

5	SAMPLE SYSTEM: IRON-BORON.....	57
5.1	Phase Diagram, Material Parameter, and Crystallographic Structure.....	57
5.2	Sample Material and Preparation for Experiments and Microstructure Analysis.....	59
6	EXPERIMENTAL RESULTS AND DISCUSSION	61
6.1	Growth Morphology and Microstructure.....	61
6.2	Bent Dendrite Growth.....	65
6.2.1	Bent growing dendrites under reduced gravity conditions	65
6.2.2	Microstructure of bent dendrites	66
6.2.3	Discussion	66
6.2.4	Conclusion.....	68
6.3	Dendrite Growth Velocity V versus Undercooling ΔT	69
6.3.1	Pure Fe.....	70
6.3.2	Fe-1 at.% B.....	76
6.3.3	Fe-5 at.% B.....	83
6.3.4	Fe-10 at.% B	86
6.4	Eutectic composition Fe-17 at.% B.....	89
6.4.1	Eutectic Dendrite Growth Velocities $v(\Delta T)$	89
6.4.2	Microstructure Analysis of Fe-17 at.% B.....	96
	SUMMARY	97
A	APPENDIX.....	101
A.1	Video Analysis of Dendrite Growth Velocity	101
	BIBLIOGRAPHY	103
	Publication List	112
	Curriculum Vitae	114
	Acknowledgments	113

INTRODUCTION

Our daily life is surrounded by materials which were formed during phase transformation, such as ice, steel constructions of buildings, and even crack resistant display-glass of smartphones. Since the Bronze Age (4000 BC – 1200 BC) followed by the Iron Age (1200 BC – 500 BC) the use of solidification techniques, alloying and casting play a key role in human history. For example the legendary Damascus steel swords are known for their sharpness and strength. This material culture of mankind is culminated in our today's high technology society. However, not before the first half of the 20th century scientists tried to develop a physical understanding how the material properties were related to the conditions of solidification.

In the case of metals the major growth mode is *dendritic solidification* (tree-like). “Worldwide, as many as 10 billion metallic dendrites are produced in industry every second” [1]. In other words, to understand and to control dendritic solidification processes is of great economic interest. Particularly the initial process conditions determine the evolution of the microstructure and therefore influence the final product of solidification. The main challenge is to design materials directly from the melt with specific material properties without expensive post-processing. Therefore it is essential to have a fundamental physical understanding of the complex mechanism of dendritic solidification which is mainly governed by the heat and mass transport at the moving solid-liquid interface. Even though dendrite growth is an experimentally and theoretically well investigated process, there are still many open questions in this field of solidification science [2].

Since ISAAC NEWTON (1643-1727) studied snowflakes under a microscope the process how dendritic structures form out of chaos is not fully understood. In particular, side branches of dendrites have a self-similar pattern and fractal geometry. NEWTON investigated ice crystals and their identification which were formed in clouds under various environmental conditions. In order to understand the laws of nature he supposed an underlying surface order to explain this manifold phenomenon. In general, the mechanism of dendritic growth is driven by temperature and or concentration gradients at the solid-liquid interface. Initially solid fluctuations into the liquid at the growth front of a crystal are able to grow faster as other parts. Those tips dash forward becoming a dendritic stem which can build further side branches leading to a network structure with residual liquid in between. In detail, dendrite growth is a complex process dealing with many aspects as follows:

- Diffusion of heat and mass
- Solubility of the chemical components in the solid
- Atomic attachment kinetics at the interface between liquid and solid

- Shape, curvature and stability of the interface
- Surface energy of the interface and its anisotropy
- Concentration and thermal convection.

In order to understand dendritic solidification kinetics in more detail it is important to measure key factors as for instance the growth velocity V over a wide range of magnitude and therefore verify dendrite growth models. Non-equilibrium rapid solidification offers this possibility. In 1724 GABRIEL FAHRENHEIT discovered an effect called *undercooling* ΔT . He observed water droplets which stayed liquid below their freezing temperature of 0 °C. In a clean environment a high purity material remains liquid in a metastable undercooled state unless hundreds of atoms cluster statistically together and form a stable nucleus which starts to grow. Statistical nucleation theory tells you which phase nucleates with a certain possibility. Thermodynamics defines the equilibrium state of coexisting liquid and solid phase whereas growth theory describes the kinetics of growth. The opportunity of undercooling offers to study dendritic solidification far from thermal equilibrium over a wide range of undercooling. The dependence of $V(\Delta T)$ varies for metals from cm/s up to several m/s depending on the undercooling from 50 K to above 300 K prior to equilibrium solidification.

Rapid solidification in undercooled melts can be investigated by containerless experimental methods where heterogeneous nucleation on container walls is completely avoided which otherwise limits the undercoolability of a melt. For instance electromagnetic levitation (EML) technique [3] is applied to undercool droplets of metallic melt accessible for *in-situ* diagnostics of the solidification process. During the transformation of the undercooled liquid phase into the solid phase latent heat is released leading to a visible contrast between liquid and solid which is recordable by a high-speed video camera. In the past infrared cameras were too slow for observing crystal growth in metals. Recent developments make fast infrared cameras available. As feasibility study within this thesis an infrared camera is used to evaluate it as a powerful tool for new findings. This is especially interesting for low melting materials at small undercooling with weak contrast in visible light.

Understanding industrial multicomponent alloys is a very complex issue. To study dendritic growth and investigate effects of solidification, a binary system like Fe-B is used as a model system. Moreover the knowledge of the solidification behaviour and thermodynamic properties of Fe-B is of interest in several fields of material engineering. For example, Fe-B is a subsystem of the Nd-Fe-B alloys with superior magnetic properties. Also the high modulus TiB₂-reinforced steel composite is based on the Fe-B-Ti ternary alloy. Furthermore B is used for hardenability of steels and even to form amorphous alloys. In this thesis the growth kinetics of pure Fe and Fe-B alloys are investigated by measuring the growth velocity V as a function of undercooling ΔT . In

general, dendritic solidification in undercooled melts is mainly governed by nucleation and crystal growth. Namely the interfacial energy, the interfacial mobility and the crystal anisotropy are key factors for dendrite growth kinetics and dendritic morphology which will be investigated in the present work by measuring and modelling $V(\Delta T)$. The anisotropic nature of the interfacial free energy and atomic attachment kinetics lead to a preferred growth direction of the dendritic crystal. In the case of a cubic crystal structure like Fe the $\langle 100 \rangle$ –direction is typical [4]. The knowledge of the growth morphology is crucial to analyse EML dendrite growth videos where only the intersection of the solidification front with the spherical sample surface is visible. In detail, the pattern visible on the surface is the intersection of a growing octahedron of which the center is placed on the sample surface [5]. The vertices correspond to the primary dendrite tips and the edges correspond to the secondary side branches.

Pure Fe melts crystallize primarily in body-centered cubic phase. The Fe-B system is an incongruent melting metal-metalloid alloy at low B concentrations. Starting with pure Fe manifold phenomena can be studied by stepwise adding B. In general, B is poorly soluble in Fe [6] and has a low equilibrium partition coefficient $k_E \ll 1$. During solidification the different solubility of solvent in liquid and solid phase leads to a pile up of B concentration and a concentration gradient in front of the moving interface. Due to the low solubility of B in Fe the dendrite growth velocity is limited by the diffusion of B in liquid Fe. At low undercoolings this effect dominates, and slows down dendrite growth velocity leading to a Fe-B solid solution. For larger undercoolings at low B concentration (such as Fe-1 at.% B) an effect called *solute trapping* is expected. At a certain undercooling the rapid propagation of the solid-liquid interface leads to entrapment of solute beyond its chemical equilibrium solubility. B is incorporated above its solubility limit in Fe leading to a supersaturated solid solution. This non-equilibrium phenomenon (solute trapping) can be explained and treated by the *sharp interface model* taking into account a velocity dependent partition coefficient $k(V)$.

At higher B concentrations the growth velocity is expected to slow further down. Additionally the primary crystallization mode changes from body-centered cubic (bcc) to face-centered cubic (fcc) structure (Fe-5 and 10 at.% B). In this case a phase competition in nucleation and growth takes place between bcc and fcc structure. Measurements of dendrite growth velocity as a function of undercooling may help to give a phase discrimination.

By further increasing the B concentration (Fe-17 at.% B) the single phase dendritic mode changes to the multiphase *eutectic growth* mode in which two different crystallographic phases are formed simultaneously during solidification. The eutectic composition Fe-17 at.% B is a metallic glass former which gives rise to investigations of glass formation. Even nucleation and crystallization may be suppressed by applying sufficiently high external cooling rates. However

the glass transition temperature T_g of Fe-17 at.% B is about 800 K [7] and cannot be reached by the experimental methods applied within this thesis. Amorphous Fe-17 at.% B may be prepared at much higher cooling rates ($\sim 10^6 \text{ K s}^{-1}$).

Melt *convection* is an important aspect which affects dendritic growth at high *fluid flow* velocities. In earth laboratory, high electromagnetic fields are necessary in a terrestrial 1g-EML to lift the sample against gravity. Therefore electromagnetic stirring induces fluid flow which affects the heat and mass transport at the solid-liquid interface during solidification. This influence of forced convection changes dendritic growth morphology and growth velocity, especially if the fluid flow velocity is in the same order of magnitude or larger than the solidification velocity itself. The present research shows unexpected *bent dendrite growth* under different fluid flow conditions which was accepted for publication [8]. This phenomenon has been observed *in-situ* for the first time in solidifying metals during levitation. Bent dendrite growth appears at low undercooling for all investigated dendritic growing alloys (Fe-1, 5, and 10 at.% B). In the present work the influence of convection on growth velocity and morphology is investigated by applying different experimental fluid flow conditions:

- 1g-EML (0.3 m/s) [9]
- μg -EML (0.05 m/s) [9] under reduced gravity during parabolic flight
- Melt-fluxing experiments in a static magnetic field (0 – 6 T).

God created the solids,

The Devil their surfaces.

WOLFGANG PAULI (1900-1958)

1 THEORETICAL BACKGROUND: SOLIDIFICATION IN UNDERCOOLED LIQUIDS

In this chapter the thermodynamic background is described in order to understand non-equilibrium rapid solidification processes. Together with chapter 2 *dendritic growth* and chapter 3 *eutectic growth* it builds the fundament to interpret the experimental results. For further and more detailed explanations the author refers to i.e. the book SOLIDIFICATION by J. A. DANTZIG and M. RAPPAZ [10] or METASTABLE SOLIDS FROM UNDERCOOLED MELTS by D.M. HERLACH, P. GALENKO and D. HOLLAND-MORITZ [11].

Thermodynamics characterizes the equilibrium state of liquid and solid phase. However a system in thermodynamic equilibrium would not change in a macroscopic view. There has to be a deviation from equilibrium, otherwise solid and liquid will coexist at the melting temperature with no moving of the phase boundary. For instance, lowering the temperature of the system results in an expansion of the stable phase (solid) at the expense of the unstable phase (liquid). In other words, the crystal grows into the melt. In this case the liquid at the interface is *undercooled*. Rapid Solidification from a deeply undercooled liquid state is a non-equilibrium process which is governed by nucleation and crystal growth. In order to initiate solidification a nucleus of critical size has to be formed in the undercooled melt. *Nucleation* theory predicts which crystallographic phase is selected and defines the probability of atoms which statistically cluster together to form a nucleus. After a nucleus of critical size is formed it becomes stable by further growth which is described by *crystal growth* theory. Subsequently, the solid state expands by crystal growth that is either *dendritic* or *eutectic*. The driving force for solidification is the GIBBS free energy which will be defined in this chapter. In general, with increasing undercooling the driving force for solidification increases which leads to a faster growth of the solid phase.

1.1 Thermodynamics: Undercooling and Driving Force for Solidification

The equilibrium state of a thermodynamic system can be described by the thermodynamic potential. In case of choosing temperature T , pressure p , and particle number N , as thermodynamic variables the GIBBS free energy $G(p, T, N)$ is the thermodynamic potential. It describes the changes of the system is the GIBBS free energy $G(p, T, N)$. The GIBBS free energy G is defined by:

$$G(p, T, N) = \underbrace{U(S, V, N) + p \cdot V}_{H(S, N, p)} - T \cdot S(U, V, N) = H - T \cdot S,$$

where U is the internal energy of the system, V the volume, S the entropy, and H the enthalpy. Figure 1-1 shows the GIBBS free energy G as a function of temperature T at constant pressure p and particle number N for the liquid and solid phase. The GIBBS free energy of the liquid phase $G_L(T)$ intersects the GIBBS free energy of the solid $G_S(T)$ at the equilibrium melting temperature T_E . Above this temperature the liquid phase is thermodynamically preferred and stable. Below T_E the liquid phase becomes metastable which is called *undercooled state* and indicated by the dashed part of the curve. The enthalpy difference $\Delta G_{LS}(T) = G_S(T) - G_L(T) < 0$ is the driving force for crystallization which increases with rising undercooling. $\Delta G_{LS}(T) = \Delta H_{LS}(T) - T\Delta S_{LS}(T)$ can be expressed in the case of a monoatomic system by the enthalpy difference $\Delta H_{LS}(T)$ and the entropy difference $\Delta S_{LS}(T)$ as followed:

$$\Delta G_{LS}(T) = \underbrace{\Delta H_f - \int_T^{T_L} \Delta C_{p,LS}(T) dT}_{\Delta H_{LS}(T)} - T \left(\underbrace{\Delta S_f - \int_T^{T_L} \frac{\Delta C_{p,LS}(T)}{T} dT}_{\Delta S_{LS}(T)} \right),$$

where the enthalpy of fusion $\Delta H_f = H_L(T_E) - H_S(T_E) = T_E \Delta S_f$ and $\Delta C_{p,LS}(T) = C_L^p(T) - C_S^p(T)$ is the difference of the specific heat of the liquid $C_L^p(T)$ and solid phase $C_S^p(T)$. The specific heat $C_L^p(T)$ of an undercooled liquid is experimentally difficult to measure but essential for calculating the driving force of solidification. In 1950 TURNBULL [12] suggested a simple linear approximation. In that case the difference of the specific heat of the liquid and solid can be neglected ($\Delta C_{p,LS}(T) = 0$). As a consequence of this simplification ΔH_{LS} and ΔS_{LS} become temperature independent which leads to:

$$\Delta G_{LS}(T) = \frac{\Delta H_f}{T_E} (T_E - T). \quad (1)$$

This is especially valid for pure metals where $\Delta C_{p,LS}$ is small [13] but also for mixed phases at low undercoolings.

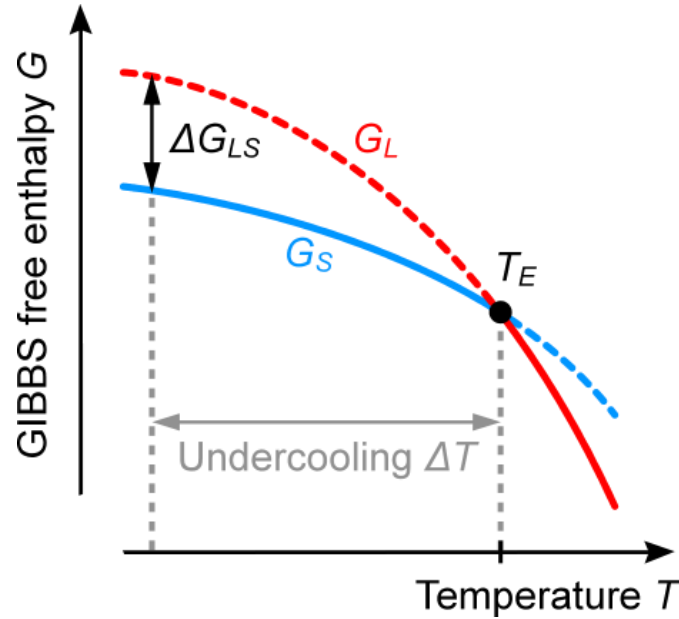


Figure 1-1: The GIBBS free energy G as a function of the temperature T plotted for a liquid phase G_L (red) and a solid phase G_S (blue). The equilibrium melting point T_E is defined by the intersection of G_L and G_S . For a given undercooling ΔT the driving force for solidification is the GIBBS free energy difference ΔG_{LS} .

1.2 Thermodynamics of Binary Systems

In the case of a binary alloy the thermodynamic state of a system can no longer be described by only the pressure p , temperature T and number of particles N . The different types of particles (molecules or atoms) interact with each other. Therefore the GIBBS free energy becomes also dependent on the composition as an additional thermodynamic variable. Furthermore the total GIBBS free energy G of the binary system is not only the sum of the GIBBS free enthalpies G_1 and G_2 of each system. An additional free enthalpy term of mixing ΔG_{mix} has to be taken into account.

Let a binary alloy be consisting of components N_1 and N_2 in atomic percent (at.%). The composition of both can be characterized by the concentration $c_1 = N_1/N$ and $c_2 = 1 - c_1$ with the total number of the particles $N = N_1 + N_2$. Consequently the GIBBS free energy of the binary system can be written as:

$$G(T, p, c_1, c_2) = c_1 G_1(T, p) + c_2 G_2(T, p) + \Delta G_{mix}(T, p, c_1, c_2),$$

where $\Delta G_{mix} = \Delta H_{mix} - T\Delta S_{mix}$ is the GIBBS free energy of mixture, ΔH_{mix} the enthalpy of mixture, and ΔS_{mix} the entropy of mixture.

In a binary system the minor component is called the *solute*, while the major component is the *solvent*. The crystal structure of the composition is not strictly the same as of each component. Moreover if elements are not soluble, the mixture has to implement vacancies or interstitials to build a crystal structure. In the case of Fe-B for small B concentration the crystal forms a solid

solution. At large undercoolings the B is incorporated beyond its equilibrium solubility, known as *solute trapping* leading to a supersaturated crystal which will be explained in chapter 1.5.2.

To summarise, a binary system can be described by the GIBBS free energy $G(T, p, c_1, c_2)$. From a macroscopic thermodynamic point of view an undercooled liquid state should not exist because the liquid state is energetically unfavourable below the equilibrium temperature T_E . Even though, the solid state is energetically preferred, there has to be a certain mechanism which has to initiate the transformation from liquid to solid. This process of nucleation for solidification will be described in the following subchapter.

1.3 Nucleation Theory

Nucleation initiates of solidification and will be described in this subchapter. In 1926 first attempts to describe the kinetics of nucleation were developed by VOLMER and WEBER about condensation of supersaturated vapour [14]. BECKER and DÖRING extended this model in 1935 [15]. Later 1949, TURNBULL and FISHER [16] developed modified models to analyze nucleation of a crystal in an undercooled melt.

Below the equilibrium melting point T_E the GIBBS free energy G of a liquid phase decreases with increasing temperature and the melt should transform into the energetically preferred solid phase. As described in the previous section the driving force for solidification increases with rising undercooling. Obviously a free energy barrier exists to initiate solidification otherwise undercooling would not be possible. Consequently the undercooling of liquids cannot be explained by thermodynamics alone. Following thermodynamics in a liquid phase, the atoms move randomly driven by kinetic energy (temperature). Due to statistical fluctuations atoms collide and may spontaneously build an embryo which may form a nucleus. By further growth the nucleus becomes stable.

Classical nucleation theory distinguishes between *homogeneous* and *heterogeneous* nucleation. Homogeneous nucleation is an intrinsic mechanism where atoms build statistically a cluster which is able to grow. This is governed only by the thermodynamic properties of the system itself. Heterogeneous nucleation in contrast is an extrinsic process initiated by an inhomogeneity like a foreign particle or container wall acting as nucleation sites. For achieving deep undercoolings the heterogeneous nucleation sites need to be minimized. This can be realized by using high-purity materials under clean experimental conditions.

1.3.1 Homogeneous Nucleation

The homogeneous nucleation in a liquid is an intrinsic process. The temperature driven motion of atoms leads to statistical density fluctuations in the liquid which built solid-like clusters. Above the equilibrium melting point T_E those clusters decompose and disappear. In the case of

an undercooled melt at temperatures below T_E the GIBBS free energy of the solid phase G_S becomes smaller as for the liquid phase G_L . Consequently, the free enthalpy difference $\Delta G_{LS} = G_S(T) - G_L(T)$ is negative. This implies that the transformation from a metastable undercooled liquid into solid phase is energetically preferred. Obviously it exists an energy barrier which the solid-like cluster has to overcome to initialize solidification otherwise the metastable undercooled state would not be possible. In fact, the formation of such a cluster means that energy is needed to build up an interface between solid and liquid with an interfacial energy σ_{LS} . For simplicity consider a spherical like geometry of clusters. Therefore the energy balance $\Delta G(r)$ during the formation of such a spherical solid-like cluster in an undercooled melt can be written as a function of the cluster radius r . In total, $\Delta G(r)$ is the sum of a volume $\Delta G_V(r)$ and surface contribution $\Delta G_A(r)$:

$$\Delta G(r) = \Delta G_V(r) + \Delta G_A(r) = -\frac{4}{3}\pi r^3 \Delta G_{LS} + 4\pi r^2 \sigma_{LS}. \quad (2)$$

Figure 1-2 shows the GIBBS free energy difference ΔG as a function of the radius r . The volume contribution of the free enthalpy is proportional to r^3 whereas the surface contribution dependence is r^2 . This means ΔG has a maximum at ΔG^* at a critical radius r^* . Clusters smaller than r^* are unstable. ΔG_V is negative which means an energy benefit for the system to build a solid-like cluster. However there is an energy barrier ΔG^* to overcome such a cluster. Even as the cluster gains energy through further growth larger as r^* it stays metastable. The cluster becomes stable if it reaches $r_0 = 1.5 \cdot r^*$ since the free enthalpy balance becomes negative.

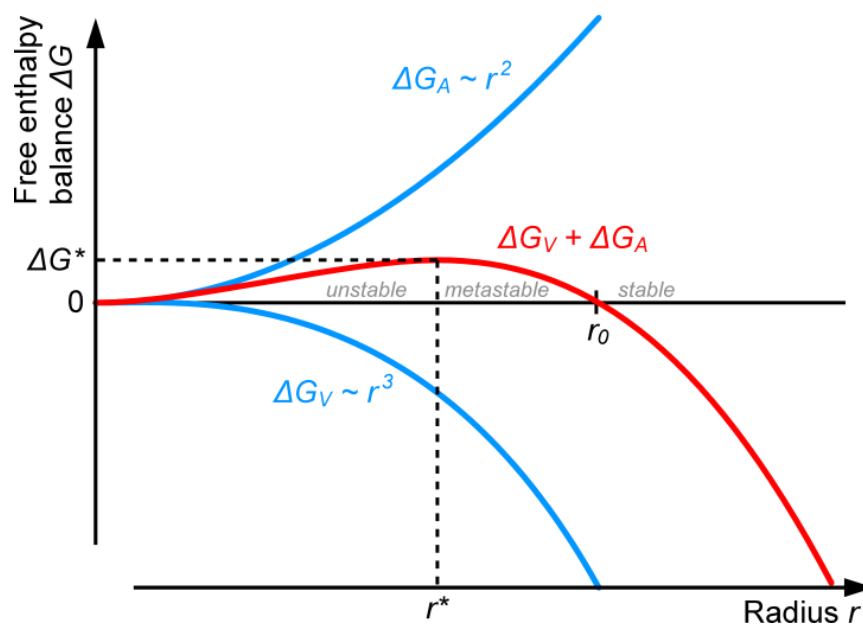


Figure 1-2: GIBBS free energy difference ΔG as a function of the radius r . The volume contribution ΔG_V is negative and proportional to r^3 whereas the surface contribution ΔG_A is positive and proportional to r^2 . The activation energy ΔG^* is necessary for the formation of a critical nucleus with the radius r^* .

The critical radius r^* is given by the maximum of equation (2) to:

$$r^* = -2 \frac{\sigma_{LS}}{\Delta G_{LS}}.$$

As an example, for pure Fe with a typical undercooling for homogeneous nucleation of $\Delta T = 420 \text{ K}$, with the latent heat of fusion $\Delta H_f = 1737 \text{ J/cm}^3$, the surface energy $\sigma_{LS} = 204 \cdot 10^{-7} \text{ J/cm}^2$, and the melting temperature $\Delta T_E = 1811 \text{ K}$ the critical radius can be calculated by combining equation (1) and (2):

$$r^* = \frac{2\sigma_{LS}T_E}{\Delta H_f \Delta T} = \frac{2 \cdot (204 \cdot 10^{-7} \text{ J/cm}^2) \cdot (1811 \text{ K})}{1737 \text{ J/cm}^3 \cdot 420 \text{ K}} \approx 1.01 \text{ nm}.$$

The lattice constant of body-centered cubic (bcc) Fe crystal is $a_0 = 0.28665 \text{ nm}$. Therefore the volume of a unit cell and the volume of the critical nucleus are:

$$V_{unit \ cell} = (a_0)^3 = 2.36 \cdot 10^{-23} \text{ m}^3$$

$$V_{r^*} = \frac{4}{3} \pi (r^*)^3 = 435.19 \cdot 10^{-23} \text{ m}^3.$$

Consequently, the critical nucleus is built of $V_{r^*}/V_{unit \ cell} = 184$ unit cells. Each unit cell consists of 4 atoms which means a critical nucleus has in total 688 Fe atoms.

To build such an critical nucleus of $r^* \approx 1 \text{ nm}$ consisting of $n = 688$ atoms an activation energy of

$$\Delta G^* = \frac{16\pi}{3} \frac{\sigma_{LS}^3}{\Delta G_{LS}^2} \approx 22 \text{ eV}$$

is needed. This energy barrier explains why metallic melts can be undercooled to several hundred Kelvin prior to equilibrium solidification before a stable nucleus appears. For comparison, if the temperature is $1500 \text{ }^\circ\text{C}$ the thermal energy of an atom according to the equipartition theorem with its average translational kinetic energy $\frac{3}{2} k_B T$ is about 0.23 eV .

To rate the probability of nucleation VOLMER and WEBER developed a model for condensation of supersaturated vapour [14]. This model is based on the assumption that clusters grow or decay by the attachment or detachment of atoms to the nuclei. They considered the number of clusters N_n containing n atoms per unit volume V_{mol} at a temperature T which can be described by the BOLTZMANN statistics:

$$N_n = \frac{N_A}{V_{mol}} \exp\left(-\frac{\Delta G(n)}{k_B T}\right),$$

where $k_B = R/N_A = 1.3806488(13) \times 10^{-23} J \cdot K^{-1}$ is the BOLTZMANN constant while $R = 8.3144621(75) J \cdot K^{-1} \cdot mol^{-1}$ is the universal gas constant, $N_A = 6.02214129(27) \times 10^{23} mol^{-1}$ the AVOGADRO constant, and V_{mol} the molar volume. $\Delta G(n)$ corresponds to the energy required to build a cluster consisting of n atoms. Obviously the probability to find small clusters is higher than to find large clusters. However for $n \rightarrow \infty$ the function increases exponentially which is non-conform to the conservation number of particles. Therefore VOLMER and WEBER proposed that the clusters which reach the critical size n^* will grow further through attachment of particles. In other words those clusters are extracted from the ensemble which means that the distribution function aborts at n^* . This behaviour is illustrated in Figure 1-3.

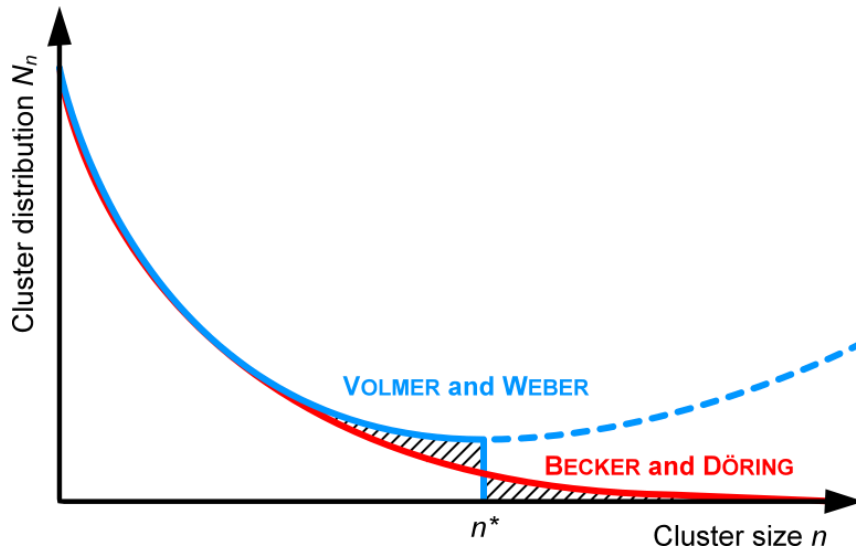


Figure 1-3: Cluster distribution function N_n as a function of the cluster size with n particles according to the model of VOLMER and WEBER (blue curve) [14] and BECKER and DÖRING (red curve) [15]. The shaded areas are equal according to the particle conservation law.

However even a post-critical cluster (metastable) is able to shrink by detachment of atoms with a certain possibility. Therefore BECKER and DÖRING [15] suggested a cluster distribution function which respects the particle conservation law and converges for large clusters above the critical size n^* which is also shown in Figure 1-3.

Consequently the steady-state (quasi stationary) nucleation rate $I(t)$ according to BECKER and DÖRING is given by the frequency for building clusters with a radius $r > r^*$ or with atoms $n > n^*$ which can be expressed by:

$$I(t) = K_{n^*}^+ N_{n^*}(t) - K_{n^*+1}^- N_{n^*+1}(t),$$

where N_{n^*} and N_{n^*+1} are the number of clusters containing n^* respectively $n^* + 1$ atoms. The factor $K_{n^*}^+$ is the probability for clusters converting from n^* to the size of $n^* + 1$ atoms. In the contrary $K_{n^*+1}^-$ describes the detachment from a $n^* + 1$ cluster to a cluster with n^* atoms. In particular, the number of clusters $N_n(t)$ with n atoms at a time t is given by the nucleation rate:

$$I_{SS}^{hom} = K_{n^*}^+ \frac{N_A}{V_{mol}} \Gamma_z \exp\left(-\frac{\Delta G^*}{k_B T}\right).$$

The ZELDOVICH-factor Γ_z takes into account the post-critical clusters $n > n^*$ and is defined as the second derivation of ΔG for $n = n^*$ as follows:

$$\Gamma_z = \sqrt{\frac{\Delta G^*}{3\pi k_B T n^{*2}}}.$$

The transformation from a liquid to a solid state needs a thermally activated atomic diffusion process. Therefore BECKER [17] assumed a diffusion controlled attachment of atoms to a cluster. In addition, TURNBULL and FISHER [16] suggested for attaching an atom to a cluster the atom has to diffuse through the solid-liquid interface which means it has to overcome an activation barrier ΔG_a for thermally activated atomic diffusion. In this case, the attachment rate $K_{n^*}^+$ can be described by the Boltzmann statistics:

$$K_{n^*}^+ = 4n^{*\frac{2}{3}}v_0 \exp\left(-\frac{\Delta G_a}{k_B T}\right),$$

where $v_0 = k_B T/h$ is the vibration frequency of the atoms with $h = 6.62606957 \times 10^{-34} \text{ J} \cdot \text{s}$ the PLANCK constant. The factor $4n^{*\frac{2}{3}}$ takes into account that the attachment of atoms to the cluster is only possible at the surface of the nucleus.

Consequently the nucleation rate can be written as:

$$I_{SS}^{hom} = 4n^{*\frac{2}{3}}v_0 \frac{N_A}{V_{mol}} \Gamma_z \exp\left(-\frac{\Delta G_a}{k_B T}\right) \exp\left(-\frac{\Delta G^*}{k_B T}\right).$$

In order to quantify the nucleation rate I_{SS}^{hom} , ΔG_a is assumed to be equal to the activation energy for atomic diffusion. Furthermore the diffusion coefficient D and the interatomic spacing a_0 are correlated in the following way:

$$\frac{6D}{a_0^2} = v_0 \exp\left(-\frac{\Delta G_a}{k_B T}\right),$$

while the diffusion coefficient D is related to the viscosity $\eta(T)$ by the EINSTEIN-STOKES equation:

$$D = \frac{k_B T}{3\pi a_0 \eta(T)}.$$

Therefore the stationary nucleation rate density I_{SS}^{hom} for homogeneous nucleation can be rewritten as:

$$I_{SS}^{hom}(T) = \frac{8n^{*2/3}k_B T}{\pi a_0^3 \eta(T)} \frac{N_A}{V_{mol}} \Gamma_z \exp\left(-\frac{\Delta G^*}{k_B T}\right).$$

The temperature dependence of the prefactors is negligible small compared to the exponential term which finally leads to an approximation for the nucleation frequency of:

$$I_{SS}^{hom}(T) \approx \frac{10^{36}}{\eta(T)} \exp\left(-\frac{\Delta G^*}{k_B T}\right) m^{-3} s^{-1}.$$

1.3.2 Heterogeneous Nucleation

In the previous section homogeneous nucleation was described as an intrinsic process only dependent on the characteristic thermophysical properties of the sample system itself and the surface energy. On the contrary, *heterogeneous nucleation* is an extrinsic mechanism where foreign phases like impurities or container walls act as nucleation sites.

In 1929 VOLMER [18] described heterogeneous nucleation on a planar substrate which is schematically shown in Figure 1-4. The nucleus has a spherical cap geometry with a wetting/contact angle ϑ which is determined by the balance of the interfacial energies between the undercooled liquid and the substrate γ_{LS} , between the crystal nucleus and the substrate γ_{CS} , and between the undercooled liquid and the crystal nucleus γ_{LC} . In detail, the equilibrium of the interfacial tensions between the undercooled liquid, the substrate, and the solid nucleus, is given by:

$$\gamma_{LS} = \gamma_{CS} + \gamma_{LC} \cos \vartheta.$$

In the case of heterogeneous nucleation, the activation energy ΔG_{het}^* to build a critical nucleus size is reduced by the geometrical factor $f(\vartheta)$ compared to the homogeneous nucleation ΔG_{hom}^* :

$$\Delta G_{het}^* = \Delta G_{hom}^* f(\vartheta),$$

while the catalytic factor $f(\vartheta)$ varies from zero to one ($0 \leq f(\vartheta) \leq 1$).

For complete wetting ($\vartheta = 0$) the catalytic factor becomes zero ($f(\vartheta) = 0$) which means the activation energy $\Delta G_{het}^* = 0$ for nucleation disappears. This leads to epitaxial growth on the substrate at the equilibrium melting point T_E without undercooling. In the other extreme case of non-wetting ($f(\vartheta) = 1$) the substrate has no influence on the nucleation behaviour which means ΔG_{het}^* is equal to ΔG_{hom}^* .

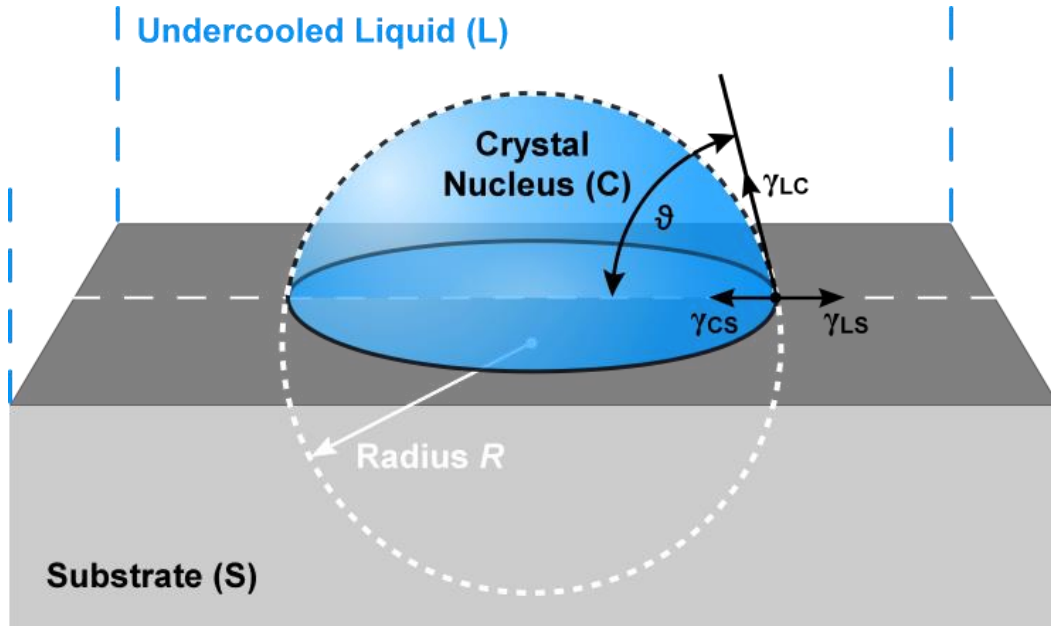


Figure 1-4: Heterogeneous crystal nucleus (C) on a planar substrate (S) in an undercooled liquid (L). The nucleus has a spherical cap geometry with a wetting angle ϑ which is determined by the balance of the interfacial tensions between the crystal nucleus, the undercooled liquid and the substrate.

The steady state nucleation rate for heterogeneous nucleation follows the same formalism as for homogeneous nucleation and is given by:

$$I_{SS}^{het}(T) = \xi \frac{8n^{*2/3} k_B T}{\pi a_0^3 \eta(T)} \frac{N_A}{V_{mol}} \Gamma_z \exp\left(-\frac{\Delta G_{hom}^* f(\vartheta)}{k_B T}\right),$$

where the factor $\xi \leq 1$ limits the number of atoms which are close enough to the solid-liquid interface to participate in a nucleation event. In other words for homogeneous nucleation each atom ($N_{hom} = N_A/V_{mol}$) can act as a starting point for nucleation whereas for heterogeneous nucleation only the atoms close to the substrate $N_{het} = \xi N_{hom}$ act as nucleation sites.

However nucleation on a planar substrate is only a special case for heterogeneous nucleation. In general, the catalytical effect of impurities, rough surfaces or foreign phases lead to heterogeneous initiated solidification before homogeneous nucleation appears. Consequently heterogeneous nucleation limits the undercoolability and is undesirable to investigate rapid solidification in deeply undercooled melts. Large undercoolings can be achieved by the use of high purity materials/environment. In the case of contactless techniques like electromagnetic levitation heterogeneous nucleation on container walls can be completely avoided.

1.3.3 Nucleation in Alloys

So far, the described nucleation theory is only valid in liquids of pure elements. In alloys the concentration has to be taken into account as an additional thermodynamic variable. Therefore the GIBBS free enthalpy of the solid G_S and liquid phase G_L , as well as the entropy of fusion ΔS_f are not only a function of temperature but also depend on the chemical composition.

Furthermore the nucleus composition can vary from the composition of the liquid. This depends on the solubility of its components in the solid. Consequently the concentration changes also the GIBBS free energy difference ΔG_{LS} , the solid-liquid interfacial energy γ_{LS} , and the activation energy barrier ΔG^* for nucleation. Furthermore, in binary alloys, according to SPAEPEN and THOMPSON [19, 20] the concentration dependence in a nucleus is a function of undercooling.

1.4 Solid-Liquid Interface

In the previous sections the undercooled state of a liquid was defined and nucleation was introduced as the initiation for solidification. The physical effects at a solid-liquid interface play a key role to understand rapid crystal growth in an undercooled melt. Therefore this subchapter describes models for a solid-liquid interface and how to calculate the solid-liquid interfacial energy. The motion of this phase boundary and non-equilibrium effects will be discussed in the next subchapter.

Referring to the previous section 1.3 about nucleation the solid-liquid interfacial energy γ greatly affects the activation energy barrier ΔG^* to build a nucleus of critical size. The solid-liquid interfacial energy is defined as the GIBBS free energy necessary for the formation of a solid-liquid interface per unit area ($[\gamma] = J/m^2$). However this physical quantity is not directly accessible to experiments. It has the general form of $\gamma = H - TS$ with an enthalpic and entropic contribution. The interfacial free energy is governed by interplay between the short-range order in the liquid and the crystallographic structure of the solid. In general γ is of anisotropic nature depending on the crystal structure. The underlying surface energy anisotropy leads to preferred growth directions of the solid. In the case of bcc-crystals like γ -Fe the $\langle 100 \rangle$ growth direction is typical [10]. Later on we will see the importance of this fact. To put it more simply, we ignore the anisotropy in the first step by introducing a negentropic (negative entropy) model by SPAEPEN and THOMPSON [21, 22, 19].

Figure 1-5 illustrates a schematically solid-liquid interface based on the model by SPAEPEN and THOMPSON. SPAEPEN assumes a monoatomic system idealized by hard spheres to describe the interface between a close packed crystal/solid plane and a dense random packed liquid phase. The crystalline structure of the solid is characterized by a “maximum short-range density”. For instance the highest possible packing fraction of hard spheres is realized in a fcc crystal. Consider a dense random packing which follows three construction rules:

- (1) Tetrahedral short-range order is preferred,
- (2) Octahedral short-range order is forbidden,
- (3) Density is maximized.

With these rules the boundary layers of the crystal can be constructed. The first two rules originate from FRANK's [23] prediction of a polytetrahedral short range order in metallic melts. The third rule guarantees to minimize the free energy of the interface.

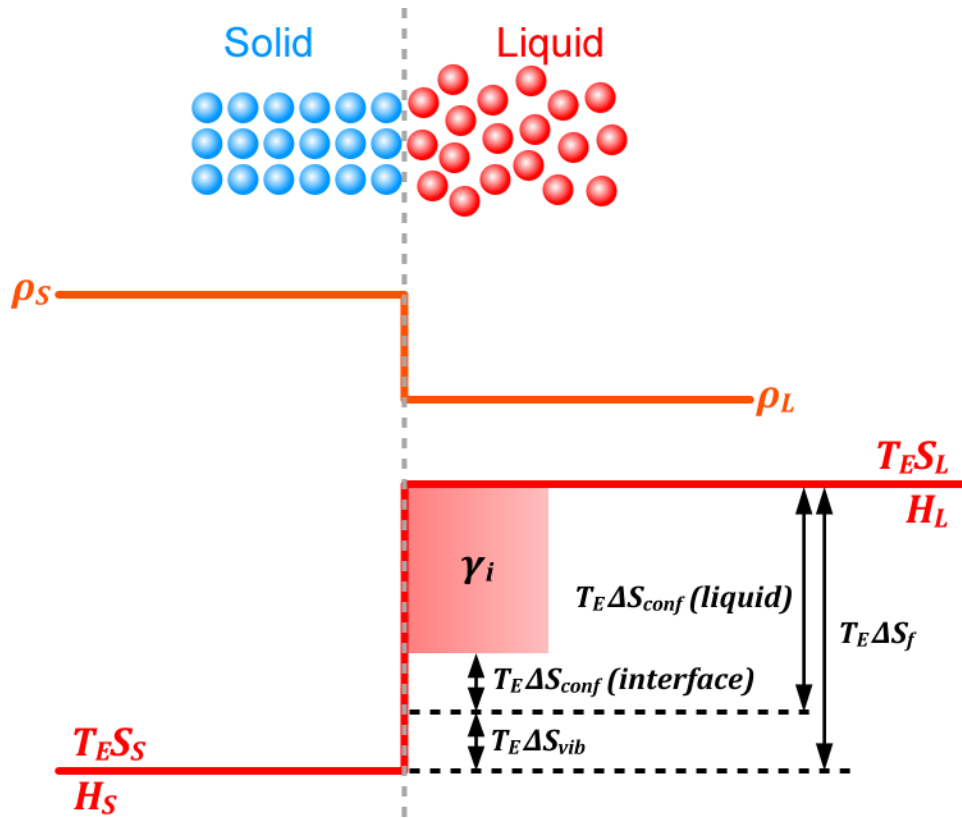


Figure 1-5: Schematic concept of a solid-liquid interface based on to the negentropic model by SPAEPEN and THOMPSON. H is the enthalpy, T_E the equilibrium melting temperature S the entropy, and γ_i the solid-liquid interfacial energy.

The interfacial energy γ is defined as the difference of the GIBBS free energy of a system which contains a solid-liquid interface and a hypothetical reference system. The free energy changes discontinuously at the phase boundary from the bulk solid G_S to the bulk liquid G_L . The density of the solid ρ_S and liquid ρ_L is assumed to be constant with a sharp transition which means discontinues change at the boundary. At the equilibrium melting temperature T_E it follows that:

$$G_L(T_E) = H_L(T_E) - T_E S_L(T_E) = H_S(T_E) - T_E S_S(T_E) = G_S(T_E),$$

$$\Rightarrow \Delta G_{LS}(T_E) = \Delta G_L - \Delta G_S = 0.$$

The enthalpy of fusion is $\Delta H_f = H_L(T_E) - H_S(T_E)$ and the entropy of fusion $\Delta S_f = \Delta H_f / T_E$.

In particular, the entropy of fusion $\Delta S_f = \Delta S_{vib} + \Delta S_{conf}$ consists of two contributions, a vibrational term ΔS_{vib} and an atomic configuration term ΔS_{conf} . Typical values for metals are [21]:

$$\Delta S_f \approx 1.2 k_B \text{ per atom},$$

$$\Delta S_{vib} \approx 0.2 k_B \text{ per atom ,}$$

$$\Delta S_{conf} \approx 1.0 k_B \text{ per atom .}$$

The solid-liquid interfacial energy γ_i at the equilibrium melting temperature T_E per interface atom is given by:

$$\gamma_i(T_E) = T_E [\Delta S_{conf}(liquid) - \Delta S_{conf}(interface)] ,$$

where $\Delta S_{conf}(liquid)$ and $\Delta S_{conf}(interface)$ are the difference in configurational entropy per atom for the reference system and the interface system. Therefore the interfacial energy γ_S per atom in the crystal solid plane is given by:

$$\gamma_S(T_E) = \frac{N_i}{N_S} T_E [\Delta S_{conf}(liquid) - \Delta S_{conf}(interface)] ,$$

where N_i/N_S is the ratio of the numbers in the interface and solid plane. The dimensionless solid-liquid interfacial energy α is defined by:

$$\alpha \equiv \frac{\gamma_S(T_E)}{\Delta H_f} = \frac{N_i}{N_S} \left(\frac{\Delta S_{conf}(liquid) - \Delta S_{conf}(interface)}{\Delta S_f} \right) .$$

The α -factor is determined by the structure of the solid and liquid phase and is independent of the temperature. To put it more simple, the configurational entropy of the interface can be written as:

$$S_{conf}(interface) = S_{conf}(1) \frac{N_1}{N_i} ,$$

while $S_{conf}(1)$ is the configurational entropy per atom of the first interfacial layer which contains N_1 interface atoms. $S_{conf}(1)$ depends on the total number Z of possible configurations to build up the interface in accordance with the construction rules.

Consequently the dimensionless factor α can be calculated for bcc, fcc, and hcp crystal structures [19, 21, 22, 24]:

$$\alpha^{bcc} = 0.70 ,$$

$$\alpha^{fcc,hcp} = 0.86 .$$

This is in good agreement with the results obtained by density functional theory $\alpha^{fcc} = 0.86$ [25] and experimental investigations by HOLLAND-MORITZ [26].

Finally the solid-liquid interfacial energy per surface atom can be calculated with the α -factor by:

$$\gamma_{LS} = \alpha \frac{\Delta S_f \Delta T_E}{(N_A V_{mol}^2)^{1/3}},$$

where V_{mol} is the molar volume and N_L is the AVOGADRO constant.

In the case of pure Fe at the equilibrium melting temperature $\Delta T_E = 1811 K$ the interfacial energy γ_{LS} is about $0.210 J/m^2$ and at an undercooling $\Delta T = 295 K$ about $0.204 J/m^2$ [27]

1.5 Local Equilibrium to Non-Equilibrium Solidification

After the introduction of the solid-liquid interface, the next step is to study the kinetics of the advancement of the solid-liquid interface during solidification.

This subchapter describes the physical effects at a moving solid-liquid interface. In particular, it considers solidification as a moving solid-liquid boundary with respect to the *attachment kinetics* as well as the shape of the boundary (*GIBBS-THOMSON effect*). The deviation from equilibrium arises from gradients in temperature and/or composition. Solidification is driven by heat flow and mass transport (diffusion) into the undercooled melt opposite to directional solidification. The heat flow into the undercooled melt leads to a negative temperature gradient that destabilizes a planar front due to temperature fluctuations. In alloy systems a concentration gradient occurs due to the fact that the solubility of the solvent in the solid state is smaller as in the liquid state. This leads to a concentration pile up at the solidification front and therefore to a concentration gradient into the melt. If the undercooling is large enough and the growth of the solidification front faster as atomic diffuse velocity at the interface, *solute trapping* occurs. The atoms cannot “escape” which leads to an entrapment of solute in the solid state beyond its chemical equilibrium.

The investigated solidification modes within this thesis are *dendritic growth* (chapter 2) and *eutectic growth* (chapter 3) which will be described including theoretical models in separate chapters.

1.5.1 GIBBS-THOMSON Effect and the Morphology of the Solid-Liquid Interface

After introducing the solid-liquid interfacial energy, the shape of the solid-liquid boundary itself is of significant interest and physical meaning. Moreover the morphology of the solidification front not only determines the growth conditions but also the evolution of the microstructure.

Consider a spherical solid particle surrounded by an undercooled melt. The curved solid-liquid interface increases the pressure on the solid particle. Per definition the GIBBS free energy

$G(p, T, N) = U + pV - TS$ includes a pressure-volume term. This means by increasing the pressure leads to a raising of the GIBBS free energy (by $\Delta G = \Delta pV$). This effect is known as capillary or GIBBS-THOMSON effect. As a consequence, the melting point of the curved solid T_E^R will be lower as of than a planar surface T_E^∞ . Small crystals are in equilibrium with their liquid melt at a lower temperature than large crystals. The reduction of the melting point depends on the mean radius of curvature κ and the GIBBS-THOMSON coefficient Γ :

$$\Delta T_R = T_E^\infty - T_E^R = \Gamma \cdot \kappa.$$

where ΔT_R is called the *curvature undercooling* and κ is the curvature of the solid. The GIBBS-THOMSON coefficient Γ is in the order of $10^{-7} Km$ and can be expressed by the solid-liquid interfacial energy:

$$\Gamma = \frac{\gamma_{LS} V_{mol}}{\Delta S_f}.$$

This equation can be written as a capillary length $d_0 = \Gamma C_L^p / \Delta H_f$.

The curvature κ at a point on the interface is defined by:

$$\kappa = \frac{1}{R_1} + \frac{1}{R_2},$$

where the main curvatures R_1 and R_2 are the radii of curvature measured for any orthogonal pair of directions in the surface. For a sphere with radius R as well as for a rotational paraboloid at the tip, the curvature is $\kappa = 2/R$ which leads to:

$$\Delta T_R = \frac{2\Gamma}{R}.$$

Consequently the curvature of the interface reduces the melting temperature at the interface due to the GIBBS-THOMSON effect. Consequently, the interface temperature T_i has to be corrected by the curvature undercooling ΔT_R :

$$T_i = T_E - \Delta T_R.$$

Aside the suppression of the equilibrium melting temperature of a curved interface by the GIBBS-THOMSON effect the interface is undercooled due to atomic attachment kinetics under rapid solidification conditions.

1.5.2 Attachment Kinetics at the Solid-Liquid Interface

The previous sections describe how the interfacial energy between a solid-liquid interface can be calculated and is determined by its shape (GIBBS-THOMSON effect). The next step is to define the kinetic effects for solidification which are governed by the atomic diffusion at the interface border and the ability of atoms to attach to a solid from the undercooled melt.

According to rate theory [28, 29] the velocity $V = \delta(R_S - R_L)$ of a moving solidification front is a result of the attachment rate R_S and detachment rate R_L multiplied by the distance δ between solidified mono layers which is approximated by interatomic spacing. Figure 1-6 illustrates this process.

For a pure system, the correlation between the growth velocity V and the GIBBS free energy ΔG with a temperature T_i at a sharp interface is given by WILSON [30] and FRENKEL [31]:

$$V = f \cdot \underbrace{\delta \cdot \nu}_{\bar{v}_0} \cdot \exp\left(-\frac{\Delta G_a}{RT_i}\right) \cdot \left[1 - \exp\left(\frac{\Delta G(T_i)}{RT_i}\right)\right]. \tag{1.4.2-1}$$

The atoms have to overcome the energy barrier ΔG_a in order to change from liquid into solid state. Thermal atomic motion in the liquid with a vibration frequency ν (approximately 10^{13} Hz) lead to fluctuations which are able to overcome the energy barrier. The accommodation factor $f \leq 1$ is the fraction for available attachment positions in the solid which is typically 1 for metals.

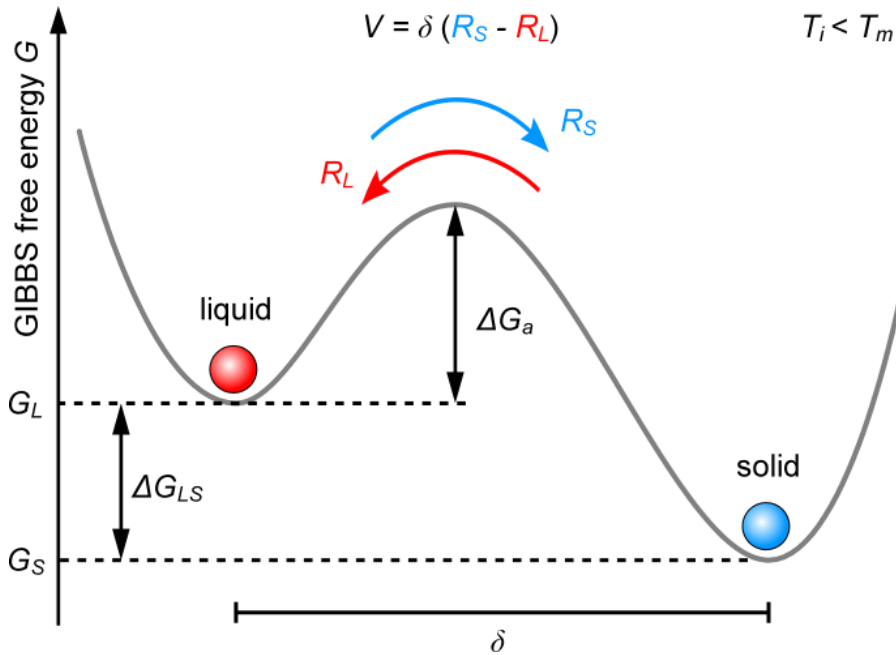


Figure 1-6: Schematic potential well at an interface temperature $T_i < T_E$ to illustrate the detachment rate R_L from solid to liquid and the attachment rate R_S from liquid to solid. The barrier height ΔG_a between liquid and solid is given by the activation energy for atomic diffusion whereas the GIBBS free energy difference ΔG_{LS} represents the asymmetry between liquid and solid.

A linearization of equation (1.4.2-1) for the typical case $\Delta G(T_i)/R_G T_i \ll 1$ leads to:

$$V = V_0 \frac{\Delta G_{LS}}{R_G T_i} = \mu_k \Delta T_K,$$

where $\Delta T_K = T_E - T_i$ is the *interfacial kinetic undercooling* for a planar interface moving at a constant velocity V . The mobility of such a moving phase boundary is defined as a constant $\mu_k > 0$ which is called *kinetic coefficient* given in $m \cdot s^{-1} \cdot K^{-1}$.

Using equation $\Delta G_{LS}(T) = \Delta H_f \Delta T / T_E$ the kinetic coefficient can be written as:

$$\mu_k = \frac{V_0 \Delta H_f}{R_G T_E T_i} \approx \frac{V_0 \Delta H_f}{R_G T_E^2}$$

Expressed in atomic quantities the equation changes to:

$$\mu_k = \frac{V_0 \Delta \hat{H}_f}{k_B T_E^2},$$

where $k_B = R_G / N_A = 1.3806504 \times 10^{-23} J/K$ is the BOLTZMANN constant and $\Delta \hat{H}_f$ is the latent heat of fusion per atom.

According to JACKSON [32] the mechanism of crystal growth can be classified as *diffusion limited* and *collision limited* growth. In the case of diffusion limited growth a complex crystal needs atomic rearrangement which is limited by the diffusion velocity V_D . The solidification front cannot move faster as the atoms diffuse. Whereas in the case of collision limited growth, like in a pure metal or solid solution, the growth velocity is governed by the number of collisions where an atoms from the liquid state collides with a solid atom and joins the crystal. In this situation the energy barrier ΔG_a is negligible small.

For pure Fe the kinetic coefficient μ_k can be approximated with the velocity of sound V_0 and is in the order of $10^4 m \cdot s^{-1}$.

Furthermore, the attachment kinetics depends on the crystallographic plane considered which means μ_k is anisotropic. In pure metals ΔT_K is small for slow growth velocities. However for very high growth velocities ($100 - 1000 m s^{-1}$) the atoms cannot move fast enough to avoid being captured by the moving solidification front. The structure of the liquid is frozen without rearrangement. This leads to an amorphous material which is called *metallic glass* in the case of metals. The first discovered metallic glass was an AuSi alloy in 1960 [33]. Amorphous metals have a widespread scientific and commercial interest due to their unique mechanical and magnetic properties [34, 35, 36]. By developing multicomponent alloy compositions with deep eutectics, large atomic size mismatch between constituents and sluggish crystallization kinetics,

the critical cooling rates to prevent crystallization could be reduced by orders of magnitude (from 10^6 in quenched ribbons to 0.7 K/s in Pd-Cu-Ni-P) [37].

In conclusion we arrive to the expression for the interface temperature T_i including the GIBBS-THOMSON effect (curvature undercooling ΔT_R) and the kinetic contribution:

$$T_i = T_E - \Delta T_R - \Delta T_K.$$

1.5.3 Solute Trapping

In general, the solid state has a lower solubility of solute in solvent than the liquid state. Consider an alloy solidifying under near equilibrium conditions which is schematically shown in the left image of Figure 1-7. The solute concentration in the liquid c_L^* and the solute concentration in the solid at the moving solid-liquid interface c_S^* defines the equilibrium *partition coefficient* $k_E = c_S^*/c_L^*$. The different solubility of solvent in liquid and solid phase leads to a pile up in front of the interface. This results in a concentration gradient into the undercooled liquid which is determined by the diffusion velocity V_D . The composition ahead of the solidification front (concentration field) differs from the initially composition of the liquid melt. Consequently the local conditions of solidification change which leads to a *constitutional undercooling*.

Consider a rapid propagation of the solid-liquid interface under non-equilibrium conditions. If the solidification front propagates faster as the diffusion velocity, an entrapment of solute occurs beyond its chemical equilibrium solubility. To put it more simply, the solute atoms cannot “escape” (diffuse) fast enough ahead of the solidification front. This effect is called *solute trapping* which results in a supersaturated solid solution. In the extreme case of complete solute trapping $c_S^* = c_L^*$ while $k = 1$. The right image of Figure 1-7 illustrates the phenomenon of solute trapping.

AZIZ and KAPLAN [38, 39] introduced an effective partition coefficient $k(V)$ depending on the solidification velocity V . They proposed a model for dilute and concentrated alloys in which $k(V)$ varies continuously between $k = k_E$ and $k = 1$.

The driving force for the solute redistribution at the interface is given by:

$$\kappa_e(c_L^*, c_S^*, T) = \exp\left(-\frac{\Delta(\mu'_B - \mu'_A)}{R_G T}\right),$$

where $\mu'(c, T) = \mu(c, T) - R_G T \ln(c)$. μ is the chemical potential while the symbol Δ refers to the differences of the thermodynamic potentials in the liquid and the solid state with respect to the components A and B.

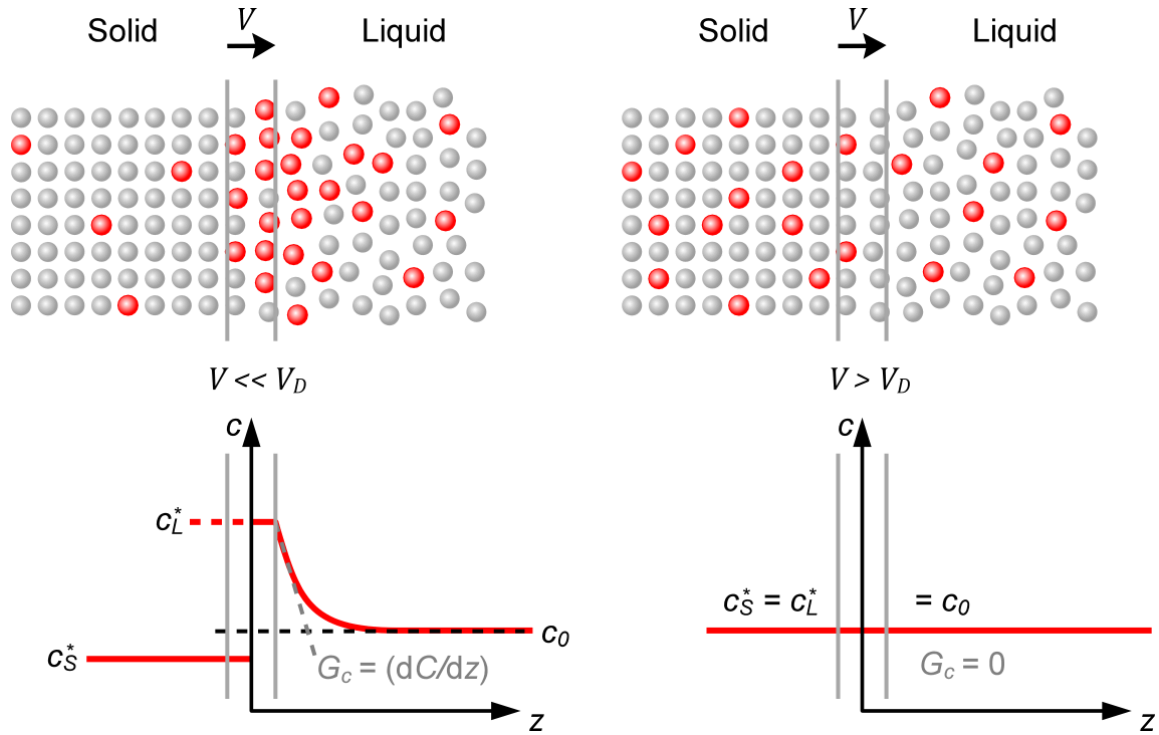


Figure 1-7: Solute Trapping: A solute pile up propagates ahead of the solidification front. As the growth velocity becomes higher as the speed of diffusion at the interface, the solute atoms are “trapped” in the solid. In the case of complete solute trapping the solute concentration in the solid are equal to the concentration in the liquid.

According to AZIZ and KAPLAN [39] the velocity dependent partition coefficient is given by:

$$k(V, T, c_L^*) = \frac{c_S^*}{c_L^*} = \frac{\kappa_e + V/V_{Di}}{1 - (1 - \kappa_e)c_L^* + V/V_{Di}},$$

where V_{Di} is the interface diffusion speed which is in the order of 10 m/s [40, 1].

For dilute alloys the equation simplifies and leads to following approximation:

$$k(V) = \frac{k_E + V/V_{DI}}{1 + V/V_{DI}}.$$

The effect of solute trapping occurs especially in systems with a small partition coefficient $k_E \ll 1$ like in Fe-B or Ni-B [41]. Solute trapping is expected to occur in the Fe-B system for small B concentrations at large undercoolings.

In the case of non-equilibrium solidification the equilibrium phase diagram is not valid and cannot be applied. The liquidus and solidus lines from an equilibrium phase diagram will approach each other for increasing growth velocity and increasing solute trapping at the interface. Due to the deviation from chemical equilibrium a kinetic liquidus line can be introduced constructing a kinetic phase diagram. The slope of such kinetic liquidus line m_V is given by:

$$m_V(V) = m_E \frac{1 - k(V) + k(V) \ln(k(V)/k_E)}{1 - k_E},$$

where m_E is the slope of the equilibrium liquidus line. The velocity dependence is factored in the non-equilibrium partition coefficient $k(V)$.

Experimental results can be well predicted for small and moderate growth velocities by the considerations above. However, the model is not able to predict complete solute trapping. This segregation free growth has been observed experimentally. The weak point of the model is the assumption of an infinite diffusion velocity in the bulk liquid $V_D = \infty$. Therefore GALENKO [42] proposed an additional kinetic parameter by introducing a finite diffusion velocity in the bulk liquid V_D . Taking into account the deviation from chemical equilibrium ahead of the solidification front and a finite diffusion velocity leads to:

$$k(V) = \begin{cases} \frac{k_E + c_0(1 - k_E) \left(1 - \frac{V^2}{V_D^2}\right) + \frac{V}{V_{DI}}}{1 - \frac{V^2}{V_D^2} + \frac{V}{V_{DI}}} & V < V_D \\ 1 & V \geq V_D \end{cases}$$

In the GALENKO model k reaches the value 1 at V_D while in the model by AZIZ $k = 1$ is only realized for an infinite growth velocity $V = \infty$. This behaviour is illustrated in Figure 1-8 which shows a schematically plot of a hypothetical velocity dependent partition coefficient. The model by GALENKO was recently confirmed by molecular dynamics simulations (MD) [43].

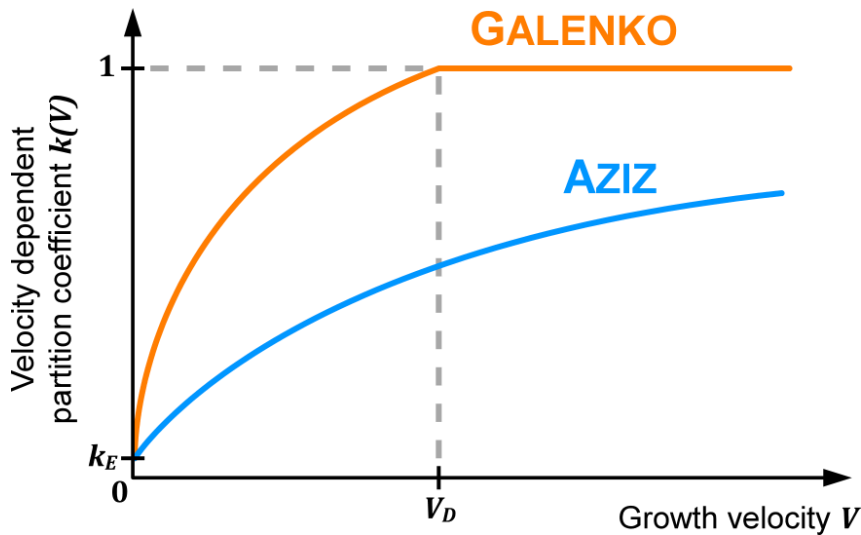


Figure 1-8: Schematic plot of the velocity dependent partition coefficient $k(V)$ as a function of the growth velocity V according to models by AZIZ and GALENKO.

2 DENDRITIC GROWTH MODEL

The previous chapter introduced the physical background to describe nucleation and solidification in undercooled liquids. The present chapter provides the concept of dendritic growth and how to model dendrite growth velocities as a function of undercooling according to a *sharp interface model* taking into account *fluid flow* effects in heat and mass transport in the melt.

After a stable nucleus is formed in an undercooled melt the solidification is assumed to propagate as a steady-state process. Thermal and solute gradients govern rapid solidification and cause deviations from equilibrium since the overall system is not at the lowest GIBBS free energy. As already discussed the main effects from local equilibrium to non-equilibrium solidification are:

- surface energy of a curved interface,
- attachment kinetics of the atoms, and
- trapping of solute elements.

In the case of an undercooled melt, the sample solidifies rapidly under non-equilibrium conditions. A planar growth front becomes unstable due to a negative temperature and a concentration gradient which leads to a different growth morphology. For metals the major growth mode is dendritic. Figure 2-1 (left image) shows a solidified dendritic structure at the surface of a Fe-5 at.% B sample and a schematic growing dendrite (right image). Obviously a dendrite has a multi-branch “tree-like” crystal structure. In fact, the term “dendrite” derives from the Greek word *Déndron* ($\delta\acute{\epsilon}\nu\delta\rho\nu$), which means “tree”.

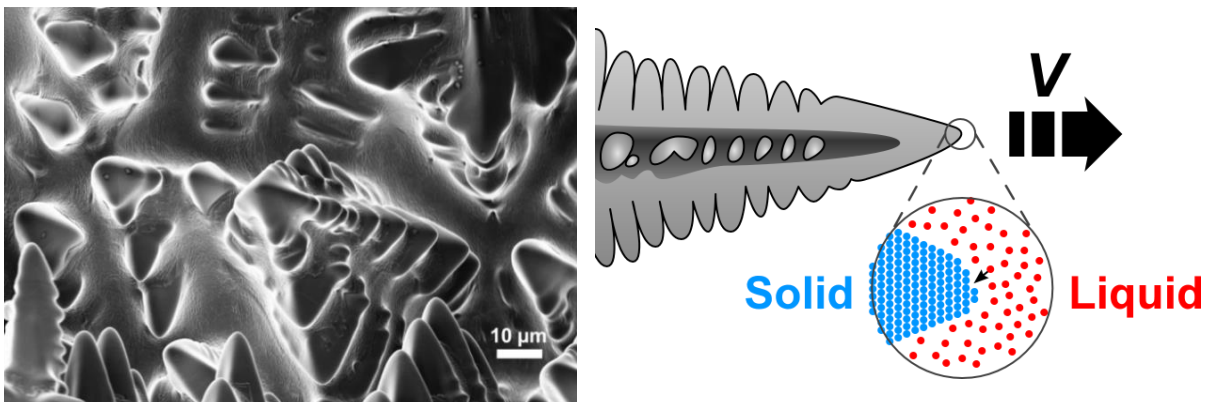


Figure 2-1: Left picture: SEM image of a Fe-5 at.% B sample surface. Right picture: Schematic illustration of a growing dendrite into the liquid.

2.1 Sharp Interface Model for Dendritic Solidification

The sharp interface model is a one dimensional simplification of an idealized growing dendrite. Furthermore the dendrite tip is assumed to be a rotational paraboloid with a sharp phase boundary of solid and liquid at the interface.

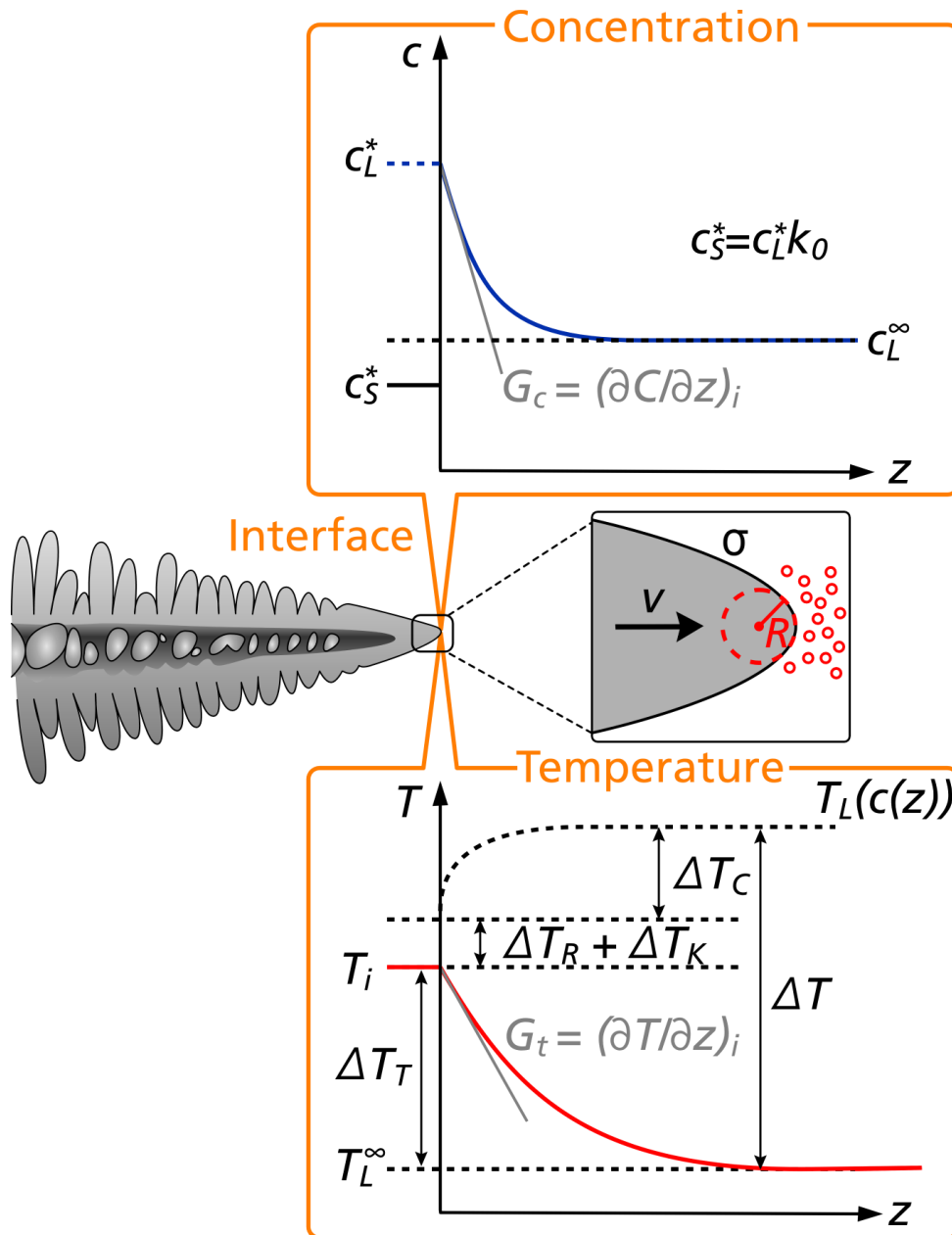


Figure 2-2: Schematic illustration of the sharp interface model defining the temperature and solute concentration field ahead of a parabolic dendrite tip with the interface temperature T_i and curvature radius R which grows at a constant velocity V into the undercooled melt. The total undercooling $\Delta T = T_L - T_L^\infty$ splits into various contributions: the thermal undercooling ΔT_T , the constitutional undercooling ΔT_C , the curvature undercooling ΔT_R and the kinetic undercooling ΔT_K .

In this study a sharp interface model developed by GALENKO and DANILOV [44, 45] is applied that is an extension of the LKT-model (by LIPTON, KURZ, and TRIVEDI) [46] in the respect of measured

dendrite growth velocities V as a function of undercooling ΔT . The total undercooling ΔT as measured in the experiment is illustrated in Figure 2-2 which splits into various contributions:

$$\Delta T = \Delta T_T + \Delta T_C + \Delta T_N + \Delta T_R + \Delta T_K. \quad (2.1-1)$$

The terms of undercooling are listed in Table 2-1 and described in the following. Figure 2-2 illustrates the concept of the model and shows the contributions of each undercooling term.

In the case of a pure metal, the total undercooling simplifies to $\Delta T = \Delta T_T + \Delta T_R + \Delta T_K$.

Table 2-1: Terms of undercooling

Term		Description/Origin
ΔT	Total undercooling	Sum of all undercooling contributions
ΔT_T	Thermal undercooling	Heat transport
ΔT_C	Constitutional undercooling	Mass transport
ΔT_N	Non-equilibrium liquidus undercooling	Slope of the kinetic liquidus line
ΔT_R	Curvature undercooling	GIBBS-THOMSON effect
ΔT_K	Kinetic undercooling	Kinetic and attachment effects

The *thermal undercooling* ΔT_T at the dendrite tip is governed by the heat transport into the liquid, which is expressed by:

$$\Delta T_T = T_i - T_L^\infty = \frac{\Delta H_f}{\underbrace{c_{p,L}}_{\Delta T_{hyp}}} Iv(P_T),$$

where T_i is the temperature at the interface (dendrite tip) of the growing dendrite and T_L^∞ is the temperature of the undercooled melt far from the interface. The latent heat of fusion ΔH_f divided by the specific heat of the liquid $c_{p,L}$ defines the *hypercooling limit* $\Delta T_{hyp} = \Delta H_f / c_{p,L}$ which is the maximum increase in the interface temperature due to the release of latent heat. The thermal PÉCLET number $P_T(V, R) = V \cdot R / (2D_T)$ is a function of the dendrite tip growth velocity V and the tip radius curvature R while D_T is the thermal diffusivity in the liquid which is in the order of $10^{-5} \text{ m}^2/\text{s}$. The heat diffusion into the undercooled melt is described by the related IVANTSOV function $Iv(P_T) = P_T \cdot \exp(P_T) E_1$, where $E_1 := \int_1^\infty t^{-1} \exp(-t \cdot x) dt$ is the first exponential integral function.

The *solutal/constitutional undercooling* ΔT_C is characterized by the mass transport into the liquid:

$$\Delta T_C = \frac{m_V C_0 (k_V - 1) Iv(P_C)}{1 - (1 - k_V) Iv(P_C)},$$

with the velocity dependent partition coefficient k_V , the IVANTSOV function for mass diffusion $Iv(P_C) = P_C \cdot \exp(P_C)E_1$, and the PÉCLET number of mass diffusion $P_C(V, R) = V \cdot R/(2D_C)$. The diffusion coefficient D_C is not well known. BRILLO et al. found a relation between viscosity and self-diffusion $D\eta = \text{const}$ in the case of ZrNi [47]. This stands in contrast to the EINSTEIN-STOKES-equation:

$$D_C = \frac{k_B T}{6\pi\eta R_a},$$

which gives an approximation for the diffusion coefficient valid for spherical particles with radius R_a in a liquid with the dynamic viscosity η for low REYNOLDS number. However, the EINSTEIN-STOKES-equation is used within this work to give an estimation for the diffusion coefficient. In the case of B in Fe the diffusion coefficient D_C is in the order $10^{-9} \text{ m}^2/\text{s}$ while the atomic diffusion speed in the bulk liquid V_D for B in Fe is about some m/s . The liquidus slope m_V is given by:

$$m_V(V) = \frac{m_E}{1-k_E} \left[1 - k_V + \ln\left(\frac{k_V}{k_E}\right) + (1 + k_V)^2 \frac{V}{V_D} \right], \quad V < V_D$$

$$m_V(V) = \frac{m_E \ln(k_E)}{k_E - 1}, \quad V \geq V_D$$

where k_E is the equilibrium partition coefficient and m_E is the slope of the equilibrium liquidus line in the equilibrium phase diagram.

In the case of rapid solidification, the solute partition coefficient k becomes a function of the growth velocity (section 1.5.3) which is expressed by the non-equilibrium partition coefficient k_V [42]:

$$k_V(V) = \begin{cases} \frac{k_E + c_0(1 - k_E) \left(1 - \frac{V^2}{V_D^2}\right) + \frac{V}{V_{DI}}}{1 - \frac{V^2}{V_D^2} + \frac{V}{V_{DI}}} & V < V_D \\ 1 & V \geq V_D \end{cases}$$

where c_0 is the nominal composition. The interface diffusion velocity V_{DI} can be obtained by dividing the diffusion coefficient D_C in the solid-liquid interface by the interatomic spacing a_0 ($V_{DI} = D_C/a_0$). The diffusion coefficient at the interface is smaller compared to the bulk diffusion coefficient [48].

The concentration at the dendrite tip can be calculated by:

$$c_L^* = \begin{cases} \frac{c_0}{1 - (1 - k_V)Iv(P_C)}, & V < V_D, \\ c_0, & V \geq V_D. \end{cases}$$

The *non-equilibrium liquidus undercooling* ΔT_N takes into account the shift of the equilibrium liquidus slope m_E to its non-equilibrium liquidus value m_V in the kinetic phase diagram:

$$\Delta T_N = (m_E - m_V)C_0,$$

which is the case for large dendrite growth velocities.

The *curvature undercooling* ΔT_R due to the GIBBS-THOMSON effect (section 1.5.1) is defined by:

$$\Delta T_R = \frac{2\Gamma}{R},$$

with the GIBBS-THOMSON coefficient $\Gamma = \gamma_0 V_{mol} / \Delta S_f$ and the radius of curvature R .

As described in section 1.5.2 the *kinetic undercooling* ΔT_K is expressed by:

$$\Delta T_K = \frac{V}{\mu_K},$$

which takes into account kinetic effects at the solid-liquid interface and the attachment of atoms from liquid to solid. The kinetic growth coefficient

$$\mu_K = \frac{f v_0 \Delta H_f}{R_G T_L^2}$$

represents the mobility of the phase boundary as described in chapter 1.5.2.

Now all terms of undercooling ΔT have been defined and the interface temperature T_i at the dendrite tip is determined. However the undercooling $\Delta T(V, R)$ is a function of the velocity V and the dendrite tip radius R which is unknown. Possible dendrite tip radii are thin fast growing dendrites and thick slow growing dendrites. For a given undercooling ΔT Figure 2-3 shows possible pairs of (V, R) . The IVANTSOV solution for the moving-boundary-problem $V \cdot R = const$ (isothermal solution $\Delta T = \Delta T_T$) gives an infinite number of possible values (dashed line in Figure 2-3). This solution assumes an isothermal solid-liquid interface ($T_i = T_E$) and does not take into account the GIBBS-THOMSON effect. Experiments by GLICKSMAN [49] on transparent systems demonstrated that dendrites always grow with a particular growth velocity V and a specific tip radius R . Moreover the growth velocity increases with undercooling whereas the tip radius decreases. Figure 2-4 illustrates this behaviour for a pure system and an alloy. TEMKIN [50] includes the curvature of the dendrite tip for an isotropic case $\Delta T = \Delta T_T + \Delta T_R$ (non-isothermal solution) which is shown as the green curve in Figure 2-3. According to this analysis a minimum tip radius R_{min} exists at $V = 0$ which can be identified with the critical cluster radius r^* of a nucleus. The maximum-velocity principle proposes that the dendrite grows with its maximum velocity V_{max} . However this assumption is not in agreement with the experiments by

GLICKSMAN which show a much larger dendrite tip radius. LANGER and MÜLLER-KRUMBHAAR [51, 52] suggested a selection criterion for a stable dendrite tip radius and introduced the *marginal stability criterion* $\sigma^* = 1/4\pi^2$. According to them the operating dendrite tip radius is approximately equal to a minimum wavelength for planar instabilities. Even if this selection criterion leads to a good agreement between theory and experiment, it is not based on a physical explanation. The microscopic *solvability theory* [53, 54, 55] provides a solution of the form $V \cdot R^2 = \text{const}$ and predicts a selection constant σ^* which depends on the capillary anisotropy of strength ε [56]. As a consequence of the solvability theory dendrite growth requires anisotropy of the interfacial dynamics and therefore gives an explanation why dendrites grow along preferred crystallographic directions.

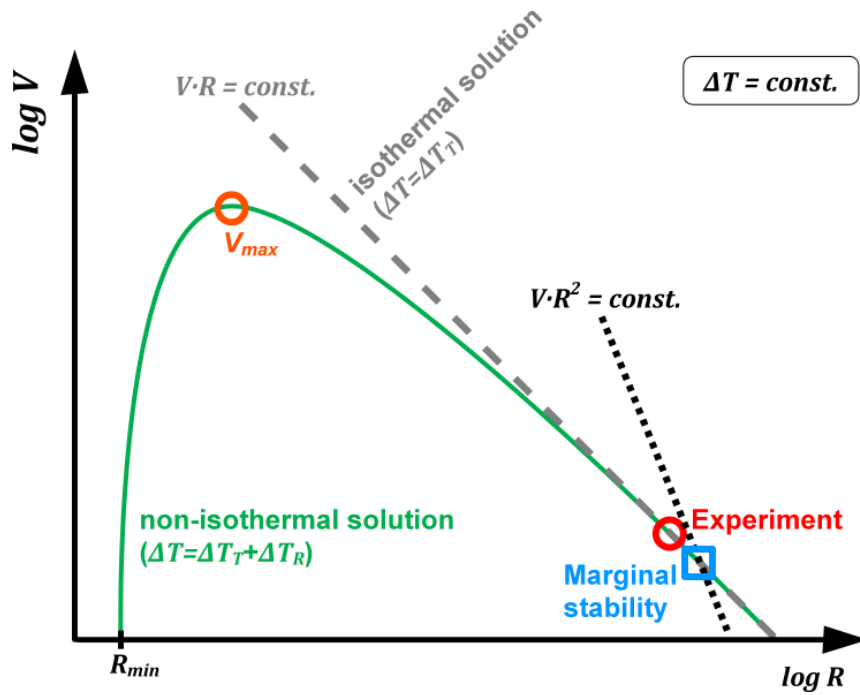


Figure 2-3: Possible value pairs (R, V) for a given undercooling according to IVANTSOV ($V \cdot R = \text{const}$) with respect to a pure system and steady state growth, maximum velocity V_{max} and solvability theory ($V \cdot R^2 = \text{const}$). Experimental result by GLICKSMAN in comparison with marginal stability criterion and solvability theory.

The *stability analysis* according to the *solvability theory* provides an equation for a unique determination of the growth velocity V with a corresponding dendrite tip radius R as a function of undercooling ΔT :

$$\frac{2d_0 a_L}{VR^2} = \begin{cases} \sigma_0 \varepsilon_C^{7/4} \left[\frac{1}{2} \xi_T(P_T) + \frac{2m(V)c_0}{DQ} \xi_C(P_C) \right], & V < V_D, \\ \sigma_0 \varepsilon_C^{7/4} \left[\frac{1}{2} \xi_T(P_T) \right], & V \geq V_D. \end{cases} \quad (2.1-2)$$

The dimensionless stability constant $\sigma^* = \sigma_0 \varepsilon_C^{7/4}$ depends on the shape of the solid-liquid interface, where ε_C is the interface anisotropy parameter and $\sigma_0 > 0$ is a constant.

$$\sigma^* = \begin{cases} \frac{2d_0 a_L}{VR^2} = \frac{1}{4\pi^2} \approx 0.0253 & \text{(planar phase boundary)} \\ 0.0192 & \text{(spherical phase boundary)} \\ 0.025 & \text{(parabolic phase boundary)} \end{cases}$$

$\xi_T(P_T)$ and $\xi_C(P_C)$ are the stability functions which depend on the thermal and the chemical PÉCLET numbers. They are given by:

$$\xi_T(P_T) = \frac{1}{(1 + a_1 \varepsilon^{1/2} P_T)^2},$$

$$\xi_C(P_C) = \frac{1}{(1 + a_2 \varepsilon^{1/2} P_C)^2},$$

where $\varepsilon = 15\varepsilon_C$ is the stiffness for a crystal with cubic symmetry and the anisotropy ε_C of the interfacial energy. In particular, $\xi_{T,C}(P_{T,C}) \rightarrow 1$ for small growth velocities ($V \rightarrow 0$) and $\xi_{T,C}(P_{T,C}) \rightarrow 0$ for high growth velocities ($V \rightarrow \infty$). The parameters a_1 and a_2 are obtained by fitting to experimental data or by an asymptotical analysis [57].

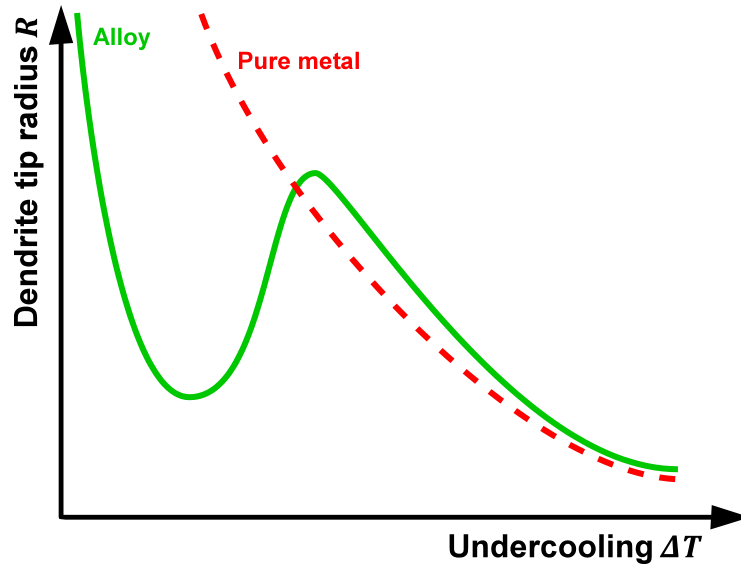


Figure 2-4: Schematic dendrite tip radius R as a function of undercooling ΔT in the case of an alloy and pure metal.

Finally the growth velocity V can be calculated as a function of undercooling ΔT by simultaneously solving the equations for the total undercooling $\Delta T(V, R)$ (2.1-1) and for the dendrite tip radius $R(V, R)$ (2.1-2). The numerical calculations for this thesis are done with the software WOLFRAM MATHEMATICA 8.

In conclusion, a pure metal and an alloy differ in their dendritic growth behaviour. In the case of a pure metal the dominating undercooling contribution is the thermal undercooling ΔT_T . The so called “thermal” dendrites are mainly governed by the heat flow which is determined by the

thermal diffusivity $D_T \approx 10^{-5} \text{ m}^2/\text{s}$. On the contrary for an alloy the constitutional undercooling ΔT_C dominates for low undercoolings. The so called “*solutal*” dendrites are governed by mass diffusion which is determined by the diffusion coefficient $D_C \approx 10^{-9} \text{ m}^2/\text{s}$. “Thermal” dendrites are much faster as “solutal” dendrites because D_T and D_C differ by four orders of magnitude. At large undercoolings a transition occurs from solutal-controlled to thermally-controlled dendrite growth. At high growth velocities (large undercoolings) an alloy behaves like a pure metal.

2.2 Influence of Convection on Dendrite Growth

So far we treated dendritic solidification as a steady state one-dimensional sharp interface process which is an interplay between heat/mass transport, attachment kinetics and surface energy. However experimental reality cannot provide ideal conditions like for instance a resting liquid in its mechanical equilibrium without fluid flow. In experiments, natural and forced convection occur. Namely fluid flow is generated by BUOYANCY forces due to thermal and/or concentrational gradients (natural convection), by surface tension gradients (MARANGONI convection), and by external forces like electromagnetic stirring (forced convection). In particular, the fluid flow acts on the concentration and temperature gradient field ahead of the solidification front which will be discussed in the following and implemented into the sharp interface model.

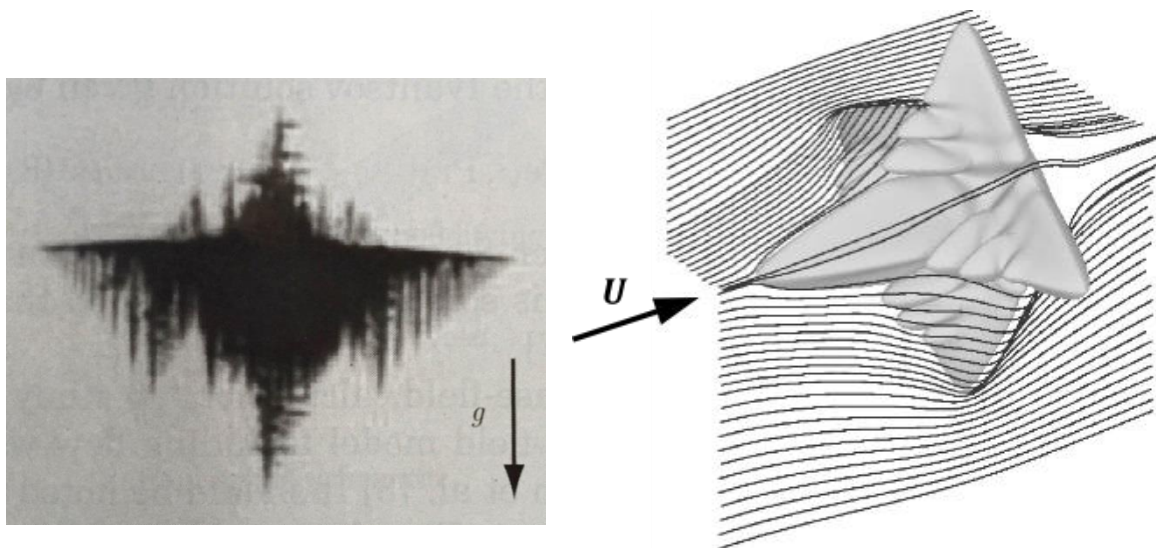


Figure 2-5: Left image: Effect of fluid flow on the growth of a settling NH_4Cl crystal showing an enhanced growth velocity in the opposing fluid flow direction [10]. Right image: Computed streamtraces for fluid flow over a phase-field modelled growing isolated dendrite [58].

The left image of Figure 2-5 shows a settling NH_4Cl growing dendritic crystal which corresponds to an upward fluid flow U [10]. A significant enhanced dendrite growth velocity can be observed in the opposite direction of the fluid flow relative to the crystal. The right image shows a phase-field simulation of a growing dendrite with indicated fluid flow streamtraces [58]. Obviously the dendrite grows faster against the direction of fluid flow U .

Consequently the mechanism of convection inside the undercooled melt has to be taken into account to model the experimental results. We will see later, especially if the fluid flow velocity is in the same order of magnitude or greater as the solidification velocity itself. A modification to the LKT-model with respect to the effect of forced convection caused by electromagnetic stirring has been suggested by GALENKO et al. [59, 60].

As an estimation for electromagnetic levitation experiments (experimental method described in chapter 4.1), the fluid flow velocity U_0 is assumed to be a result of the balance between the electromagnetic field, gravitation, and the viscous dissipation:

$$U_0 = \left[\frac{2}{\rho} \left(\rho g R_0 + \frac{B_0^2 \left(1 - \exp\left(2 R_0 / \delta\right)\right)}{8\pi} + \frac{\rho \eta^2}{2\delta^2} \right) \right]^{1/2},$$

where g is the gravity acceleration, ρ is the mass density, η is the dynamic viscosity of the liquid, δ is the skin depth, R_0 is the radius of the sample, and B_0 is the time averaged value of the magnetic field inside the levitation coil.

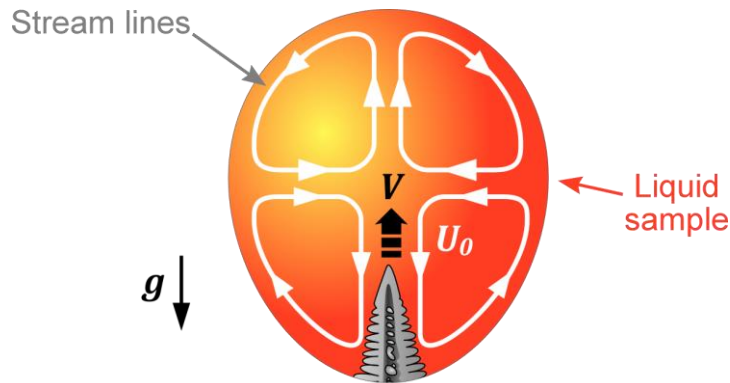


Figure 2-6: Upwards growing dendrite in an electromagnetic levitated liquid sample with indicated streamlines. In this idealized case the fluid flow velocity U_0 occurs in the opposite direction as the dendrite growth velocity V .

In the case of forced convection inside the melt, the stability parameter σ^* becomes dependent on the fluid flow velocity U_0 which can be expressed by:

$$\sigma^* = \frac{\sigma_0 \varepsilon_c^{7/4}}{1 + \chi(Re) \frac{U_0 \Gamma}{a \Delta T_{hyp}}},$$

where σ_0 is the stability constant, Re is the REYNOLDS number and $\chi(Re)$ is a function which is defined by BOUISSOU and PELCÉ in Ref. [61]. The stability parameter σ^* was chosen to fulfil $\sigma_0 \varepsilon_c^{7/4} / \sigma^* = 1.675$ as a result of phase-field modelling [58] in the idealized case of an upstream fluid flow for a free growing dendrite which is illustrated in Figure 2-6. The thermal

undercooling ΔT_T and the constitutional undercooling ΔT_C have to be modified due to convection. This is expressed by additional thermal and mass diffusion PÉCLET numbers which dependent on the fluid flow velocity U_0 which are defined by:

$$P_T^f(U_0, R) = \frac{U_0 \cdot R}{2a_L},$$

$$P_C^f(U_0, R) = \frac{U_0 \cdot R}{2D}.$$

Consequently the thermal undercooling $\Delta T = T_i - T_L^\infty$ is given by:

$$\Delta T_T = T_i - T_L^\infty = \Delta T_{hyp} \cdot P_T \cdot \exp(P_T + P_T^f) \int_1^\infty q^{-1} \exp(-q \cdot P_T + (\ln q - q)P_T^f) dq,$$

and the constitutional undercooling ΔT_C changes to:

$$\Delta T_C = \frac{m_V C_0 (k_V - 1) Iv^f(P_C, P_C^f)}{1 - (1 - k_V) Iv^f(P_C, P_C^f)},$$

while $Iv^f(P_C, P_C^f) = P_C \cdot \exp(P_C + P_C^f) E_{1-P_C^f}(P_C + P_C^f)$ is a modified IVANTSOV function.

3 EUTECTIC GROWTH MODEL

The dendritic growth is a single-phase growth mechanism. Eutectic growth is a cooperative growth of two solid phases within one liquid phase. This chapter gives a description of the eutectic growth theory and introduces a modified JACKSON-HUNT model [62] for eutectic solidification to analyse the experimental results. For further details and explanations the author refers to Chapter 7 in the book METASTABLE SOLIDS FROM UNDERCOOLED MELTS by D.M. HERLACH, P. GALENKO and D. HOLLAND-MORITZ [11].

The Fe-B system is a metallic glass former. Metallic glasses are characterized by the fact that no crystallographic long range order is present in the solidified material. For instance, if the Fe-17 at.% B alloy melt is undercooled to the glass transition temperature T_g the undercooled melt freezes into a metastable amorphous phase. However, this experimental conditions cannot be realized by the experimental methods used within this thesis. Therefore much higher cooling rates are necessary ($\sim 10^6 K s^{-1}$). In the case of 1g-EML experiments which are performed in this work, the Fe-17 at.% B alloy solidifies eutectic. The eutectic solidification is a cooperative growth of two phases simultaneously which is shown schematically in Figure 3-1. In particular, γ -Fe solid solution and stoichiometric compound Fe_2B solidify.

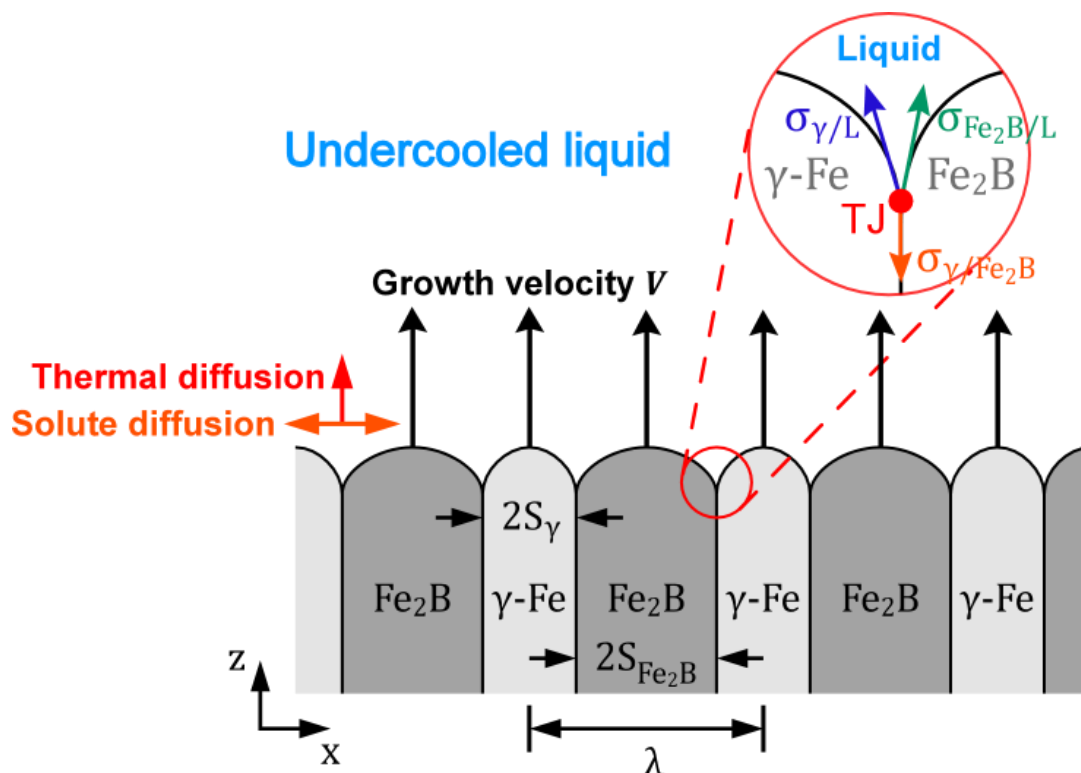


Figure 3-1: Schematic illustration of eutectic solidification in Fe-B alloy system. λ is the interlamellar spacing. S_{γ} and S_{Fe_2B} are the half widths of γ -Fe and Fe₂B. $\sigma_{\gamma/L}$, $\sigma_{Fe_2B/L}$ and σ_{γ/Fe_2B} are the interface energies at the triple junction point (TJ). V is the steady state growth velocity of both phases solidifying cooperatively into the liquid.

In cooperation with Professor HAIFENG WANG and his student KUANG WANGWANG a modified JACKSON-HUNT model [62] for eutectic solidification is used within this thesis to model the 1g-EML experimental results for the eutectic composition Fe-17 at.% B [63].

Eutectic alloys have been studied intensively by experiments and modelling due to their economic importance (e.g. casting [64], pattern formation and selection [65]). The pioneering work for modelling eutectic growth was done by JACKSON and HUNT (JH) in 1966 [62]. They assumed a linear phase-diagram (LPD) for solidification under local equilibrium conditions. The JH model is able to predict the experimental results in directional solidification (e.g. Al-Cu [66] and In-In₂Bi [67] eutectic alloys). In order to show some physical insights into rapid solidification, two simple types of LPD were adopted by TRIVEDI-MAGNIN-KURZ (TMK) [68]. One model assumes cigar-shaped growth with parallel liquidus and solidus lines below the equilibrium eutectic temperature while the other model uses constant and equal partition coefficients. Subsequently, non-equilibrium kinetics are implemented with LPD to apply for rapid solidification in a dilute alloy [69].

Even though TMK-kind models [68, 69] are widely used in rapid solidification, the LPDs are rarely found in practical alloy systems. In fact, the assumption of dilute alloys with LPD is only applicable to small undercooling [70, 71]. In the case of an undercooled eutectic alloy, the negative temperature gradient ahead of the migrating interface results in an interface instability which leads to the formation of an eutectic dendrite morphology [72, 73]. Assuming a purely thermal driven dendrite, the eutectic growth model (e.g. TMK [68]) and dendrite growth model (e.g. Lipton-Kurz-Trivedi (LKT) [46]) can be combined to describe the solute diffusion parallel to the interface, and the thermal diffusion perpendicular to it [74, 75]. However these eutectic dendrite growth models for dilute alloys with LPD [74, 75] cannot predict the experimental results, especially at high undercooling according to calculation results in Refs. [46, 73, 74]. Therefore a modified model with non-linear phase diagram (NLPD) is introduced in the following.

3.1 Current Model for Concentrated Alloys with Non-Linear Phase Diagram (NLPD)

Figure 3-1 illustrates the concept of eutectic solidification and shows the used important variables. For a migrating planar interface under steady state conditions, the non-equilibrium diffusion equation is given by [76]:

$$\frac{\partial^2 C_L}{\partial X^2} + \left(1 - \frac{V^2}{V_{DL}^2}\right) \frac{\partial^2 C_L}{\partial Z^2} + \frac{V}{D_L} \frac{\partial C_L}{\partial Z} = 0 \quad (3.1-1)$$

The solution of Eq. (3.1-1) in the case of lamellar eutectic growth is [76]:

$$C_L(X, Z) = \begin{cases} C_0 + \sum_{n=0}^{\infty} B_n \cos(b_n X) \exp\left[-\frac{VZ\omega_n}{D_L(1-V^2/V_{DL}^2)}\right], & V < V_{DL} \\ C_0, & V \geq V_{DL} \end{cases} \quad (3.1-2)$$

Here C_L is the liquid concentration, C_0 is the liquid concentration far from the interface, V is the growth velocity, V_{DL} is the solute diffusion velocity in the liquid, D_L is the solute diffusion coefficient, $b_n = 2n\pi/\lambda$ ($n = 0, 1, 2, \dots$) and $\omega_n = \left[1 + \sqrt{1 + \psi(2n\pi/P_e)^2}\right]/2$ with λ the lamellar spacing and $P_e = V\lambda/2D_L$ the PÉCLET number.

In order to obtain the Fourier coefficients B_n ($n = 0, 1, 2, \dots$), the average mass conservation law at the interface is introduced by [77]:

$$-\frac{D_L \psi}{V} \left(\frac{\partial C_L}{\partial Z}\right)_{Z=0} = \begin{cases} \bar{C}_{L\gamma}^* - \bar{C}_\gamma^* & , 0 \leq X < S_\gamma \\ \bar{C}_{LFe_2B}^* - C_{Fe_2B} & , S_\gamma < X < S_\gamma + S_{Fe_2B} \end{cases}, \quad (3.1-3)$$

where S_γ (S_{Fe_2B}) is the half width of the γ -Fe (Fe_2B) lamellar spacing, \bar{C}_γ^* is the average solute concentration of γ at the γ/L interface, C_{Fe_2B} the concentration of a stoichiometric compound Fe_2B is constant and equal to $1/3$ and, $\bar{C}_{L\gamma}^*$ and $\bar{C}_{LFe_2B}^*$ are the average liquid concentration at the γ/L and the Fe_2B/L interface which can be obtained from Equation (3.1-2) as:

$$\bar{C}_{L\gamma}^* = \frac{1}{f_\gamma \lambda} \int_0^{f_\gamma \lambda} C_L(X, 0) dX = C_0 + B_0 + \sum_{n=1}^{\infty} \frac{B_n}{n\pi f_\gamma} \sin(n\pi f_\gamma) \quad (3.1-4)$$

$$\bar{C}_{LFe_2B}^* = \frac{1}{f_{Fe_2B} \lambda} \int_{f_\gamma \lambda}^{\lambda} C_L(X, 0) dX = C_0 + B_0 - \sum_{n=1}^{\infty} \frac{B_n}{n\pi f_{Fe_2B}} \sin(n\pi f_\gamma) \quad (3.1-5)$$

Substituting equations (3.1-2), (3.1-4) and (3.1-5) into equation (3.1-3) and noting that the concentration at the triple-junction point (e.g. $X = S_\gamma$, $Z = 0$) is equal to the kinetic eutectic concentration \hat{C}_L of a planar interface [77, 78], the Fourier coefficients B_n are obtained as:

$$B_0 = C_L^\wedge - C_0 - \sum_{n=1}^{\infty} B_n \cos(n\pi f_\gamma) \quad (3.1-6)$$

$$B_n = \frac{2\sin(n\pi f_\alpha)}{\omega_n n\pi} (C_{\text{Fe}_2\text{B}} - \bar{C}_\gamma^*) / \left[1 - \sum_{m=1}^{\infty} \frac{2\sin^2(m\pi f_\gamma)}{\omega_m m^2 \pi^2 f_\gamma f_{\text{Fe}_2\text{B}}} \right] \quad (n \geq 1), \quad (3.1-7)$$

where f_γ and $f_{\text{Fe}_2\text{B}}$ are the volume fraction of γ -Fe and Fe_2B , respectively. The introduction of an average mass conservation law with the interface equation (3.1-3) instead of the mass conservation law at the interface for dilute alloys with LPD, makes the current solution of diffusion equation applicable to concentrated alloys with NLPD [77, 78].

The kinetic eutectic composition C_L^\wedge is determined by the kinetic conditions at the γ/L (equations (3.1-8) and (3.1-9)) and $\text{Fe}_2\text{B}/L$ (equation (3.1-10)) interfaces:

$$\frac{V}{V_{DL}^I} = \frac{R_g T_I}{C_L^\wedge - C_\gamma^\wedge} \left(\frac{\partial \tilde{\mu}_L^\wedge}{\partial C_L^\wedge} \right)^{-1} \left(1 - \frac{V^2}{V_{DL}^I{}^2} \right) \left[1 - \exp \left(- \frac{\Delta \mu_{\gamma/L}^{\text{Fe}^\wedge} - \Delta \mu_{\gamma/L}^{\text{B}^\wedge}}{R_g T_I} \right) \right], \quad (3.1-8)$$

$$\frac{V}{V_0} = 1 - \exp \left[\frac{C_L^\wedge \Delta \mu_{\gamma/L}^{\text{B}^\wedge} + (1 - C_L^\wedge) \Delta \mu_{\gamma/L}^{\text{Fe}^\wedge}}{R_g T_I} \right], \quad (3.1-9)$$

$$V = \left[\frac{1}{V_0} + \frac{(C_L^\wedge - C_{\text{Fe}_2\text{B}})^2}{V_{DL}^I (1 - V^2/V_{DL}^I{}^2)} \left(\frac{\partial \tilde{\mu}_L^\wedge}{\partial C_L^\wedge} \right) \right]^{-1} \left\{ 1 - \exp \left[- \frac{C_{\text{Fe}_2\text{B}} \Delta \mu_{\text{Fe}_2\text{B}/L}^{\text{B}^\wedge} + (1 - C_{\text{Fe}_2\text{B}}) \Delta \mu_{\text{Fe}_2\text{B}/L}^{\text{Fe}^\wedge} - g_{\text{Fe}_2\text{B}}}{R_g T_I} \right] \right\}, \quad (3.1-10)$$

where V_{DL}^I is the interfacial solute diffusion velocity, V_0 is the upper limit velocity of V , $\Delta \mu_{i/L}^{j^\wedge} = \mu_i^{j^\wedge} - \mu_L^{j^\wedge}$ ($i = \gamma, \text{Fe}_2\text{B}$; $j = \text{Fe}, \text{B}$) is the chemical potential difference between solid and liquid, $\tilde{\mu}_L^\wedge = \mu_L^{\text{B}^\wedge} - \mu_L^{\text{Fe}^\wedge}$ is the solute diffusion potential, R_g is the gas constant, T_I is the interface temperature and $g_{\text{Fe}_2\text{B}}$ the Gibbs energy of Fe_2B which is temperature-dependent but not concentration-dependent. For the solid-solution phase γ -Fe, there are two independent dissipative processes which are a trans-interface diffusion equation (3.1-8) and an interface migration equation (3.1-9). Whereas for the stoichiometric compound Fe_2B two dissipative processes dependent on each other and the kinetic interface condition is given by only one equation (3.1-10) [78, 79].

In the case of LPD, the average interface undercooling is adopted generally to obtain uniquely the relation between λ and ΔT ($= T_E^e - T_I$) for a given growth velocity V from the minimum undercooling principle $\partial \Delta T_I / \partial \lambda = 0$ [62]. However this method is not applicable here because the interface undercooling contributions (e.g. constitutional undercooling, curvature undercooling etc.) cannot be obtained analytically in the case of NLPD [78, 79, 80]. Therefore, the average

kinetic interface conditions for migration of the γ/L and $\text{Fe}_2\text{B}/L$ interfaces are averaged by the volume fractions of γ and Fe_2B :

$$V = f_\gamma V_0 \left\{ 1 - \exp \left[\frac{\bar{C}_{L\gamma}^* \Delta \bar{\mu}_{\gamma/L}^{B^*} + (1 - \bar{C}_{L\gamma}^*) \Delta \bar{\mu}_{\gamma/L}^{\text{Fe}^*} - V_m \bar{K}_{\gamma/L} \sigma_{\alpha/L}}{R_g T_I} \right] \right\} + f_\beta \left[\frac{1}{V_0} + \frac{(\bar{C}_{L\text{Fe}_2\text{B}}^* - C_{\text{Fe}_2\text{B}})^2}{V_{DL} (1 - V^2/V_{DL}^2)} \left(\frac{\partial \bar{\mu}_L^*}{\partial \bar{C}_{L\text{Fe}_2\text{B}}^*} \right) \right]^{-1} \left\{ 1 - \exp \left[- \frac{C_{\text{Fe}_2\text{B}} \Delta \bar{\mu}_{\text{Fe}_2\text{B}/L}^{B^*} + (1 - C_{\text{Fe}_2\text{B}}) \Delta \bar{\mu}_{\text{Fe}_2\text{B}/L}^{\text{Fe}^*} - g_{\text{Fe}_2\text{B}} + V_m \bar{K}_{\text{Fe}_2\text{B}/L} \sigma_{\text{Fe}_2\text{B}/L}}{R_g T_I} \right] \right\} \quad (3.1-11)$$

where $\bar{K}_{i/L} = -2 \sin \theta_i / \lambda f_i$ with θ_i ($i = \gamma$ and Fe_2B) the contact angle is the average interface curvature [80], $\sigma_{\gamma/L}$ and $\sigma_{\text{Fe}_2\text{B}/L}$ are the interface energies. V_m is the molar volume which is assumed to be the same for γ -Fe and Fe_2B . Similarly, the averaged kinetic interface condition for trans-interface diffusion at the γ/L interface is:

$$\frac{V}{V_{DL}} = \frac{R_g T_I}{\bar{C}_{L\gamma}^* - \bar{C}_\gamma^*} \left(\frac{\partial \bar{\mu}_L^*}{\partial \bar{C}_{L\gamma}^*} \right)^{-1} \left(1 - \frac{V^2}{V_{DL}^2} \right) \left[1 - \exp \left(\frac{\Delta \bar{\mu}_{\gamma/L}^{A^*} - \Delta \bar{\mu}_{\gamma/L}^{B^*}}{R_g T_I} \right) \right]. \quad (3.1-12)$$

So far, a model for lamellar eutectic growth under steady-state conditions is proposed by adopting the interface kinetic models for concentrated alloys [79, 80] (i.e. equations (3.1-8)-(3.1-12)). The next step is to impose a negative temperature gradient for the growing lamellar eutectic interface in order to generate its instability concerning a eutectic dendrite. In the case of such purely thermal-controlled dendrite growth [74, 75], the thermal undercooling ΔT_T can be obtained from the IVANTSOV solution [81] as:

$$\Delta T_T = \frac{\Delta \bar{H}_f}{\bar{C}_p^L} \text{Iv}(P_T), \quad (3.1-13)$$

where $\Delta \bar{H}_f$ ($= f_\alpha \Delta \bar{H}_f^\alpha + f_\beta \Delta \bar{H}_f^\beta$) is the average latent heat of fusion, \bar{C}_p^L ($= f_\alpha \bar{C}_p^{L\alpha} + f_\beta \bar{C}_p^{L\beta}$) is the average specific heat of undercooled melts, $P_T = VR/2\alpha_L$ with α_L the thermal diffusion coefficient and R the dendrite tip radius is the thermal PÉCLET number. Equation (3.1-13) gives actually a relation between VR and ΔT_T . To find a unique solution, a second equation from the solvability theory [82, 83] is needed:

$$R = \left(\frac{\bar{\Gamma}}{\sigma_0 \varepsilon^{7/4}} \right) / [P_T \Delta \bar{H}_f \xi_T / 2 \bar{C}_p^L], \quad (3.1-14)$$

where $\xi_T = 1/(1 + a_T \varepsilon P_T^2)$ is a stability function, $\bar{\Gamma} = f_\alpha \bar{\Gamma}_{L\alpha} + f_\beta \bar{\Gamma}_{L\beta}$ is the average GIBBS-THOMSON coefficient while $\bar{\Gamma}_{Li} = \sigma_{i/L} V_m / \Delta \bar{S}_f^i$ and $\Delta \bar{S}_f^i$ is the average entropy of fusion of the i/L interface,

ε is the anisotropy coefficient, $\sigma_0 = 1/0.42$ the stability constant, and $a_T = 0.3$. For a given velocity V , R and ΔT_T are determined by equations (3.1-13) and (3.1-14).

The described combination of the lamellar eutectic model and the thermal dendrite growth model defines a total undercooling $\Delta T = \Delta T_i + \Delta T_T$. Consequently, λ , R and ΔT can be calculated for a given growth velocity V with the current eutectic dendrite growth model for concentrated alloys with NLPD (i.e. Eqs. (3.1-4)-(3.1-14)).

3.2 Model of Li and Zhou (LZ) for Dilute Alloys with Linear Phase-Diagram (LPD)

In the LI and ZHOU model (LZ) model for dilute alloys with linear phase diagram (LPD) [75], the TRIVEDI-MAGNIN-KURZ (TMK) model [68] is used to describe the lamellar eutectic growth. A second type of LPD in the TMK-model is introduced with constant and equal equilibrium partition coefficients k^e , which is a good approximation for the Fe-B eutectic alloy. The relations between the interface undercooling ΔT_i , the growth velocity V and the lamellar spacing λ is given by the minimum undercooling principle [76, 69]:

$$\lambda^2 V = \frac{K_1}{K_2}, \quad (3.2-1)$$

$$\lambda \Delta T_i = \frac{m_{L\gamma} m_{LFe_2B}}{m_{L\gamma} + m_{LFe_2B}} \left(1 + \frac{P}{P + \lambda \partial P / \partial \lambda} \right), \quad (3.2-2)$$

where

$$K_1 = 2 \left[\frac{\bar{\Gamma}_{L\gamma} \sin \theta_\gamma}{f_\gamma m_{L\gamma}} + \frac{\bar{\Gamma}_{LFe_2B} \sin \theta_{Fe_2B}}{f_{Fe_2B} m_{LFe_2B}} \right], \quad (3.2-3)$$

$$K_2 = \frac{1-k}{f_\gamma f_{Fe_2B} D_L} (P + \lambda \partial P / \partial \lambda), \quad (3.2-4)$$

$$P = \sum_{n=1}^{\infty} \left(\frac{1}{n\pi} \right)^3 \left[\sin(n\pi f_\gamma) \right]^2 \frac{P_n}{\sqrt{1 + \psi p_n^2} - 1 + 2k}, \quad (3.2-5)$$

$$P + \lambda \partial P / \partial \lambda = \sum_{n=1}^{\infty} \left(\frac{1}{n\pi} \right)^3 \left[\sin(n\pi f_\gamma) \right]^2 \left[\frac{P_n}{1 + \sqrt{1 + \psi p_n^2}} \right]^2 \frac{P_n}{\sqrt{1 + \psi p_n^2}}. \quad (3.2-6)$$

Here $p_n = 2n\pi/P_e$, $\psi = 1 - V^2/V_{DL}^2$, k is the velocity-dependent non-equilibrium partition coefficient, $m_{L\gamma}$ and m_{LFe_2B} are the slopes of kinetic liquidus which are given by [82, 83]:

$$k_{\alpha} = k_{Fe_2B} = k = \frac{\frac{V}{V_{DL}^I} + k^e \psi}{\frac{V}{V_{DL}^I} + \psi}, \quad (3.2-7)$$

$$m_{L_i} = \frac{m_{L_i}^e}{1-k^e} \left[1-k + \ln \frac{k}{k^e} + \frac{V}{V_D} (1-k)^2 \right] \quad (i = \gamma, Fe_2B). \quad (3.2-8)$$

The combination of equations (3.2-1)-(3.2-8) together with the thermal dendrite growth model (3.1-13) and (3.1-14) lead to the LZ eutectic dendrite growth model for dilute alloys with LPD. In particular, the LZ model [75] is extended by taking into account non-equilibrium solute diffusion (ψ in equations (3.2-5)-(3.2-7)) and non-equilibrium interface kinetics (equations (3.2-7) and equations (3.2-8)). To put it more simply, the only difference between the current and the LZ model is whether dilute alloys with LPD are assumed or not.

3.3 Kinetic Liquidus Slopes for Large Undercoolings

Figure 3-2 shows the evolutions of equilibrium (kinetic) liquidus slopes $m_{L_{\gamma}}^e$ and $m_{L_{Fe_2B}}^e$ ($m_{L_{\gamma}}$ and $m_{L_{Fe_2B}}$) as a function of undercooling ΔT for the presented model of concentrated alloys with NLPD. An interesting result for the γ -Fe phase at high undercoolings is the fact that the kinetic liquidus slope $m_{L_{\gamma}}$ becomes smaller as the equilibrium liquidus slope $m_{L_{Fe_2B}}^e$.

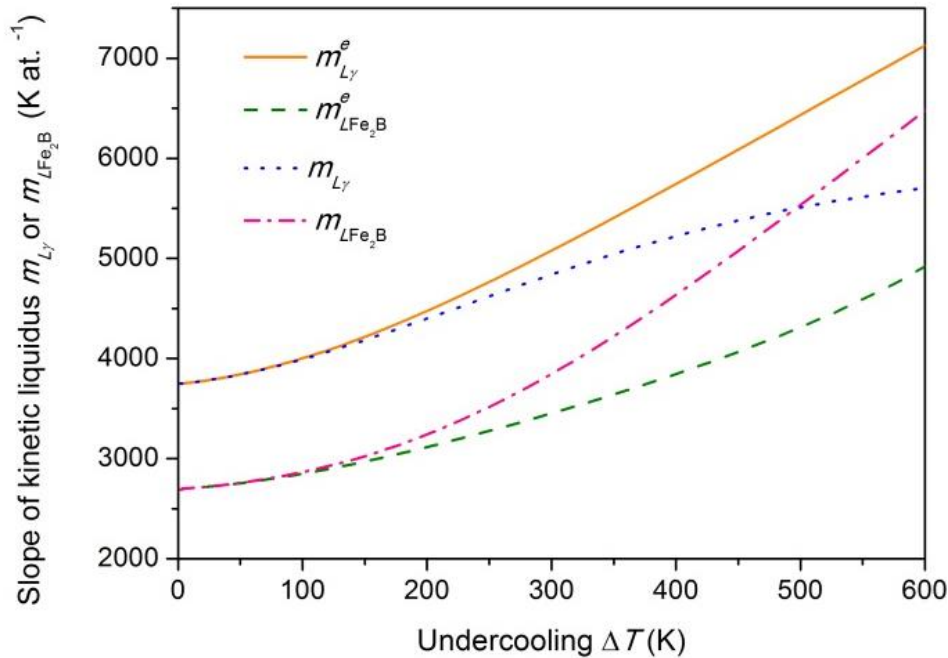


Figure 3-2: Evolution of equilibrium and kinetic liquidus slopes as a function of undercooling.

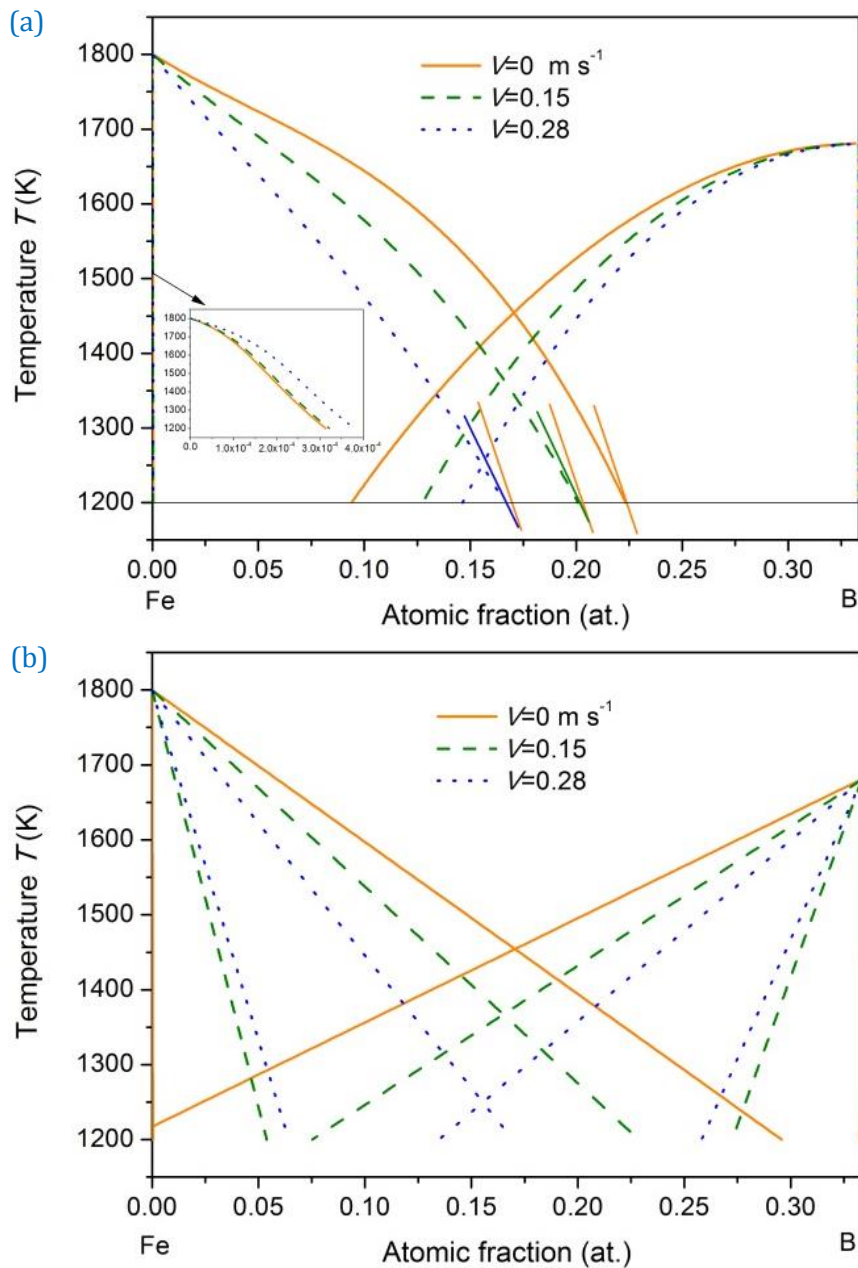


Figure 3-3: Kinetic phase-diagram of the eutectic Fe-B system in the case of concentrated alloys with NLPD (a) and dilute alloys with LPD (b).

Figure 3-3 shows the kinetic phase-diagram for the eutectic Fe-B alloy system in the case of concentrated alloys with NLPD (a) and dilute alloys with LPD (b). In the case of a given composition for concentrated alloys with NLPD, the kinetic liquidus of γ -Fe and Fe_2B decreases while the kinetic solidus of γ -Fe increases with the growth velocity V . For the stoichiometric compound Fe_2B occurs no solute trapping [78, 80] while the kinetic and equilibrium solidus coincide with each other. For a given low temperature (or high undercooling), e.g. $T = 1200$ K, $m_{L\gamma}$ decreases continuously from $m_{L\gamma}^e$ as the increase of V and thus $m_{L\gamma}$ is smaller than $m_{L\gamma}^e$ (tangents in Figure 3-3(a)). If both γ -Fe and Fe_2B are assumed as dilute alloys, their kinetic

liquidus for a given concentration decrease while their kinetic solidus increase with growth velocity V (Figure 3-3(b)). $m_{L\gamma} (m_{LFe_2B})$ thus is always larger than $m_{L\gamma}^e (m_{LFe_2B}^e)$. Furthermore the smaller slope of kinetic liquidus at high undercooling implies the importance to extend the eutectic theory to concentrated alloys with NLPD.

4 EXPERIMENTAL METHODS

This chapter explains the experimental methods to study rapid solidification for deep undercoolings. Most experiments are performed in a terrestrial electromagnetic levitator (1g-EML) which is shown in Figure 4-1. In order to investigate and reduce convectional effects some experiments were done in the TEMPUS¹ facility (μg -EML) under reduced gravity conditions during parabolic flight. Furthermore to vary fluid flow conditions, experiments were performed in a melt fluxing facility under influence of a high strength static magnetic field up to 6 T.

In addition, experiments with an infrared camera were performed as a feasibility study. This is especially interesting for low undercoolings ($\Delta T < 50 \text{ K}$) and low melting materials. Due to the maximum framerate of 850 *fps* the investigated growth velocities are limited to about 1 *m/s*.

The Microstructure of the as solidified samples is analysed with a scanning electron microscope (SEM) and Electron Backscatter Diffraction (EBSD) in order to examine the dendritic and eutectic structure including its crystallographic orientation.

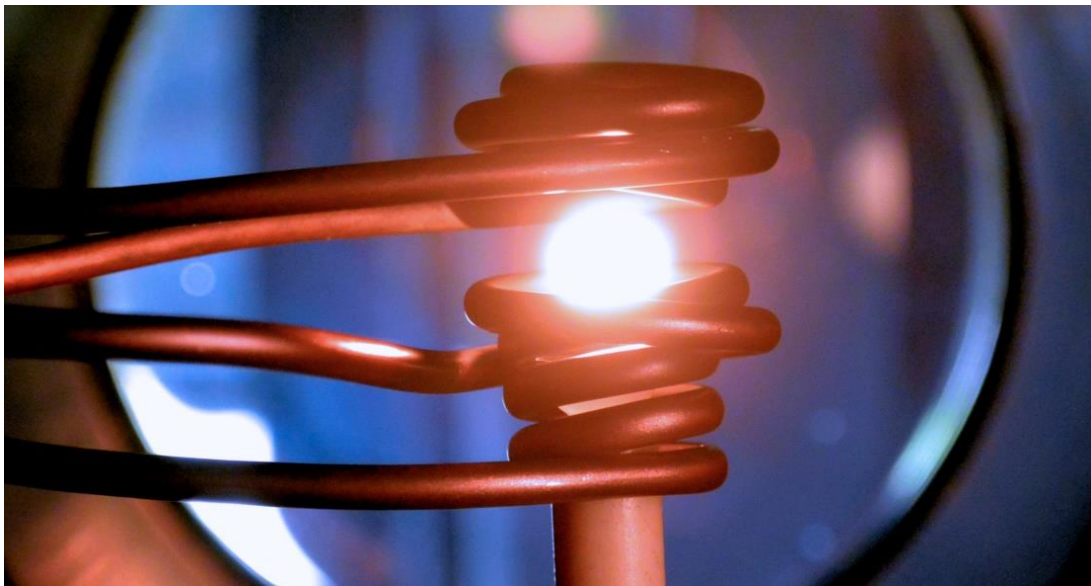


Figure 4-1: The photo shows a freely floating liquid iron sample at a temperature of about **1600 °C**. A water-cooled copper coil generates a high-frequency magnetic field, in which a seven-millimetre iron droplet levitates.

4.1 Electromagnetic Levitation (1g-EML)

The electromagnetic levitation (EML) technique [3] is an experimental method to deeply undercool electrically conductive materials (e.g. metallic melts) far below their equilibrium melting temperature and allows direct observation (*in-situ*) of the solidification process. Even highly reactive materials can be processed. This containerless technique makes it possible to avoid heterogeneous nucleation on container walls. By the use of high purity materials under

¹ Tiegelfreies Elektro-Magnetisches Prozessieren unter Schwerelosigkeit (TEMPUS)

clean environmental conditions it is possible to reach deep undercoolings up to 300 K prior to solidification. The vacuum-chamber is evacuated to 10^{-7} mbar and backfilled with high-purity helium (6N) to a few hundred mbar in order to limit evaporation of the sample. The transformation process of the undercooled liquid phase into the solid phase leads to a visible contrast between solid and liquid due to the release of latent heat during rapid solidification. The advancement of the solidification front is recorded by a high-speed video camera. Figure 4-2 shows schematically an EML experimental setup. The facility consists of a water-cooled copper levitation coil which creates an alternating magnetic field due to an alternating current I (≈ 400 A) and high voltage (≈ 100 V) at high frequency (up to 300 kHz). The resulting magnetic field amplitude H_0 is about 10^5 A/m. In general, a high frequency magnetic field induces an eddy (current) field in an electrically conducting sample. Particularly, the magnetic field induces a voltage $U_{ind} \sim f \cdot H_0$ and an eddy current $j_{ind} \sim \sigma \cdot f \cdot H_0$ in the metallic sample with the electric conductivity σ . The interaction between the sample and the magnetic field can be described as followed. To consider the MAXWELL equations, a temporal variation of a magnetic field $-\partial \vec{B} / \partial t = \vec{\nabla} \times \vec{E}$ induces eddy currents in the sample which react back on the source of the magnetic field (LENZ's law) and create a magnetic field which is counter directed to the primary field. That results in a repulsive LORENTZ force $\vec{F}_L = -\vec{\nabla}(\vec{m} \cdot \vec{B})$ between the levitation coil and the sample, where \vec{m} is the magnetic dipole moment induced in the sample. In other words, the sample behaves like a diamagnet and is repelled by the coil. The LORENTZ force acts on each point of the sample surface, while it is zero at the north and south pole. In the case of a levitating sample, the LORENTZ force is sufficient to compensate the gravitational force $\vec{F}_G = m \cdot \vec{g}$, where m is the mass of the sample and \vec{g} is the gravitational acceleration. The levitated sample can be assumed as a droplet-like head of liquid which is hold mainly on its equator at the surface where the LORENTZ force is strongest. Stable levitation conditions depend on the coil geometry and sample properties (like electrical conductivity, diameter and mass). It should be mentioned, that as a side effect of the strong electromagnetic field which is necessary for lifting the sample against gravity, strong electromagnetic stirring is applied. This forced convection results in fluid flow velocities up to 0.3 m/s [9] in the liquid sample.

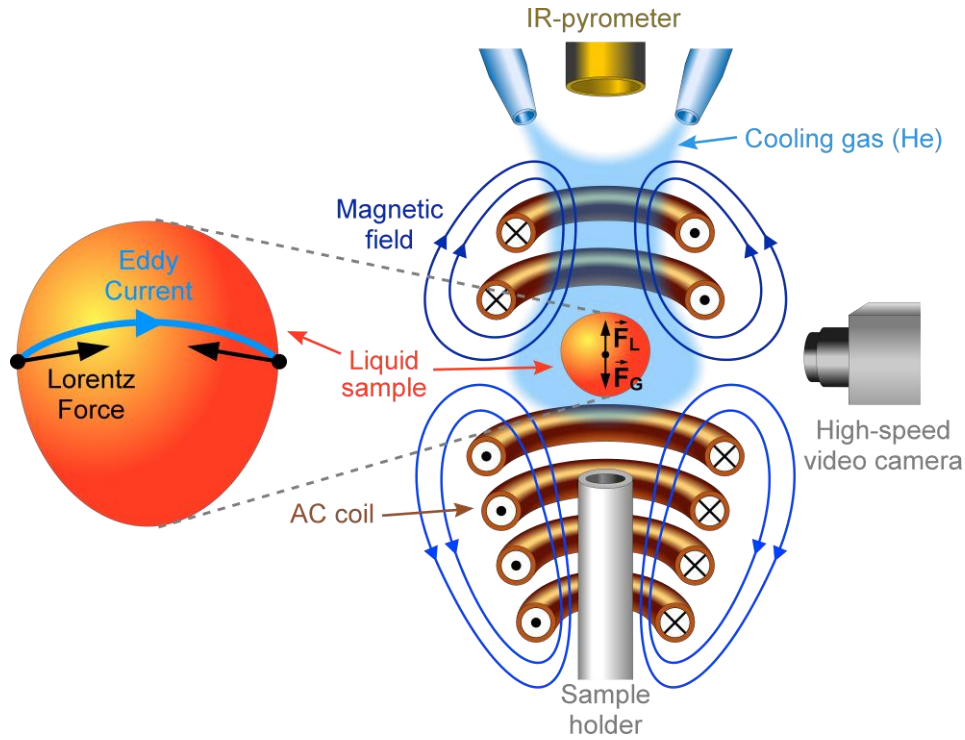


Figure 4-2: Schematic view of an electromagnetic levitation facility. The sample is processed under noble gas atmosphere in a vacuum chamber. Levitation and heating are achieved by an electromagnetic field produced by high frequency alternating currents flowing through a water-cooled copper coil. The actual force which lifts the sample against gravity F_G is the LORENTZ-force F_L which acts mainly at the equator on the surface. The temperature is measured contactless with an infrared-pyrometer.

The electromagnetic levitation and inductive heating are coupled and appear simultaneously in EML. The levitation force is proportional to $j_{ind} \cdot H_0$ whereas the power of absorption $P_{Ohm} = U_{ind} \cdot j_{ind}$ is proportional to H_0^2 . In order to achieve an experimental optimization for levitation and inductive heating, the amplitude of the coil current and the sample mass can be adjusted.

Samples for an EML experiment are about 1 g in weight and 6 – 7 mm in diameter. The temperature is measured contactless at the top of each sample by a two-color pyrometer with a sampling rate of 100 Hz. The accuracy of the pyrometer is approximately ± 3 K. The emissivity ε of the sample material is unknown. Using the pyrometer at a constant emissivity ε of 0.2 requires a correction of the measured temperature values T^{pyr} . A temperature T can be calculated by using following equation:

$$\frac{1}{T} = \frac{1}{T^{pyr}} + \frac{1}{T_L} - \frac{1}{T_L^{pyr}},$$

where T^{pyr} is the temperature recorderd by the pyrometer, T_L^{pyr} is the measured liquid temperature by the pyrometer and T_L is the liquidus temperature taken from the literature

phase diagram. The corrected temperatures can be calculated and the undercooling ΔT can be extracted from the temperature time profile.

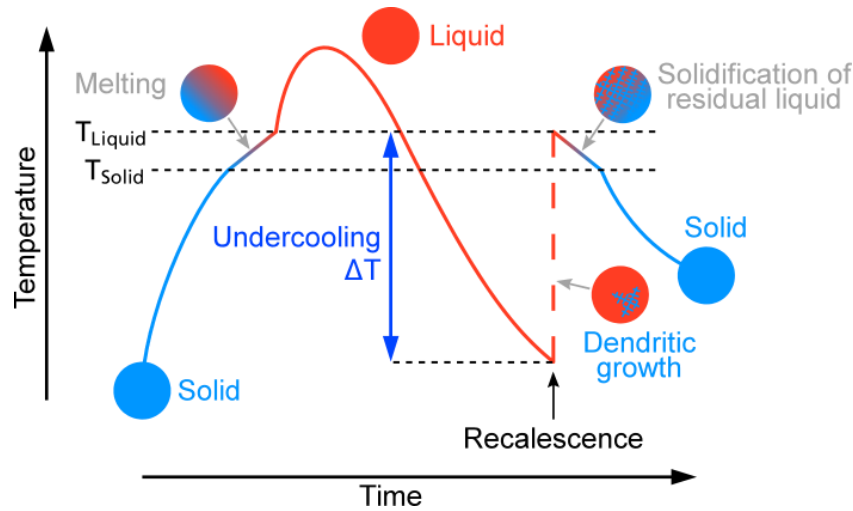


Figure 4-3: Schematic temperature-time profile measured in an undercooling electromagnetic levitation experiment. First the sample levitates in solid state, followed by melting, overheating in liquid state, undercooling until rapid solidification (recalcescence) occurs spontaneously with dendritic growth, solidification of residual liquid, and ends up in solid state again.

Figure 4-3 shows a schematic temperature-time profile for a typical undercooling experiment. The solid sample is levitated and at the same time inductively heated. By increasing the power the sample starts to melt. Once the sample is completely molten the temperature increases rapidly. This point in the temperature-time profile is used as a reference for the liquidus point for calibrating the temperature measured by the pyrometer. Overheating is applied to get rid of pollutions and potential oxide layers. The sample is cooled by reducing the power to a minimum and additionally by a diffuse He-gas flow. While the sample is undercooled spontaneous nucleation takes place. A primarily formed crystal nucleus grows rapidly and during subsequent growth latent heat is released. During this recalcescence a contrast is visible between the dark undercooled liquid and bright solidified material which can be recorded by a high-speed camera. After recalcescence a portion of the sample is solidified into a dendritic network. These dendrites thicken until the residual liquid solidifies.

4.2 Electromagnetic Levitation under Reduced Gravity (μg -EML)

Concerning terrestrial EML, the electromagnetic field necessary for levitation induces strong convective fluid flow inside the melt due to electromagnetic stirring. The resulting fluid flow velocity in 1g-EML is estimated to be around 0.3 m/s [9]. In order to verify the influence of convection on the growth velocity and morphology, experiments were performed under reduced gravity conditions in micro-gravity (μg) during parabolic flight missions using the TEMPUS² facility [84] aboard an *AIRBUS A300 Zero-G* airplane (cf. Figure 4-4). The experimental setup of

² Tiegfreeses Elektro-Magnetisches Prozessieren unter Schwerelosigkeit (TEMPUS)

an μg -EML is similar to the 1g-EML. The main difference in the TEMPUS facility compared to terrestrial EML is the decoupling of positioning and heating due to superposition of a weak quadrupole positioning field (150 kHz) and a strong dipole heating field (400 kHz). During solidification the dipole heating field is turned off, resulting in a low remaining fluid flow velocity of about 0.05 m/s [9] and therefore one order of magnitude lower as in terrestrial 1g-EML.



Figure 4-4: Left image: TEMPUS facility for containerless electromagnetic levitation. Right image: AIRBUS A300 Zero-G airplane by NOVESPACE [85].

To achieve micro-gravity for about 22 s the airplane follows a parabolic flight manoeuvre which is shown schematically in Figure 4-5. The aircraft initially climbs up at an angle of 47 degrees (injection point) following a parabolic trajectory until the pilot pulls out the nose with an angle of 42 degrees downwards (recovery point). Under these circumstances the remaining acceleration forces are in the order of $10^{-3} g$ during 22 s of reduced gravity. The parabolic flight campaigns are performed by the company NOVESPACE from Bordeaux, France.

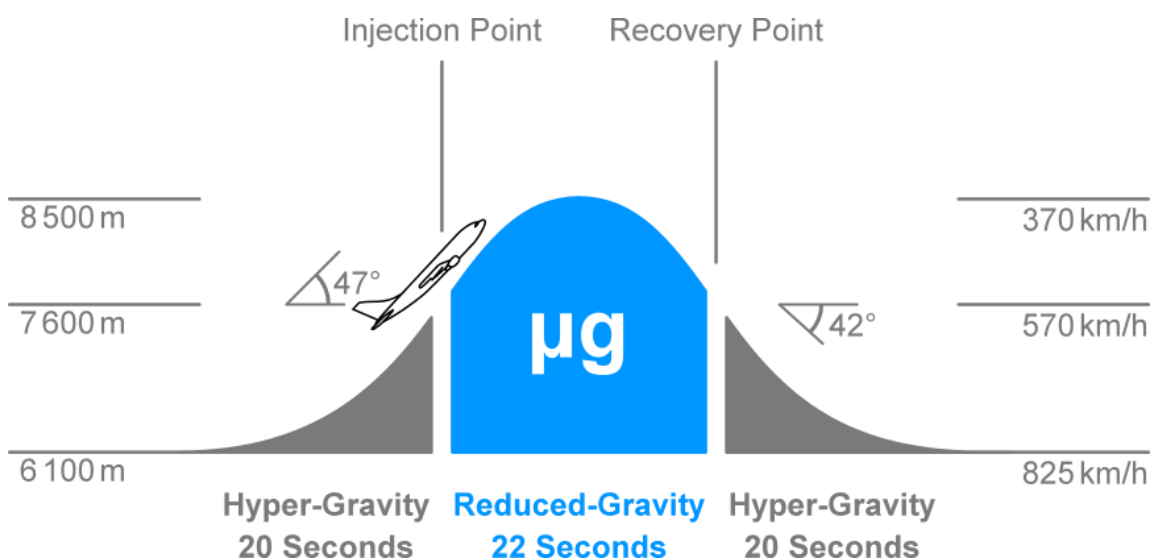


Figure 4-5: Schematic view of a parabolic flight manoeuvre

The TEMPUS facility was already flown three times aboard *Space Shuttle* Spacelab missions (IML-2, MSL-1 and MSL-1R), five sounding rocket flights with the carrier TEXUS³, and more than 2000 parabolas during several parabolic flight campaigns. Since September 2014 an EML is also installed at the *International Space Station* (ISS). The Fe-10 at.% B alloy was qualified within this thesis due to a parabolic flight experiment to be a sample for batch 2 in 2015/16 aboard the ISS as part of the MAGNEPHAS project.



Figure 4-6: German astronaut ALEXANDER GERST installing and switching on the EML-ISS (picture by ESA⁴ [86]) in Nov. 2014 aboard the International Space Station (picture by NASA⁵ [87]).

³ Technologische Experimente unter Schwerelosigkeit (TEXUS)

⁴ European Space Agency (ESA)

⁵ National Aeronautics and Space Admistration (NASA)

4.3 Melt-Fluxing in a Static Magnetic Field (MF)

Beside 1g-EML and μg -EML it is possible to achieve different fluid flow conditions by using a strong magnetic field. A static magnetic field reduces the fluid flow due to magnetic damping in conductive materials which could be shown by YASUDA et al. [88].

In 1939 BARDENHEUER and BLECKMANN published first melt fluxing experiments (MF) of undercooling Fe and Ni bulk melts. With this technique they were able to undercool samples to about $\Delta T/\Delta T_E \approx 0.18$. Later on, TURNBULL et al. [89] produced an amorphous $\text{Pd}_{40}\text{Ni}_{40}\text{P}_{20}$ sphere after fluxing the melt in B_2O_3 with cooling rates of just a few K/s . In 1987, FLEMINGS et al. [90] combined the MF with the EML technique and investigated dendritic growth of undercooled Ni-Sn alloys.

YECKEL and DERBY did three-dimensional simulations of the flow induced by transient acceleration (g-jitter) in microgravity crystal growth [91]. In most cases, the application of a magnetic field suppresses flow oscillations, but for transverse jitter at intermediate frequencies, flow oscillations are increased.

ZHANG et al. combined EML with a superconducting magnet [92]. They could show by investigations of Co-Cu alloys which show a metastable miscibility gap that the effect of a static magnetic field of 2 T is similar to that of reduced gravity during parabolic flights.

The melt fluxing experiments in a static magnetic field for this work were performed together with Professor Dr. JIANRONG GAO at the *Key Laboratory on Electromagnetic Processing of Materials* of the *North-Eastern University* (Shenyang, China). A static magnetic field was applied with a superconducting magnet up to 6 T. Figure 4-7 shows the experimental setup. The sample is covered with melt flux on an Al_2O_3 sample holder. The temperature is measured by an infrared-pyrometer while the solidification is recorded by a high-speed video camera (HSC) with a telelens and prism. Due to the high magnetic field the HSC has to be placed at a safe distance which leads to a low resolution of the videos to about $64 \times 64 \text{ px}$ corresponding to a sample diameter of about 7 mm.

B_2O_3 , DURAN and PYREX are used as fluxing agents due to their ability of high solubility for metal oxides at high temperatures. Those materials act as impurity absorber.

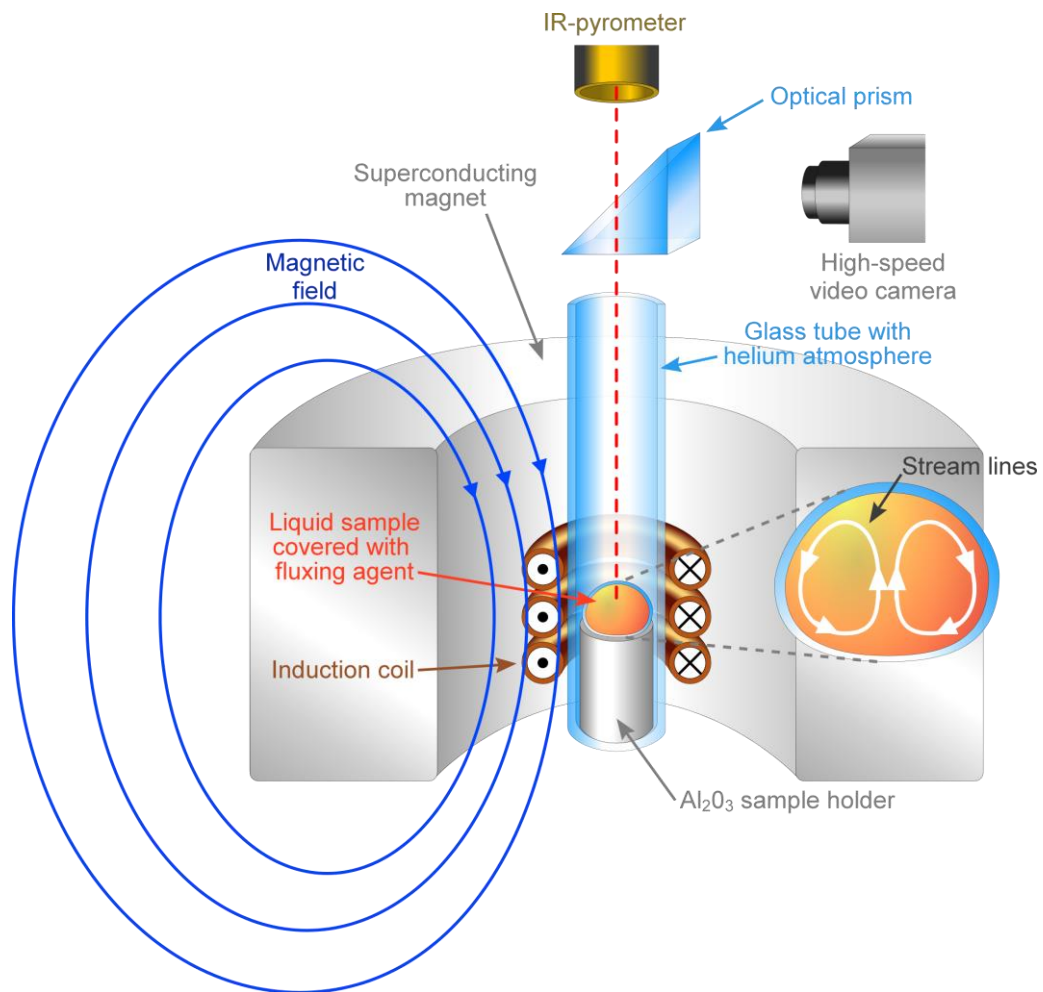


Figure 4-7: Schematic experimental setup for melt fluxing experiments in a static magnetic field produced by a superconducting magnet. The estimated flow field inside the liquid sample is indicated as stream lines.

4.4 Infrared Camera (IRC) versus High-Speed Camera (HSC)

Levitation experiments for observing the solidification process in undercooled melts is mostly done by using high-speed video cameras (HSC) working in the spectrum of visible light. In the past, infrared cameras (IRC) were operating with too low frame rates for observing solidification processes in metals. Recent developments make fast IRC available as a powerful tool for new findings. Especially the temperature distribution in the liquid and the solid during the solidification is of great interest. The low undercooling regime ($\Delta T < 50 K$) becomes accessible for growth velocity measurements due to the enhanced contrast. Additionally, low melting materials can be investigated which show no intensity in the visible light regime.

Within this thesis the possibility of using an infrared camera (IRC) was investigated. Figure 4-8 shows the experimental setup. The IRC *ImageIR 8380*, *InfraTec Thermografiesystem* was placed directly in front of the recipient. This position was chosen to minimize the distortion in the infrared domain trough the glass window of the recipient. This problem occurs not in visible light while the HSC *Photron FASTCAM SA5* was placed on the left.

Observing infrared light through a glass-window needs special filtering because glass absorbs the most part of the infrared spectrum. The *ImageIR 8380* was operated with a filter called *25mm DGF(900 – 2500)°C 25 μ m*. Due to the working distance of *0.5 m* it was necessary to adjust the image section to a smaller size which leads to a lower resolution of the videos. By using a telephoto lens the resolution could be optimized. Therefore the maximum frame rate was *800 fps*. The HSC was operated with *1000 fps*. Thus the observation is not synchronised.

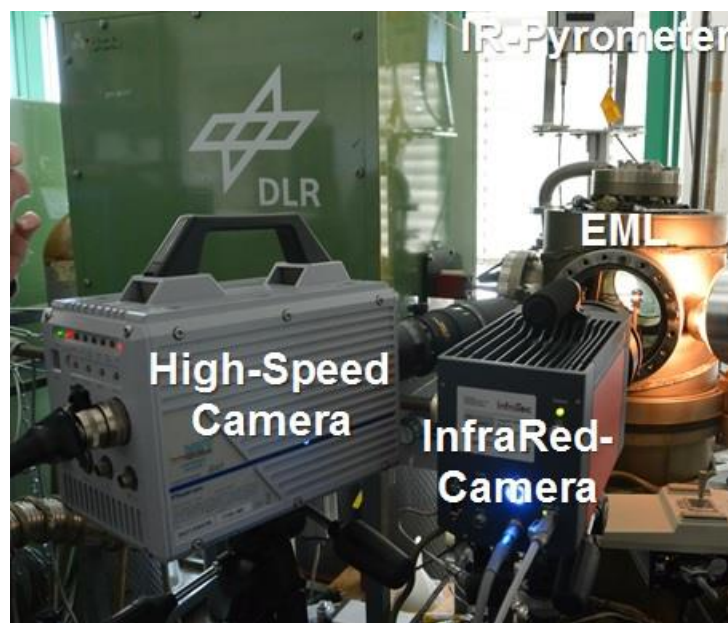


Figure 4-8: Experimental setup to observe the solidification process simultaneously with a HSC and an IRC in front of an EML.

Figure 4-9 shows snapshots of a solidifying Fe_2B sample recorded simultaneously the HSC and IRC. In the upper row (HSC) the solid phase is light and the liquid phase is dark grey. In the IRC snapshots (lower row) it is possible to observe the propagating of the solidification front and the temperature information.

The emissivity ε of the solid and liquid phase differs and is unknown. The calculation of the temperature by the computer software is done according to the STEFAN-BOLTZMANN-law. A calibration of the IRC was performed to the liquidus temperature of the used sample material. However the spherical shape of the sample leads to a misinterpretation of the temperature. This results in a higher temperature at the outer part of the spherical sample.

In conclusion this study demonstrated the possibility of observing solidification processes with an IRC. Low-melting materials like Al-Cu alloys cannot be investigated with common HSC in visible light but show remarkable contrast in the infrared. Furthermore detailed information about the heat distribution in the melt and during the solidification could be observed and is of great interest for future experiments. Nevertheless using IRC is still limited to growth velocities up to 1 m/s due to the maximum frame rate of 850 fps .

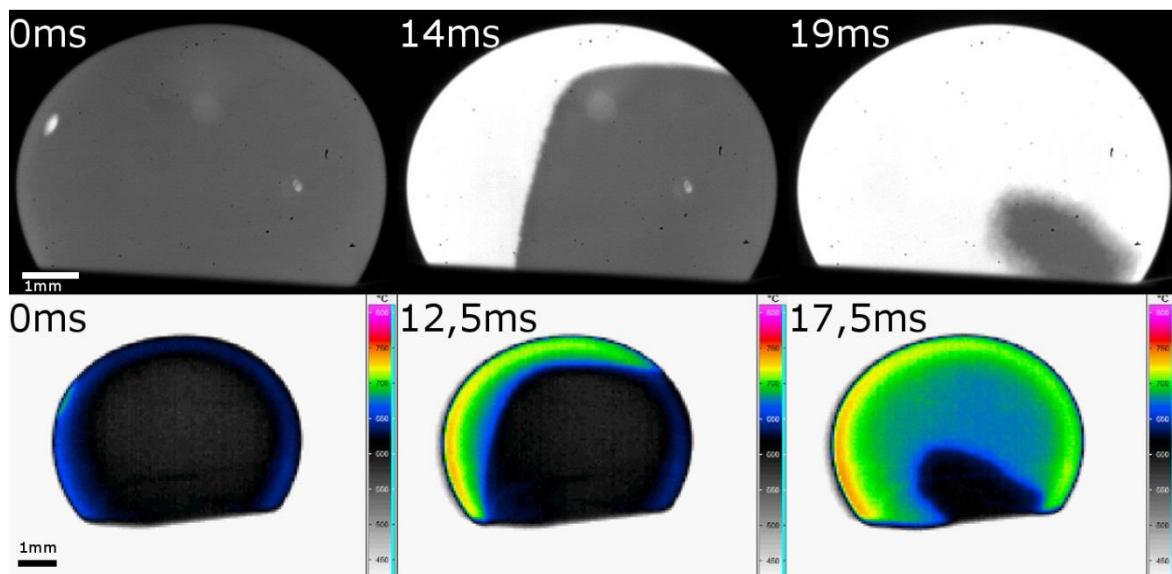


Figure 4-9: Snapshots of a solidifying Fe_2B sample. Upper row: High-speed camera at 1000 fps . Lower row: Infrared camera at 800 fps .

4.5 Microstructure Analysis

An optical microscope (ZEISS AXIO IMAGER.A2M) is used for imaging the solidified sample surface to find correlations of the observed solidification patterns which were recorded *in-situ* by the high-speed video camera.

The maximum magnification of a light microscope ($\approx 1000\times$) is limited by the wavelength of visible light (400 – 700 nm) used for illumination. Electrons have a much shorter wavelength which means higher resolution and greater magnification. In this work, a scanning electron microscope (SEM) is used to analyse the sample surface structure and bulk microstructure of the as solidified samples. The *LEO 1530 VP GEMINI* SEM used for analysis is operating under high vacuum conditions with a focussed electron beam (up to 30 kV energy) which is produced by a SCHOTTKY field emission gun. The sample is scanned in a raster pattern by the electron beam while the scattering and reflection are detected. There are three main effects which occur while the electron beam interacts with the sample, first the reflection of high-energy electrons by elastic scattering, second the emission of secondary electrons by inelastic scattering, and third the emission of electromagnetic radiation. Consequently the SEM is equipped with detectors for back scattered electrons (BSE), secondary electrons (SE), and X-rays (EDX). The image of a sample is reconstructed by a computer...

The electron backscatter diffraction (EBSD) is a powerful microstructure analysis technique in the field of solidification [93]. It is used to investigate the crystallographic orientation of the microstructure (dendritic and eutectic). The EBSD (*OXFORD INSTRUMENTS HKL EBSD system*) is equipped with a backscatter diffraction detector.

The analysis of the composition can in principle be investigated by energy dispersive X-ray spectroscopy (EDX). However, in the case of boron this doesn't work because of inherent physical effects and technical reasons. Inherent physical problems for the analysis of light elements with EDX are the low fluorescence yield, absorption and peak overlaps with L, M and N lines of heavier elements [94].

5 SAMPLE SYSTEM: IRON-BORON

In this chapter the binary Fe-B metal-metalloid system, its properties, and sample preparation are described. The investigations concentrate at the Fe-rich side of the phase diagram.

The Fe-B alloy is used as a model system to investigate dendritic and eutectic solidification in Fe based alloy melts. The knowledge of the solidification behaviour and thermodynamic properties of Fe-B is of interest in several fields of material engineering. For example, Fe-B is a subsystem of the Nd-Fe-B alloys with superior magnetic properties. Also the high modulus TiB₂-reinforced steel composite is based on the Fe-B-Ti ternary alloy. Furthermore B is used for hardenability of steels. Fe-17 at.% B eutectic composition is a metallic glass builder.

5.1 Phase Diagram, Material Parameter, and Crystallographic Structure

The investigations in this study are done for the Fe-B metal-metalloid with Fe-1, 5, 10 and 17 at.% B at the Fe-rich side of the Fe-B phase diagram which is shown in Figure 5-1 [95]. The solidus-line is unknown. In this case the equilibrium partition coefficient k_E of B in solid Fe cannot be extracted from the phase diagram. In particular k_E is very small ($k_E \ll 1$). Referring to literature it should be in the order of 10^{-4} . Therefore k_E is a fitting-parameter which has to be matched with the measurements of $v(\Delta T)$ concerning the growth velocity modelling in this thesis.

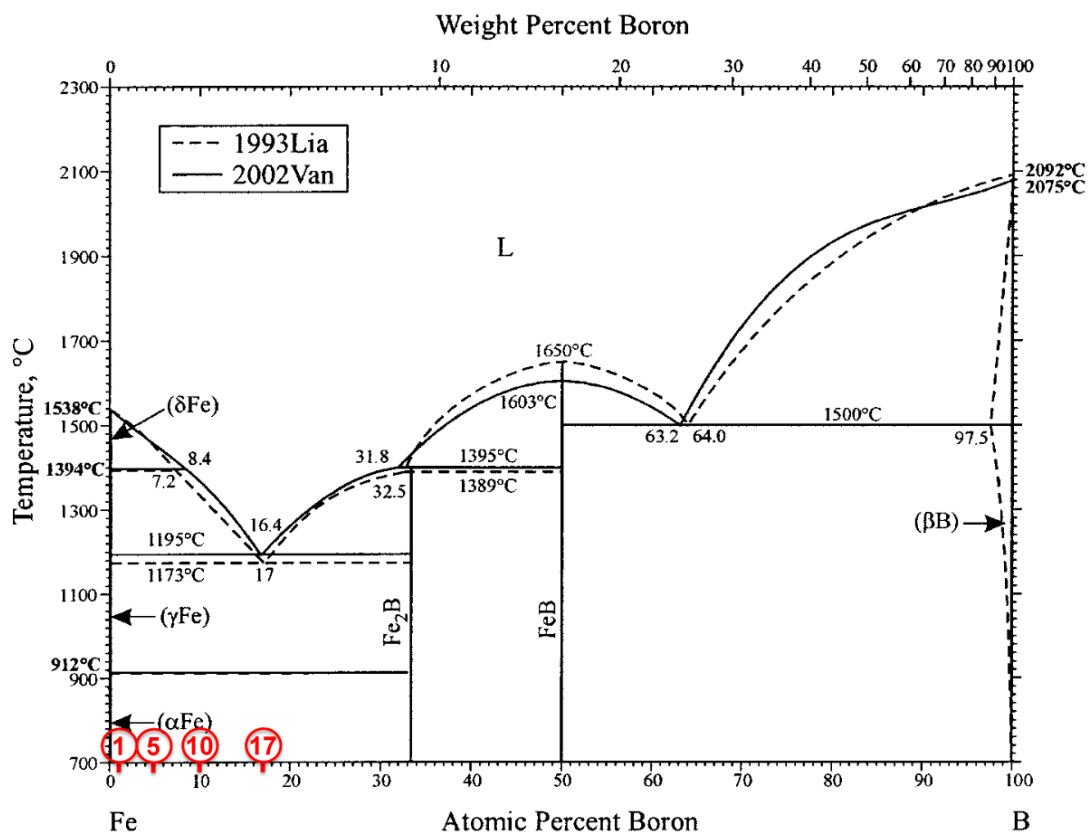


Figure 5-1: Fe-B phase diagram [95]

The approximation of the liquidus line gives the slope of the equilibrium liquidus m_L for each composition. The liquidus slope m_L can also be calculated by:

$$|\Delta H_m^{Fe}| = \frac{R \cdot T_L^2 (k_E - 1)}{m_L},$$

if $k_E = 0$. Table 5-1 summarizes the values for m_L of each alloy composition. In general, small variations of m_L have no influence on the interpretation of $v(\Delta T)$.

Table 5-1: Slope of the equilibrium liquidus m_L which is taken from the phase diagram m_L^{approx} and calculated m_L^{calc} .

Composition	T_L [K]	m_L^{approx} [K/at. %]	m_L^{calc} [K/at. %]
Fe-1 at.% B	1793	-17.14	-19.36
Fe-5 at.% B	1723	-16.56	-17.88
Fe-10 at.% B	1590	-15.47	-15.22

The solidifying δ -Fe phase has a cubic-crystal structure (body-centered cubic, bcc) as shown in Figure 5-2. Pure Fe and Fe-B with low B concentrations crystallizes in a bcc structure. As a result of the underlying surface energy anisotropy the solid grows along preferred directions. In the case of bcc-crystals the $\langle 100 \rangle$ growth direction is typical [10].

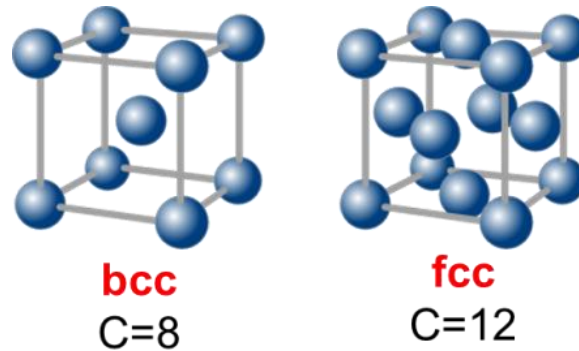


Figure 5-2: Body-Centered-Cubic (bcc) and Face-Centered-Cubic (fcc) with number of nearest neighbours C (coordination number)

Moreover in cubic crystals the solid grows dendritic-like with six primary trunks perpendicular to each other along one of the six equivalent $\langle 100 \rangle$ directions. Behind the advancing dendrite tip the secondary arms form the four conjugate $\langle 100 \rangle$ directions. The overall resulting shape of such a dendritic growing crystal is an octahedron which is shown in Figure 5-2. This shape can also be observed as an intersection with the surface of the spherical sample in the levitation videos for pure Fe. Phase-field simulations for equiaxed dendrites support this assumption of preferred growth directions and growth morphology [4].

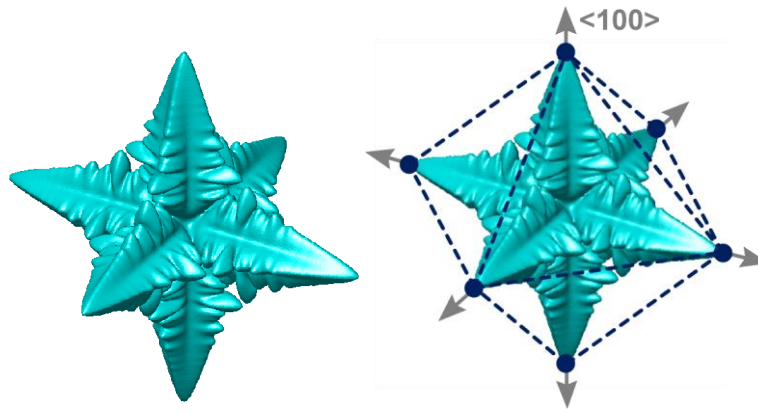


Figure 5-3: Phase-field simulation of a growing dendritic crystal [4] forming an octahedron with preferred $\langle 100 \rangle$ direction. The center of the octahedron (assumed nucleation point) put at the surface of a sphere leads to the following intersection pattern. This pattern can be observed during crystal growth in the case of solidifying pure Fe (cf. appendix A.1).

5.2 Sample Material and Preparation for Experiments and Microstructure Analysis

To achieve large undercoolings the use of high-purity raw materials is essential. Samples of Fe-1, 5, 10, and 17 at.% B were prepared from commercial high-purity elements 4N Fe and 5N B purchased from ALFA AESAR. Table 5-2 shows the specifications of Fe and B.

Table 5-2.: Raw materials used for sample preparation.

Element	Purity in %	Shape	Distributor
Boron B	99.999	Powder	ALFA AESAR
Iron Fe	99.995	Rod	ALFA AESAR

The 5N B (99.999%) powder consists of pieces differs in size and weight. The desired mass is collected by a minimum number of pieces and weight with a METTLER AT20 analytical microbalance.

The 4N Fe (99.995%) rod is cut by a BUEHLER IsoMet™ 4000 linear precision saw equipped with a corundum cutting blade. Afterwards the sample is polished by SiC (GRID 280 P4000) to the desired mass orientating at the B pieces. The polished Fe is finally cleaned in Isopropanol with an ultrasonic cleaner.

Typically 1200 mg samples are used for EML. Components were alloyed in an arc melting furnace previously evacuated (10^{-6} mbar) and subsequently filled with high purity Argon (6N) atmosphere (1 bar).

For *microstructure analysis* the as solidified samples after experiments have to be prepared properly for further investigation using a light microscope, SEM⁶ and EBSD⁷. The samples are

⁶ Scanning Electron Microscope (SEM)

⁷ Electron Backscatter Diffraction (EBSD)

cut by a diamond wire saw and embedded in a conducting amorphous material. The cross-section surface is polished by using SiC abrasive paper (GRID 280 P4000) followed by alumina and silica suspension to remove any residual damage due to cutting and grinding.

6 EXPERIMENTAL RESULTS AND DISCUSSION

In this chapter the experimental results are presented and discussed within current solidification models. The main focus of this thesis lies on the growth kinetics in the Fe-B system for dendritic growth (Fe-1, 5, 10 at.% B) and eutectic growth (Fe-17 at.% B) by measuring and modelling the growth velocity $V(\Delta T, U_0)$ as a function of undercooling ΔT influenced by different fluid flow conditions with varying fluid flow velocity U_0 .

During the investigations on the Fe-B binary system, the videos showed unexpected growth morphologies which changes if concentration, undercooling and fluid flow conditions are altered. Especially the observation of *bent growing dendrites* is significant.

The *error of the measured undercooling* ΔT is estimated as $\pm 5 K$ according to the unknown emissivity, the measurement accuracy of the infrared pyrometer, and the uncertainty of the temperature-time profile (caused by sample moving) which was used to determine the liquidus temperature as well as the maximum undercooling before rapid solidification (see chapter 4.1). The *error of the growth velocity* V differs from 5% up to 25% depending on the precision of the measured sample diameter ($\pm 0.1 mm$), the quality of the video (resolution), and the visibility of the full solidification process which is sometimes partially hidden because of the sample rotation during solidification. The videos are analysed to measure the growth velocity according to appendix A.1. For reasons of clarity no error bars are plotted in the graphs. However the scatter of data points represents the uncertainty of the measured data. The used models for calculation to describe the experimental results are in good agreement with experiments and show major trends which qualitatively reproduce significant effects like solute trapping. Some material and physical parameters are not well known, like the velocity dependent partition coefficient k , the stability constant σ , the anisotropy of the interfacial energy ε , and the kinetic growth coefficient μ_K , which were chosen as “best fit” parameters to describe the experimental results within the order of magnitude given by literature.

6.1 Growth Morphology and Microstructure

Figure 6-1 shows an overview of the observed growth morphologies for pure Fe, Fe-1, 5, 10 and 17 at.% B at low and high undercoolings. As described in section A.1 pure Fe solidifies in an octahedron shape where the intersection of the sample surface results in a rhombohedral pattern. With increasing B concentration the observed growth fronts change with respect to a regular shape, in contrast and sharpness.

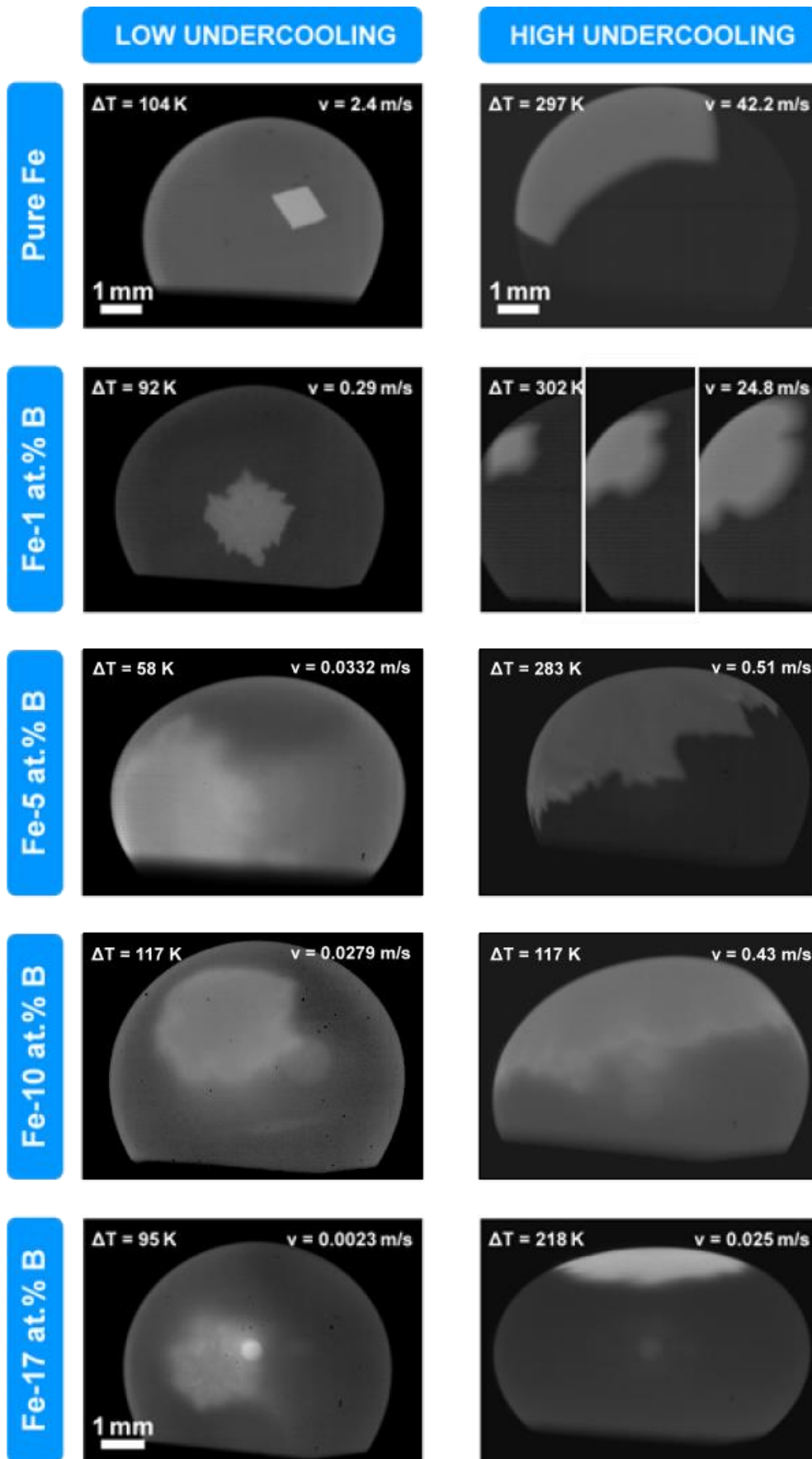


Figure 6-1: Growth morphologies for pure Fe, Fe-1, 5, 10, and 17 at.% B at low and high undercoolings.

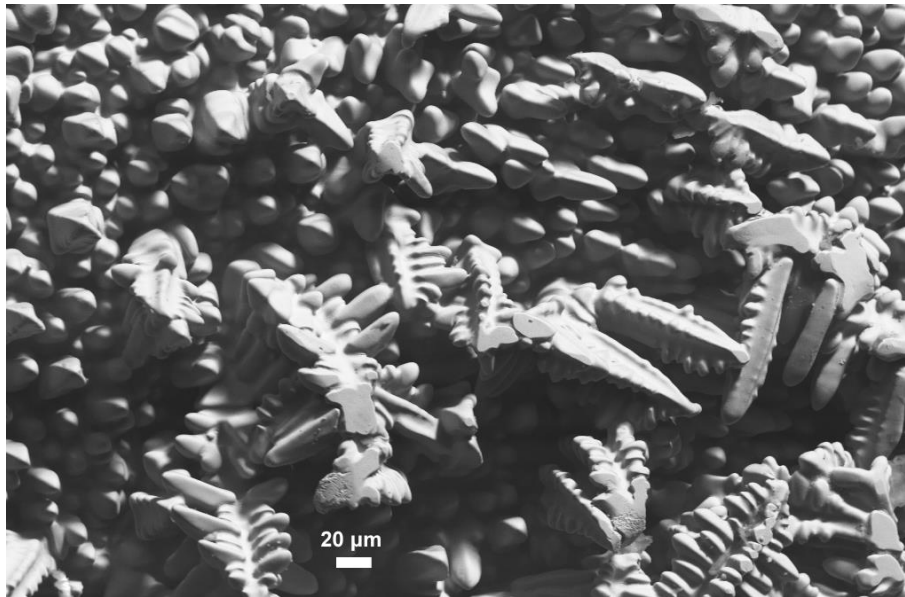


Figure 6-2: Surface of Fe-5 at.% B sample.

The microstructure of selected Fe-1, 5 and 10 at.% samples with different undercoolings were analysed in order to check for dendritic solidification. All investigated samples show a typical dendritic structure. Figure 6-2 shows the dendritic microstructure of a Fe-5 at.% B sample surface and Figure 6-3 the dendritic network of a Fe-10 at.% B sample solidified with an undercooling $\Delta T = 110 K$. The cross-section of the same Fe-10 at.% B sample implies curved dendrites which will be discussed in section 6.2.

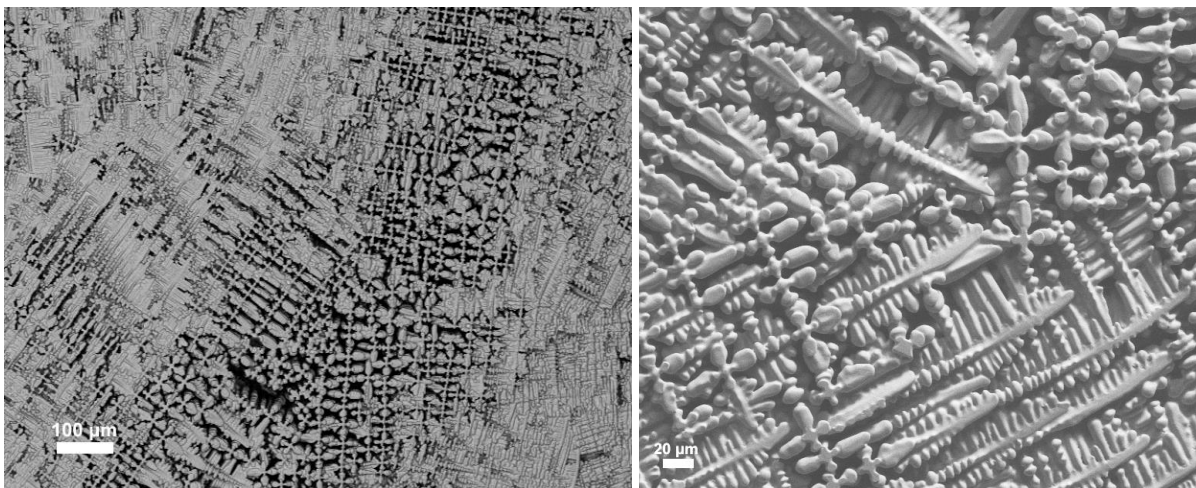


Figure 6-3: SEM image of a Fe-10at.% B 1g-EML sample surface shows a network of dendritic structure which was solidified at an undercooling of $\Delta T = 108 K$.

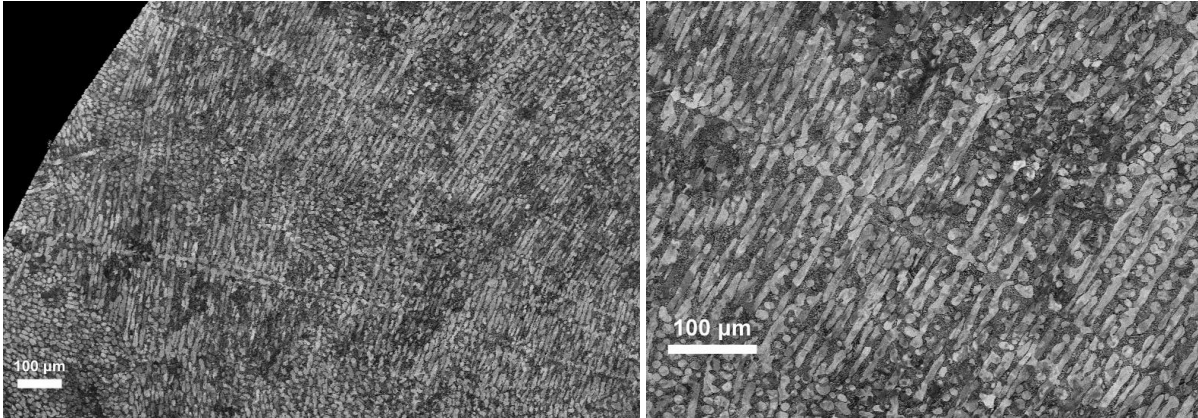


Figure 6-4: Cross-section SEM image of a Fe-10 at.% B sample.

Since the high speed video camera recordings show unique and significant solidification morphologies it should be possible to find matching patterns in the as solidified microstructure of the sample surface. Figure 6-7 shows an SEM image of a Fe-1 at.% B sample surface and the corresponding video recording solidification pathway. Similar patterns are visible in both images however a definite relation could not be found.

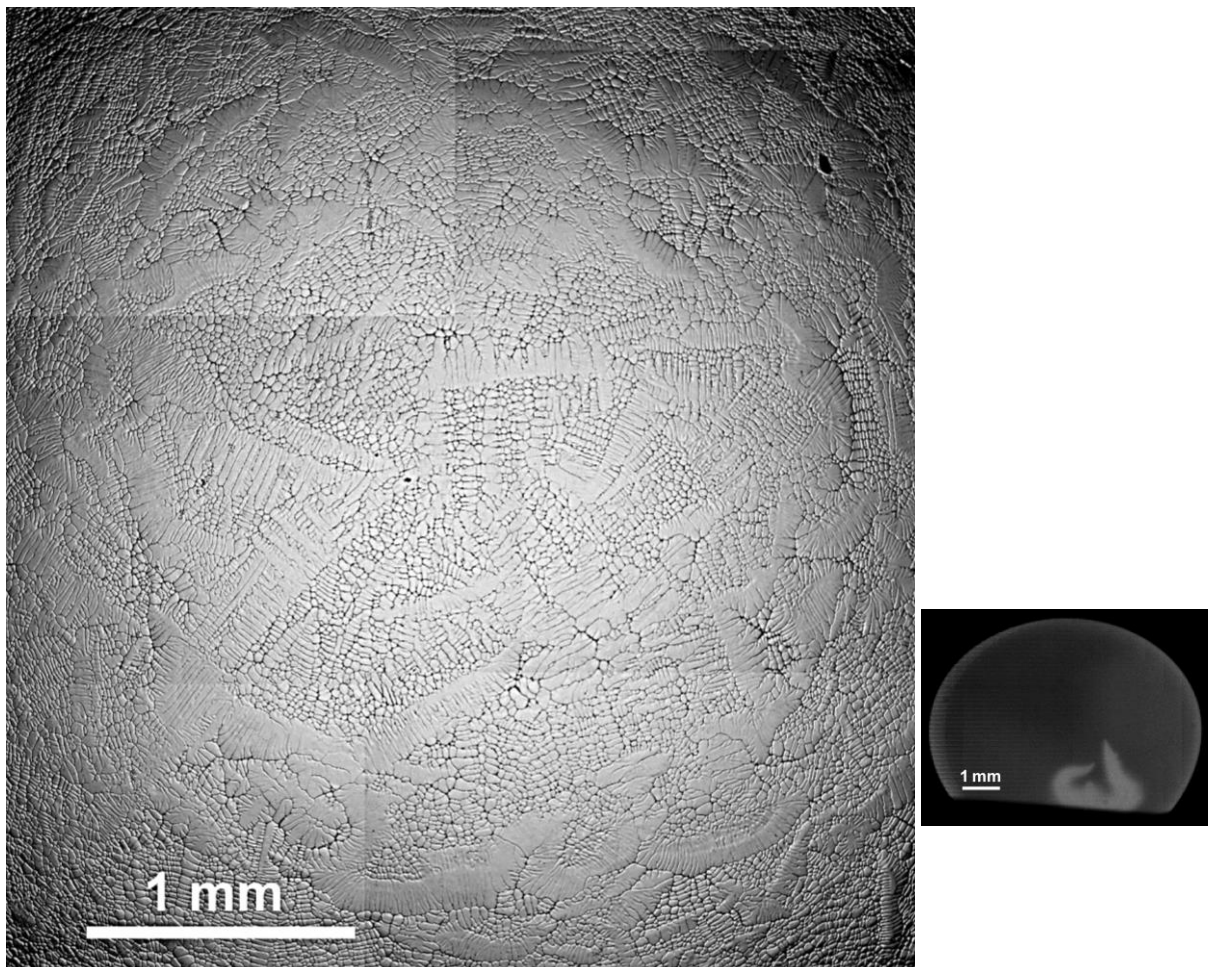


Figure 6-5: Sample surface (SEM) in comparison with the growth morphology visible in the high-speed video (snapshot) during solidification process. Similar structures can be observed but not identified/matched exactly.

6.2 Bent Dendrite Growth

Investigations of Fe with 1, 5, and 10 at.% B alloys show bent dendrite growth up to certain undercoolings in ground-based 1g-EML. Figure 6-6 illustrates typical results for the trajectories of the growing dendrites for each composition. The dendrite growth velocities are in the order of 10^{-1} m/s, therefore in the same order of magnitude as the fluid flow velocities in 1g-EML (0.3 m/s) according to R.W. Hyers [9]. In Table 6-1 the undercooling regimes and velocity results are listed. Different types of bent patterns are observed for the three compositions. The trajectories of the dendrite tips show spiralling (Fe-1 at.% B), zigzagging (Fe-5 at.% B) and U-turn (Fe-10 at.% B) growing dendrites. This behaviour is reproducible and characteristic for each composition.

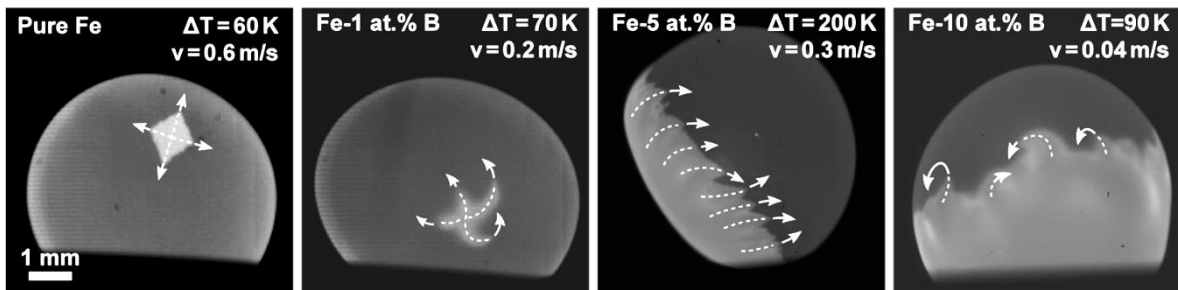


Figure 6-6: High-speed video images of electromagnetic levitated samples. The dark grey area is the undercooled liquid. The light grey region corresponds to the growing solid, which appears brighter due to the release of latent heat during rapid solidification. Arrows indicate the directions and trajectories of the growing dendrites showing straight (pure Fe), spiral like (Fe-1 at.% B), zigzagging (Fe-5 at.% B), and U-turn (Fe-10 at.% B) patterns in 1g-EML.

6.2.1 Bent growing dendrites under reduced gravity conditions

In order to verify the influence of convection on the growth morphology described in this study, parabolic flight experiments were performed under reduced gravity conditions using the TEMPUS facility [84]. In μ g-EML the fluid flow is about 0.05 m/s [9], one order of magnitude lower than in 1g-EML but still in the order of the slowest observed growth velocities. Figure 6-7 shows a bent growing dendrite under microgravity during parabolic flight. The undercooling ΔT is 98 K and the growth velocity v is about 0.14 m/s.

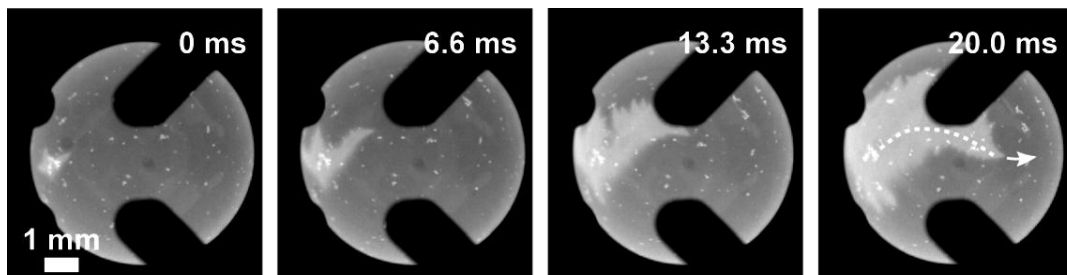


Figure 6-7: Snapshots of a undercooled solidifying Fe-1 at.% B liquid sample (dark grey) under reduced gravity conditions during parabolic flight showing bent dendrite growth (light grey).

Table 6-1: Highest undercoolings ΔT and corresponding dendrite growth velocities v for Fe-1, 5 and 10 at.% B where bent dendrite growth has been observed so far. Data for pure Fe is added for comparison.

		Undercooling ΔT [K]	Dendrite growth velocity v [m/s]	Observed pattern
1g-EML	Pure Fe	60	0.6	Straight, no bending
	Fe-1 at.% B	70	0.2	Spiral growth
	Fe-5 at.% B	200	0.3	Zigzagging
	Fe-10 at.% B	110	0.05	U-turn
TEMPUS ($\mu g - EML$)	Fe-1 at.% B	100	0.14	Spiral/Zigzagging

6.2.2 Microstructure of bent dendrites

Figure 6-8 shows the cross section microstructure of a bent dendrite with SEM and EBSD of a Fe-10 at.% B sample. The sample was processed in 1g-EML and solidified at an undercooling ΔT of 110 K.

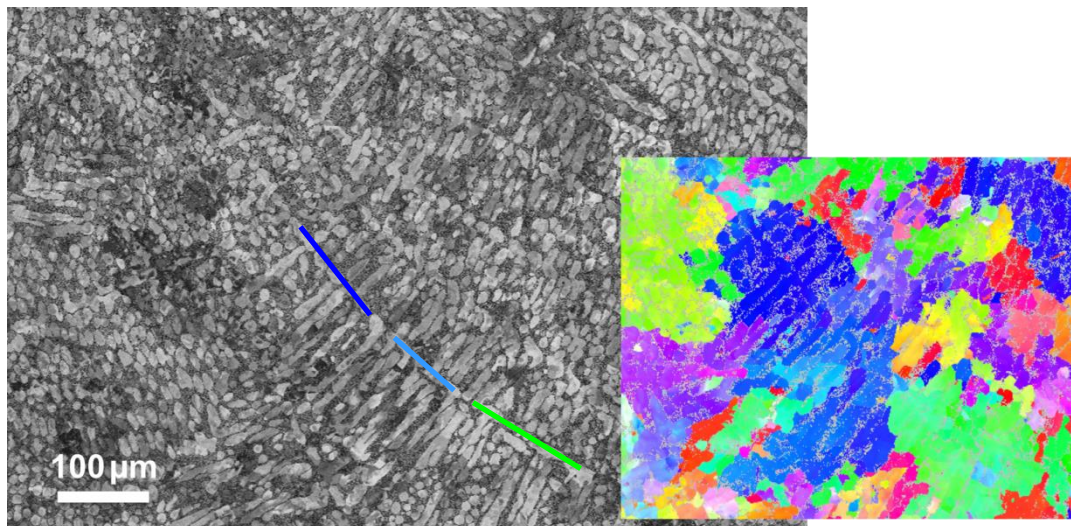


Figure 6-8: SEM and EBSD images of a cross section of Fe-10 at.% B solidified at an undercooling ΔT of 110K in 1g-EML showing a bent dendrite. The bending occurs mainly in the light blue region and at its transitions to the dark blue and green region, respectively.

6.2.3 Discussion

The trajectories of the dendrite tips show spiralling, zigzagging, and U-turn patterns for growing dendrites. So far we did not observe bent growing dendrites in any other metallic materials we investigated except multicomponent steel alloy. The findings appear to be relevant only for Fe-based alloys.

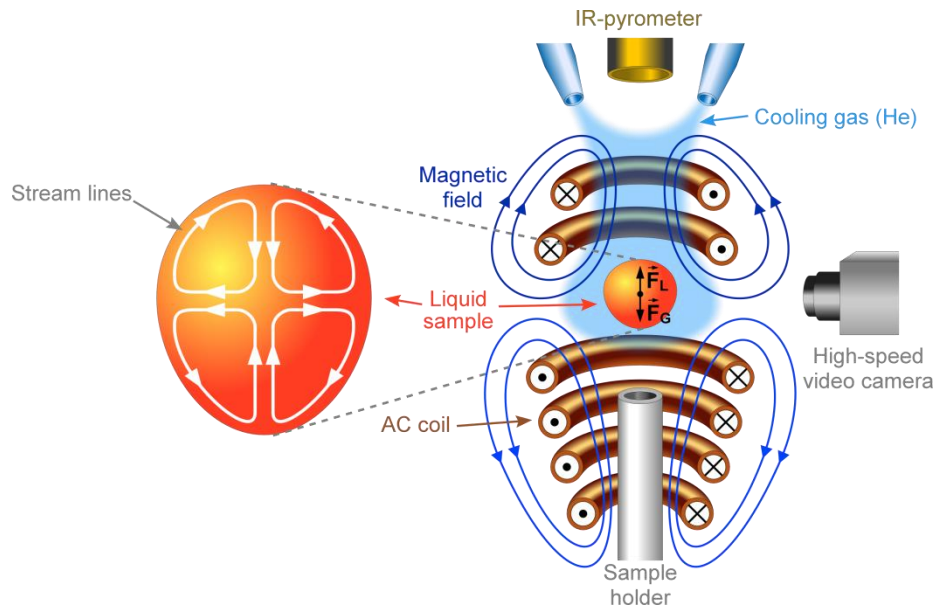


Figure 6-9: Schematic view of an electromagnetic levitation facility and levitated liquid sample with stream lines of fluid flow as indicated inside the melt [60]

In general, the dendritic solidification is a competition between heat/solute diffusion and surface energy [10]. B is poorly soluble in Fe [6]. According to growth models, a solute pile up exists at the solid-liquid interface of the dendrite tip, which slows down the dendrite growth velocity. Additionally, fluid flow influences the thermal and solute gradients ahead of the solid-liquid interface. In particular, the fluid flow velocity inside the melt in 1g-EML is in the same order of magnitude as the growth velocity itself. Figure 6-9 shows schematically the calculated fluid flow loops inside a laminar liquid sample according to P. Galenko et al. [60]. There seems to be a weak correlation between the fluid flow loops inside the liquid sample and the trajectories of the observed bent growing dendrites. More advanced investigations are needed to confirm this. Even under reduced gravity conditions with weaker fluid flow velocity the bent dendrite growth occurs for Fe-1 at.% B.

The microstructure of solidified samples showed that the effect of bent dendrites seems to be mainly sample-surface dominated. Up to now we were unable to find significant bent dendrites in the bulk microstructure of the samples. This could be explained due to coarsening and fragmentation of the as solidified microstructure. The cross section microstructure of solidified sample (Figure 6-8) indicates a stepwise breaking of the dendrite. Different crystal orientations of the grains are represented in different colors. A bending occurs mainly in the middle part (light blue region) and at its transitions to the dark blue and green region.

Regarding bent growing dendrites, one possible explanation was given by A. M. Mullis in 1999 [96] simulated dendritic bending and rosette formation during solidification under forced fluid flow perpendicular to the growth direction in a shearing flow. So far it is unclear whether the

presented experiments show an actual bent growth or deformation during growth. Phase-field modelling could reproduce the measured bending/deformation during solidification as reported by M. Yamaguchi and C. Beckermann [97]. They computed elasto-viscoplastic deformation of growing solid under a linear shear velocity field using the material point method. According to them, a phase-field model for simultaneous solid deformation and liquid flow is still not available.

Overall, the Fe-B system shows a weak anisotropy of the solid-liquid interfacial energy which may explain the observed bent dendrite growth and why this phenomenon was not reported in for instance Ni-B with a much higher anisotropy [98]. In addition, the described solidification interface morphology pattern by LIU et al. [99] in undercooled Co-24 at.% Sn eutectic melt demonstrated a transition to seaweed growth mode due to its weak interface energy anisotropy.

Another possible explanation for the observed bent dendrite growth is given by L. Gránásy et al. stating that impurities perturb the crystallization process by deflecting the dendrite tip during growth [100]. These foreign particles act as orientation pinning centers. In the melt a random field of impurities may exist leading to zigzagging or spiralling dendrites.

Our study has several limitations for the analysis of the dendrite growth morphologies. First, the strong oscillation and rotation of the liquid droplet has to be taken into account. In particular, the shape of the sample changes during crystallization. Second, the nucleation point appears statistically at a random point on the sample surface, so it is not possible to reproduce the same experimental conditions. Third, the fluid flow inside the melt is a nonlinear chaotic process and non-predictable. Fourth, the influence of impurities cannot be neglected.

6.2.4 Conclusion

The research shows bent growing dendrites under different fluid flow conditions. This phenomenon has been observed *in-situ*, as far as we know, for the first time in solidifying metals during levitation. In the case of Fe-10 at.% B in 1g-EML the effect was stronger than for Fe-1 and 5 at.% B. Bent dendrite growth could also be observed for Fe-1 at.% B under micro-gravity conditions during parabolic flight with weaker fluid flow compared to 1g-EML.

The cause of the observed bent dendrite growth is unclear. Impurities cannot be neglected and should be considered as a possible explanation to the growth behaviour. Unless the fluid flow and its influence on the thermal and/or concentration gradients at the growing dendrite tip may cause the growth of bent dendrites. It is well known that a growing dendrite follows the largest temperature gradient. For instance, future research using an infrared camera could help to clarify and visualize the thermal field around the growing dendrite.

Finally the effect of bent growing dendrites may be used to manipulate the microstructure development during solidification. For example, dendrites could be bent during growth to follow

the curving of a turbine blade or guided growing dendrites of semiconductor on substrates could lead to new technologies.

6.3 Dendrite Growth Velocity V versus Undercooling ΔT

The Fe-B dendrite growth velocities V are measured as a function of undercooling ΔT . Experiments were performed in electromagnetic levitator under different fluid flow conditions: terrestrial 1g-EML and μ g-EML TEMPUS facility during parabolic flight. Additional experiments for Fe-10 at.% B were done in a quartz glass crucible without levitation in a 1g-EML facility. Furthermore melt fluxing experiments (MF) were performed for Fe-1, 5, and 10 at.% B under influence of a high magnetic field up to 6 T.

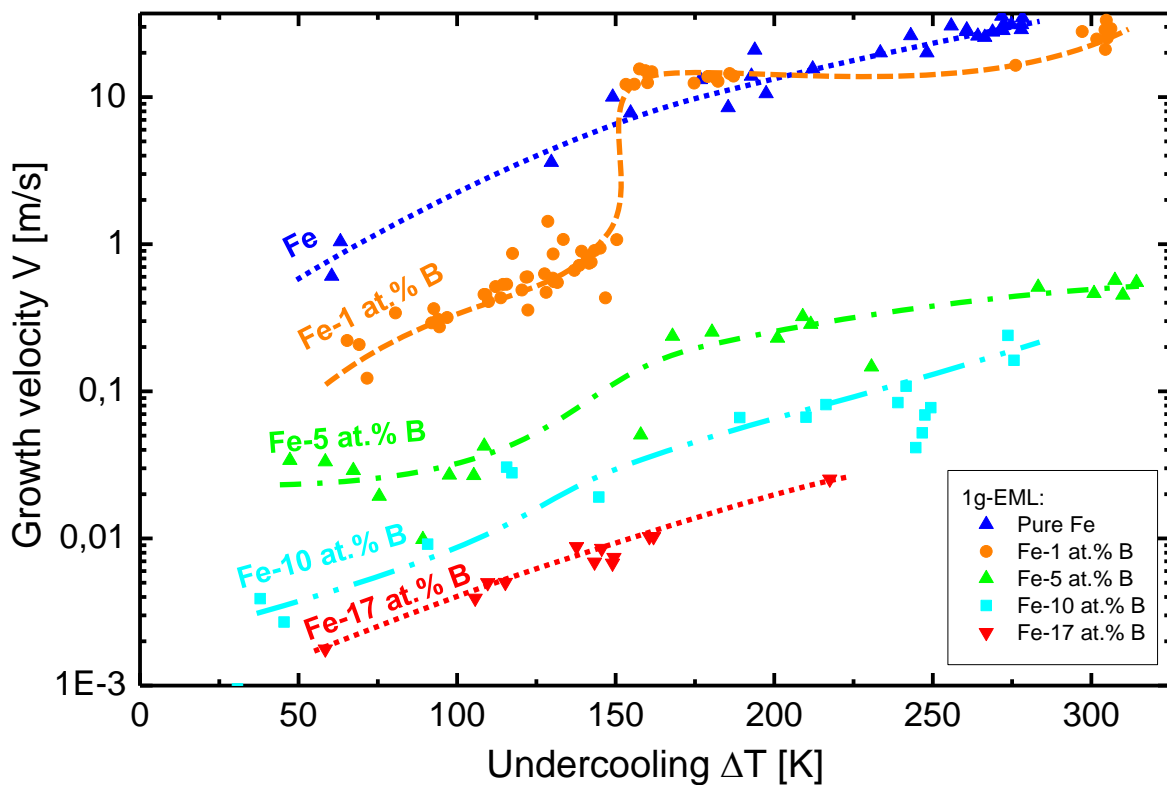


Figure 6-10: Overview of dendritic Fe, Fe-1, 5, 10 and eutectic 17 at.%B 1g-EML results: Half-logarithmic plot of the growth velocity V as a function of undercooling ΔT . The dashed lines are given as a guide for the eye to show main trends.

Figure 6-10 gives an overview about the measured growth velocities for pure Fe, Fe-1, 5 and 10 at.% (including also the eutectic composition Fe-17 at.% B) which are presented and discussed in the following. Dashed lines are given as a guide for the eye. The overview shows clearly the influence of B concentration slowing down the growth velocity. The used sharp interface model for modelling dendritic growth velocities (pure Fe, Fe-1, 5 and 10 at.%) as a function of undercooling is described in chapter 2.

6.3.1 Pure Fe

In order to study the effect of alloying B to Fe it is essential to firstly measure pure Fe for comparison. In addition, these results are compared to Ni and Ni-B alloys. Figure 6-11 shows the results of the dendritic growth velocity for pure Fe and Ni as a function of undercooling including the LKT-model predictions. Fe has a monotonous behaviour with increasing undercooling from some cm/s at low undercoolings up to $50 m/s$ at about $300 K$ undercooling. The videos show a regular, as expected for cubic metals, growth morphology (see section 6.1) with a visible growth front at the sample surface which is the intersection of an octahedral shaped grain. This can be explained by the growth of dendrites along $\langle 100 \rangle$ directions. The tracing of the dendrite tip pathway as the apex of a growing pyramid gives a precise determination of the propagating tip and its velocity inside the spherical sample (see A.1 Video Analysis). According to its equilibrium phase diagram Fe solidifies primarily into bcc phase whereas Ni solidifies into fcc. Furthermore Ni shows a different growth behaviour as Fe at high undercoolings. In the case of Ni, above $\Delta T > 180 K$ ($V > 40 m/s$) the shape at the sample surface changes from an octahedral to an isotropic growth front. BASSLER et al. [101] suggest that the growing dendrites thermally interact with each other. The dendrites become more closely spaced and the thermal fields surrounding each dendrite begin to overlap. However this behaviour cannot be observed in Fe but may occur at undercoolings above $300 K$.

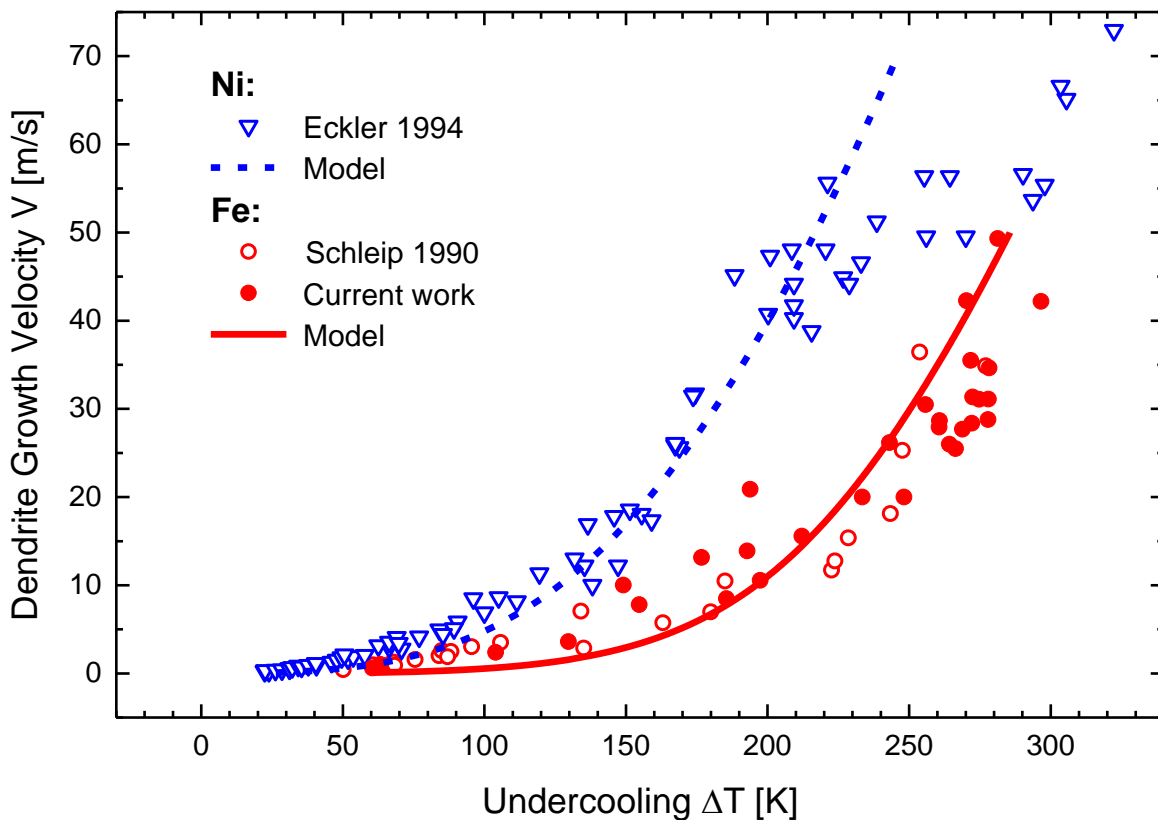


Figure 6-11: Dendrite Growth Velocity V of Fe and Ni as a function of undercooling ΔT . The parameter used for modelling are listed in Table 6-2.

Table 6-2: Thermodynamical constants and material parameters of the pure Fe and Ni used for calculations of dendrite tip radius and dendrite growth velocity.

Parameter	Symbol	Numerical Value		Unit
		Fe	Ni	
Latent heat	ΔH_f	13800	17 150	J/mol
Specific heat of the liquid	$c_{p,L}$	45	41	$J/(mol K)$
Hypercooling limit	ΔT_{hyp} $= \Delta H_f / c_{p,L}$	370	418.29	K
Liquidus temperature	T_L	1811	1728.15	K
Thermal diffusivity	D_T	5×10^{-6}	8.5×10^{-6}	m^2/s
Interfacial energy	γ_{LS}	0.32	0.46	J/m^2
Molar volume	V_{mol}	7.09×10^{-6}	7.08×10^{-6}	m^3/mol
GIBBS-THOMSON parameter	Γ $= \gamma_{LS} T_L V_{mol} \Delta H_f^{-1}$	2.88×10^{-7}	3.28×10^{-7}	$K m$
Growth parameter	V_0	1000	2000	m/s
Interfacial kinetic coefficient	μ_k $= V_0 \Delta H_f / R_G T_L^2$	0.5	1.38	$m/(K s)$
Interface anisotropy parameter	ε_C	0.03	0.022	
Constant parameter	σ_0	45	12	
Stability constant	$\sigma^* = \sigma_0 \cdot \varepsilon_C^{7/4}$	0.001	0.0151	

The model calculations to describe the experimental results were done using the sharp interface model (cf. chapter 2.1). The used physical and material parameters for modelling are listed in Table 6-2. In the case of a pure metals the total undercooling is given by $\Delta T = \Delta T_T + \Delta T_R + \Delta T_K$. The curvature undercooling ΔT_R and kinetic undercooling ΔT_K are small in comparison to the thermal undercooling ΔT_T . Consequently the dendritic growth is dominated by the thermal gradient ahead of the solidification front and the heat transport into the liquid. This is the reason why pure metal dendrites are often called *thermal* dendrites.

The latent heat of fusion ΔH_f for Fe is 13 800 J/mol according to Ref. [13]. This value is also used for Fe-1, 5 and 10 at.% B alloys where a solid solution of Fe primarily crystallizes. The interface mobility/kinetic coefficient μ_k is chosen as a “best fit” parameter according to the velocity results in Figure 6-11. In the case of collision limited growth (see chapter 1.5.2), the prefactor of the kinetic undercooling term will be in the order of the speed of sound. The speed of sound in liquid Fe is about 3820 m/s according to Ref. [102] and for Ni about 4250 m/s [103]. Here the value for V_0 is chosen to be 1000 m/s for Fe and 2000 m/s for Ni. The kinetic growth coefficient is calculated as $\mu_k = V_0 \Delta H_f / R_G T_L^2$ to 0.5 $m \cdot s^{-1} \cdot K^{-1}$ for Fe and 1.38 $m \cdot s^{-1} \cdot K^{-1}$ for Ni. Furthermore the anisotropy of the interfacial energy ε_C to describe the experimental results is chosen to be 0.03 for Fe and 0.022 for Ni. The microscopic solvability theory predicts the selection of the operating dendrite tip radius R and the growth velocity V depending on the

magnitude of the anisotropy of the interfacial energy ε_c in terms of a dimensionless stability parameter $\sigma^* = \sigma_0 \cdot \varepsilon_c^{7/4}$. As a best fit parameter σ^* is determined to be 0.001 for Fe and 0.0151 for Ni. The theoretical operating dendrite tip radius R as a function of undercooling is plotted in Figure 6-12 for Fe and Ni. Obviously a thinner operating dendrite tip radius for Ni is consistent with the faster growth of Ni compared to Fe. A thin dendrite grows faster as a thick one. Pure Fe crystallises in body-centered cubic (bcc) crystal structure whereas pure Ni crystallises in face-centered cubic (fcc) crystal structure. An Fe atom in a bcc crystal has 8 and a Ni atom in a fcc crystal has 12 nearest neighbours. HOLLAND-MORITZ et al. investigated the short-range order and coordination number Z in undercooled Fe and Ni liquids by neutron diffraction experiments [104]. Atoms joining the solid from the liquid have in the case of Ni (fcc) a higher possibility to attach which can explain the faster dendritic growth of Ni. The crystallization kinetics in fcc and bcc metals were investigated with MD simulations by ASHKENAZY and AVERBACK [105]. Their results show two different temperature regimes. In MD simulations for hard spheres it could be shown that the reported velocity difference in bcc and fcc crystallization is related to kinetic factors and not to an anisotropy in the free energy [2, 106].

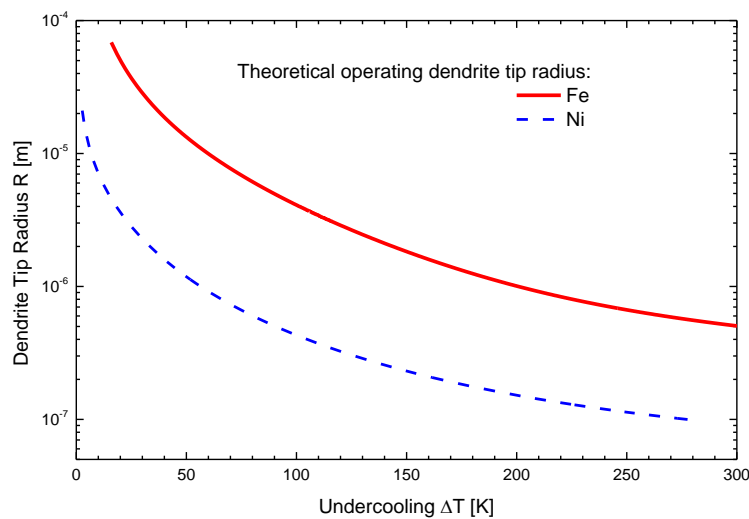


Figure 6-12: Half-logarithmic plot of the theoretical operating dendrite tip Radius R as a function of undercooling ΔT for Ni (dashed blue) and Fe (solid red).

The total undercooling ΔT for Fe and Ni split into different undercooling contributions which are shown in Figure 6-13. The thermal undercooling ΔT_T is dominating the growth behaviour (*thermal dendrite*) while the kinetic undercooling ΔT_K increases with rising undercooling. The contribution of the curvature undercooling ΔT_R due to the GIBBS-THOMSON effect is smaller than 5 K over the entire undercooling range accessible by the experiments and therefore neglectable small. However the difference between Fe and Ni is significant in the case of the curvature undercooling ΔT_R .

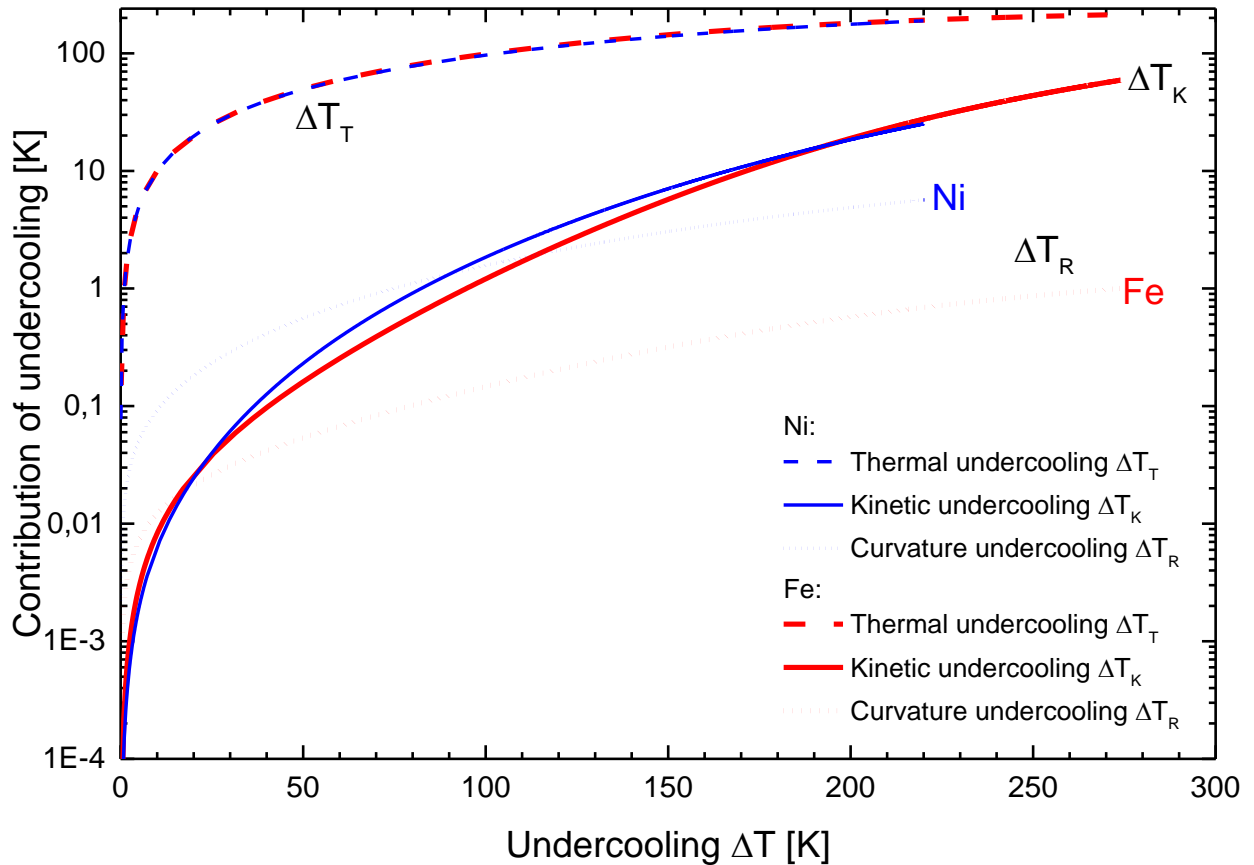


Figure 6-13: Contributions of undercooling as a function of the total undercooling ΔT for Fe (red) and Ni (blue): Thermal undercooling ΔT_T (dashed), kinetic undercooling ΔT_K (solid) and curvature undercooling ΔT_R (dotted).

The theoretical influence of convection on the growth velocity is plotted in a half-logarithmic plot in Figure 6-14 for different fluid flow velocities $U_0 = 0.05 \text{ m/s}$ and 0.3 m/s which correspond to the theoretical values in $\mu\text{g-EML}$ and 1g-EML [9]. In a pure metal the fluid flow acts on the thermal gradient field ahead of the growing dendrite as described in chapter 2.2. Consequently with increasing fluid flow the temperature gradient gets steeper and the dendrite grows faster while the heat transport is enhanced. The thermal undercooling contribution ΔT_T is plotted in Figure 6-15 as a function of the total undercooling ΔT and growth velocity V for different fluid flow conditions. In the case of an alloy the influence of convection on the concentration field ahead of the growing dendrite is much stronger (see 6.3.2, 6.3.3, and 6.3.4). This is reasonable because the thermal diffusion (10^{-5} m/s) is much larger than the mass diffusion (10^{-9} m/s).

It should be mentioned that fluid-flow also acts on phase selection and nucleation in undercooled liquid metals as shown by HYERS et al. [107]. However this fact is not included in the sharp interface model which was used to model the growth velocities as a function of undercooling.

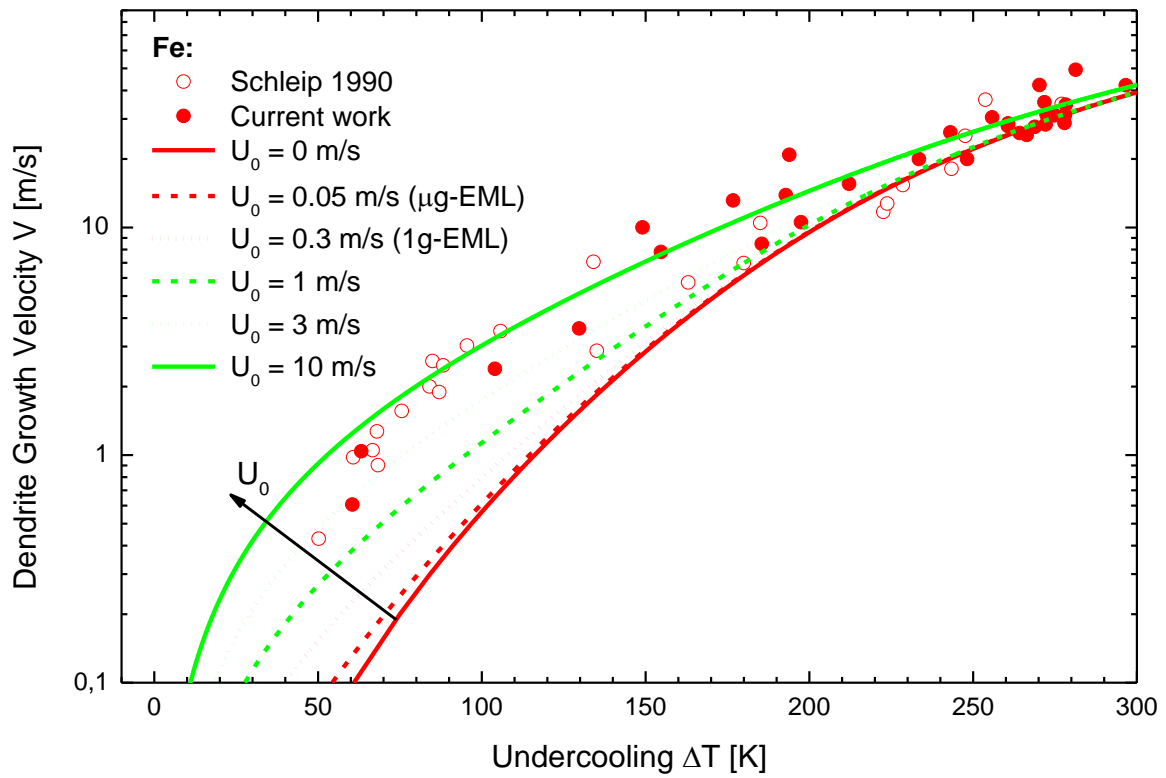


Figure 6-14: Half-logarithmic plot of Fe dendrite growth velocity V as a function of undercooling ΔT for different fluid flow U_0 .

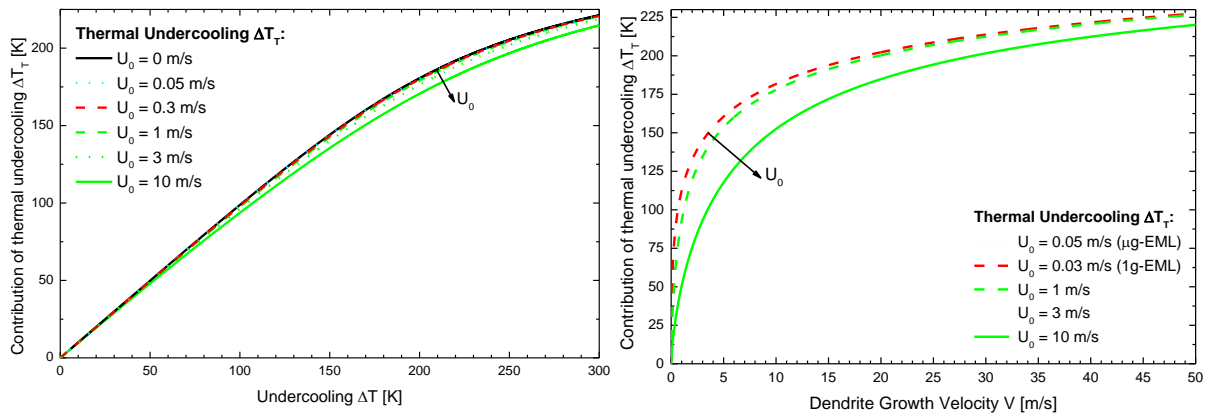


Figure 6-15: Thermal undercooling ΔT_7 for Fe plotted as a function of the total undercooling ΔT and the dendrite growth velocity V for different fluid flow U_0 .

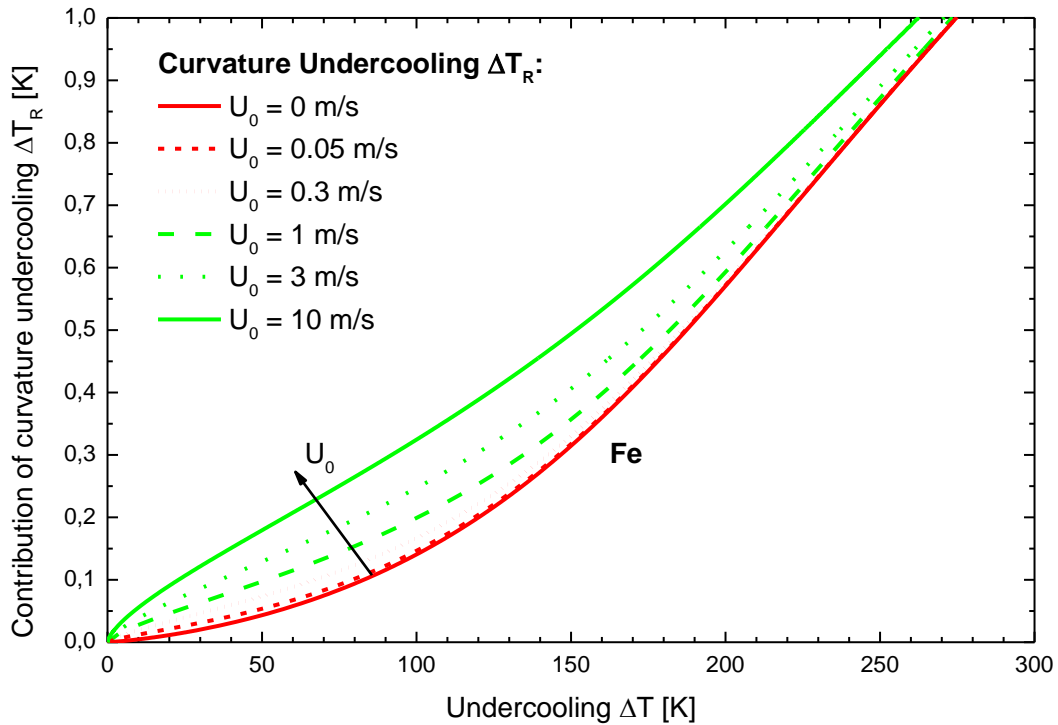


Figure 6-16: Contribution of curvature undercooling ΔT_R to the total undercooling ΔT plotted for different fluid flow U_0 .

The fluid flow velocity of $U_0 = 10$ m/s to describe the 1g-EML experimental results is physical unrealistic. The used two-dimensional model underestimates the heat and mass transport by convection. Recently, GAO et al. investigated dendrite growth velocities in an undercooled melt of pure Ni under static magnetic field (up to 6 T) [108]. The used three-dimensional model by ALEXANDROV and GALENKO [109] can describe the growth velocity results as a function of undercooling. This demonstrate a realistic description of dendritic growth kinetics of pure substances with convection due to stronger heat and mass transport as in two-dimensional models.

6.3.2 Fe-1 at.% B

Figure 6-17 shows the results of dendrite growth velocity V as a function of undercooling ΔT for Fe 1g-EML and Fe-1 at.% B 1g-EML and μg -EML. By alloying 1 at.% B to Fe the growth velocity for small undercoolings drops down essentially to the range of velocities of cm/s . For small undercoolings the dendrite growth velocities of the dilute Fe-B alloy stay much smaller than those of pure Fe. At an undercooling of about 160 K the growth velocity of Fe-1 at.% B shows a sharp increase to about 14 m/s. This effect is called solute trapping which is described in chapter 1.5.3. Table 6-3 lists the material parameter used for modelling of dendrite growth. A similar growth behaviour can be observed in the Ni-B system. The transition of diffusion limited growth of dendrites (solutal growth) to thermally controlled solidification was proven by Eckler in 1992 [110]. Figure 6-18 shows their results for Ni-B. Solute trapping for Ni-1 at.% B occurs at a higher undercooling ($> 200 \text{ K}$) compared to Fe-1 at.% B. In the case of dilute Fe-1 at.% B the plot can be divided into 3 regimes:

- Solutal growth ($80 \text{ K} < \Delta T < 160 \text{ K}$),
- Solutal and thermal growth (plateau $\Delta T > 160 \text{ K}$),
- Thermal growth, almost partition less solidification ($\Delta T > 280 \text{ K}$).

The first regime is the diffusion limited ($80 \text{ K} < \Delta T < 160 \text{ K}$) which is described well by the model. Second regime is the transition from diffusion limited to thermally controlled ($160 \text{ K} < \Delta T < 190 \text{ K}$) with the active development of solute trapping. Third regime is the totally thermal controlled part with a high scattering in data.

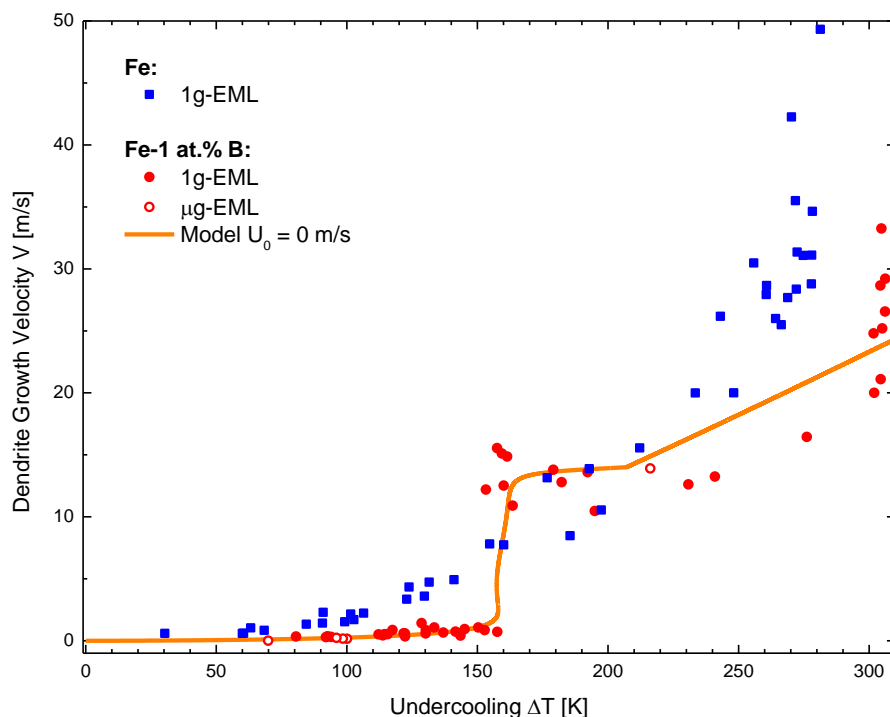
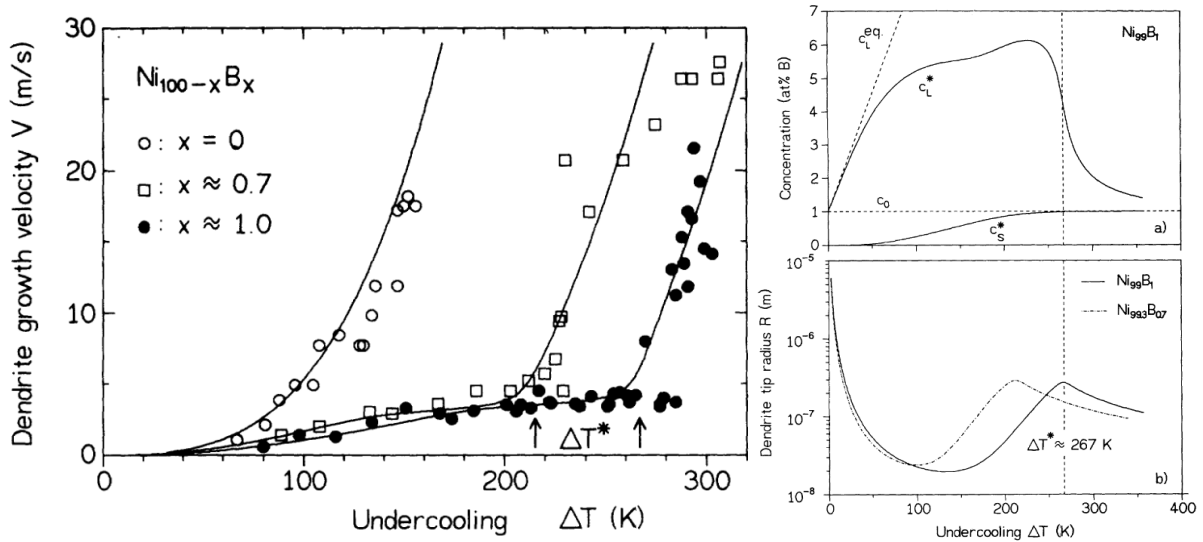


Figure 6-17: Dendrite growth velocity as a function of undercooling for Fe and Fe-1 at.% B.

Table 6-3: Thermodynamical constants and material parameters of the Fe-1 at.% B composition used for calculations of dendrite tip radius and dendrite growth velocity.

Parameter	Symbol	Numerical value	Unit
Concentration of Boron	C_0	10	at. %
Liquidus temperature	T_m	1793	K
Latent heat	ΔH_f	13800	J/mol
Specific heat of the liquid	$c_{p,L}$	45	J/(mol K)
Hypercooling limit	$\Delta T_{hyp} = \Delta H_f / c_{p,L}$	306.7	K
Liquidus slope	m_e	-17.14	K/at. %
Partition coefficient	k_e	0.001	
Diffusion coefficient	D_C	5×10^{-9}	m^2/s
Thermal diffusivity	D_T	5×10^{-6}	m^2/s
Interfacial energy	γ_{LS}	0.31	J/m ²
Molar volume	V_{mol}	7.09×10^{-6}	m ³ /mol
GIBBS-THOMSON coefficient	$\Gamma = \gamma_{LS} T_L V_{mol} \Delta H_f^{-1}$	2.85×10^{-7}	K m
Diffusion speed in bulk liquid	V_D	14	m/s
Interface diffusion speed	V_{DI}	2.5	m/s
Interfacial kinetic coefficient	$\mu_k = V_0 \Delta H_f / R_G T_L^2$	0.118	m/(K s)
Interface anisotropy parameter	ϵ_C	0.03	
Stability constant parameter	σ_0	45	
Stability constant	$\sigma^* = \sigma_0 \cdot \epsilon_C^{7/4}$	0.097	
First asymptotic parameter	a_1	0.3	
Second asymptotic parameter	a_2	0.02	

**Figure 6-18:** Results by Eckler et al. taken from Ref. [110]. Dendrite growth velocities V for Ni, Ni-0.7, and Ni-1 at.% B as a function of undercooling ΔT (left graph). The growth velocities show a sharply rise at a critical undercooling $\Delta T^* = 214$ K for Ni-0.7 at.% B and $\Delta T^* = 267$ K for Ni-1 at.% B. This effect of solute trapping can be seen in the concentration (upper right graph) and dendrite tip radius (lower right graph).

The diffusion velocity V_D of B in liquid Fe can be estimated to be around 14 m/s by the experimental data where solute trapping occurs, whereas the diffusion velocity at the interface V_{DI} is about 2.5 m/s . The velocity dependence of the partition coefficient $k(V)$ is plotted in Figure 6-19. For $V = 0 \text{ m/s}$ the partition coefficient has the value of the equilibrium partition coefficient $k_E = 0.001$. With rising solidification velocity k increases until reaching the diffusion velocity V_D where solute trapping occurs and k remains 1 for $V \geq V_D$. This is consistent with the jump of one magnitude in growth velocity from cm/s to the diffusion velocity of m/s at an undercooling $\Delta T \approx 160 \text{ K}$.

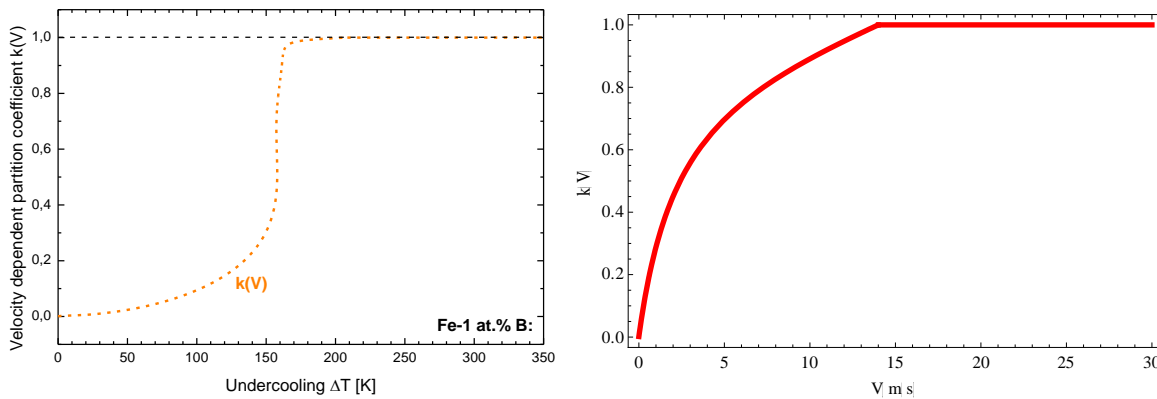


Figure 6-19: Velocity dependence of the partitioning coefficient $k(V)$ plotted as a function of undercooling (orange dashed) and growth velocity (red solid). Starting at $\Delta T = 0 \text{ K}$ corresponding to a growth velocity $V = 0 \text{ m/s}$ with the value of the equilibrium partition coefficient $k_E = 0.001$ and rising until reaching the diffusion velocity $V_D = 14 \text{ m/s}$ at an undercooling $\Delta T = 160 \text{ K}$ where solute trapping occurs and k becomes 1 for $V \geq V_D$.

The crystal growth velocity is the decisive parameter governing the trapping of solute in the solvent material. The concentrations at the dendrite tip in the liquid phase c_L^* and in the solid phase c_S^* is given by:

$$c_L^* = \frac{c_0}{1 - [1 - k(V)] I v(P_C)},$$

$$c_S^* = k(V) c_L^*.$$

Figure 6-20 shows the calculated distribution of c_L^* and c_S^* as a function of undercooling. For small undercoolings the B concentration c_L^* grows rapidly with rising undercooling due to solute rejection into the liquid. This leads to a pile up of B concentration ahead of the growing dendrite tip. The growing crystal solves B according to its equilibrium partition coefficient k_E which limits the growth velocity due to the finite diffusion velocity of B atoms in the liquid Fe. This process dominates and slows down the growth velocity V to some cm/s until solute trapping increases the solute concentration c_S^* in the crystal. The sharp increase of the dendrite growth velocity at an undercooling of about 160 K implies solute trapping. As a consequence, the concentration c_L^* in the liquid phase approaches the nominal concentration of the composition (1 at. % B) while the concentration c_S^* of the crystal increases to the nominal composition.

Obviously, B is trapped beyond its equilibrium partition coefficient leading to a supersaturated solid solution. At very large undercoolings solidification takes place partitionless.

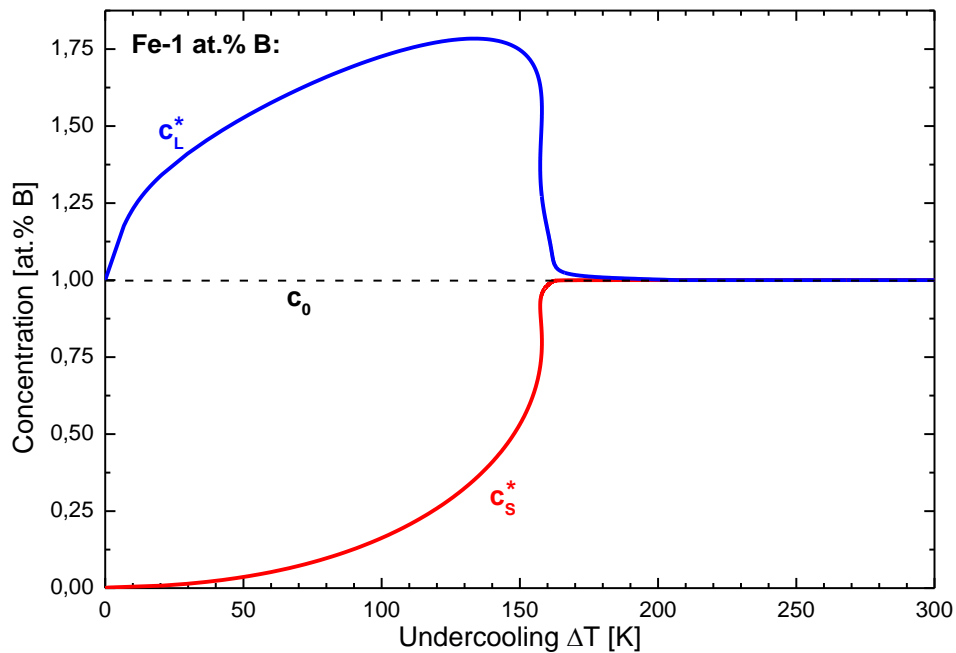


Figure 6-20: Calculated concentrations c_L^* and c_S^* at the dendrite tip as a function of undercooling.

The total undercooling ΔT splits into different undercooling terms. The constitutional undercooling ΔT_C and the curvature undercooling ΔT_R dominate the first regime ($\Delta T < 160$ K) while the thermal undercooling ΔT_T and the kinetic undercooling ΔT_K dominate the regime for large undercoolings. The critical undercooling $\Delta T^* = 160$ K is also pronounced in the dendrite tip radius which is plotted in Figure 6-22.

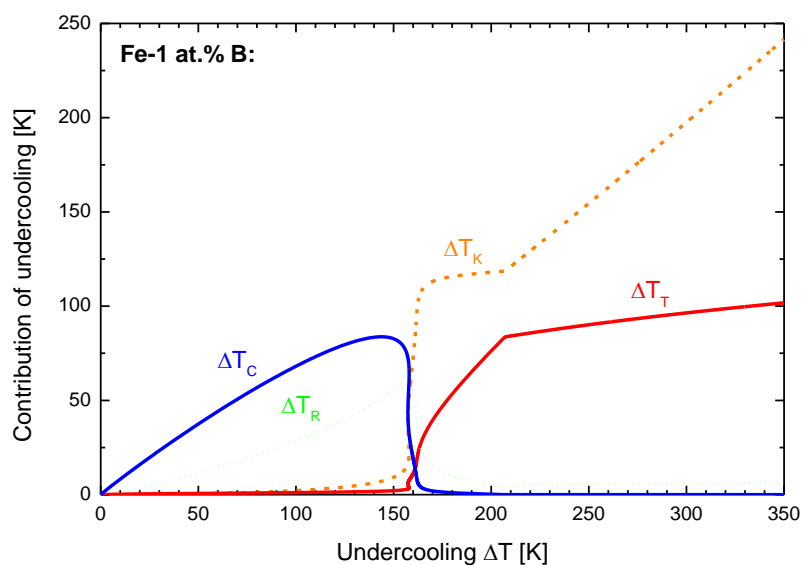


Figure 6-21: Contributions of undercooling as a function of the total undercooling ΔT for Fe-1 at.% B: Constitutional undercooling ΔT_C (blue solid), thermal undercooling ΔT_T (red solid), kinetic undercooling ΔT_K (orange dashed) and curvature undercooling ΔT_R (green dotted).

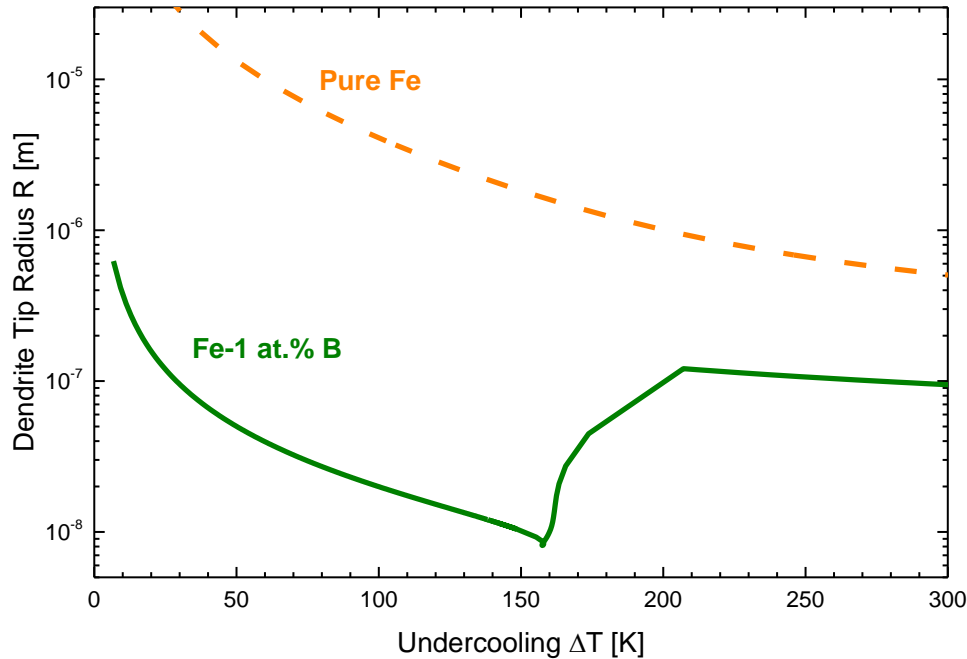


Figure 6-22: Dendrite Tip Radius R as a function of undercooling ΔT .

The growth velocity at about 160 K where the solute trapping phenomenon occurs another interesting effect becomes apparent. A very slim growing concentrational dendrite of about $10^{-8}m$ radius can grow faster as a thermal dendrite of about $10^{-6}m$. The dendrite growth velocity of Fe-1 at.% B seems to be even faster than that of pure Fe. This effect has been observed by ECKLER et al. for Ni-C [111]. They reported anomalously high velocities in the Ni-0.6 at.% C alloy which showed enhanced dendrite growth velocities in comparison with nominal pure Ni.

At very large undercooling the growth velocity values of Fe-1 at.% cannot be described by the model. Above an undercooling of 300 K the velocity rises drastically. This effect and the scatter of data points could be explained by a shift of primary bcc to primary fcc phase. This is the same idea as the assumption to explain the difference between Fe and Ni which was already discussed in section 6.3.1. HOLLAND-MORITZ et al. investigated the short-range order in undercooled Fe and Ni liquids by neutron diffraction experiments [104]. In brief, for bcc the coordination number is 8 in contrast to 12 in the case of fcc crystal structure. Therefore the attachment kinetics is faster for 12 instead of 8 nearest neighbours.

The small value of the anisotropy strength parameter $\varepsilon_c = 0.03$ is an indication to explain bent dendrite growth which is described in section 6.2. The growing dendrite tip is “sensible” against concentrational and thermal fluctuations induced by fluid flow. Not only the growth direction is affected by fluid flow but also the dendrite growth velocity. Therefore the growth velocities are measured under different fluid flow conditions (μg -EML and melt fluxing with a static magnetic field). Figure 6-23 shows the dendrite growth velocity as a function of undercooling for 1g-EML

and μg -EML. In the case of μg -EML the growth velocities at low undercoolings are as expected smaller than in 1g-EML. In general the growth velocity is increased by fluid flow. Consequently, smaller fluid flow velocities lead to slower growth velocities. This influence is strongest for small undercoolings compared with large undercoolings.

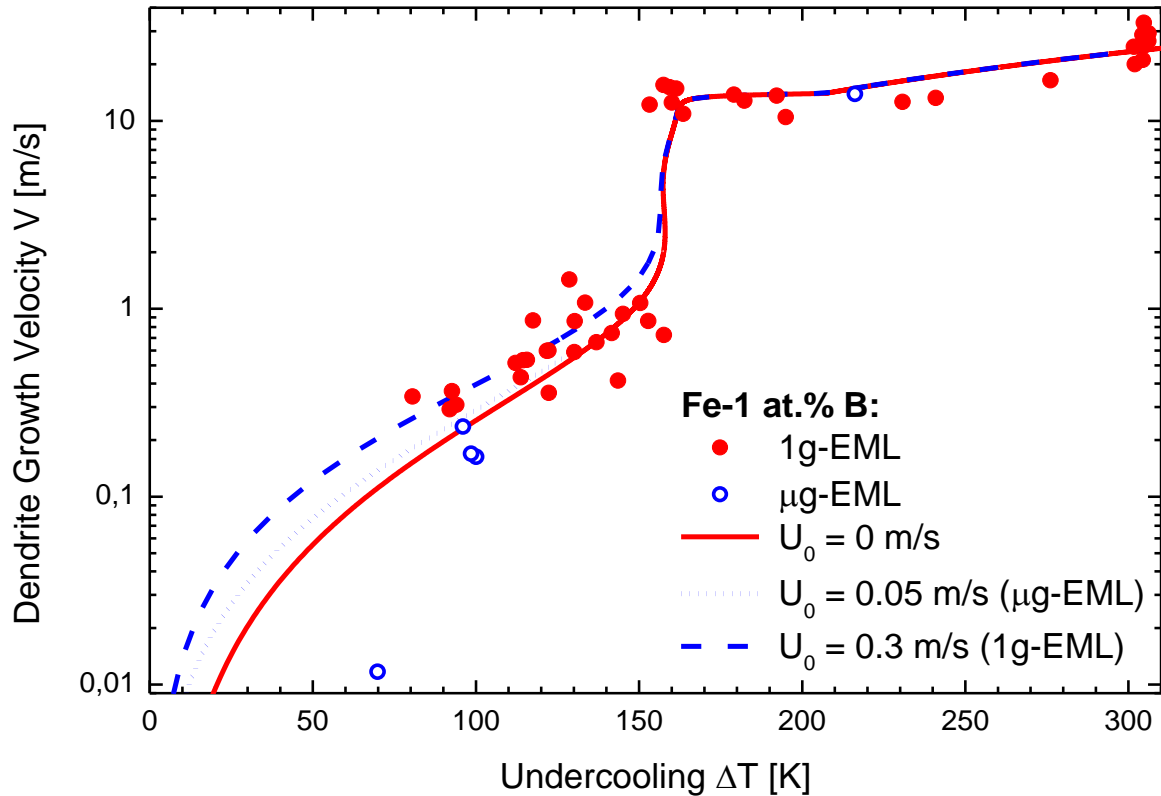


Figure 6-23: Half-logarithmic plot of the dendrite growth velocities as a function of undercooling for Fe-1 at.% B in 1g-EML and μg -EML. The influence of convection is strongest at low undercooling where the fluid flow velocity inside the melt is in the same order of magnitude as the growth velocity itself.

6.3.2.1 Microstructure Analysis of Fe-1 at.% B samples

Microstructure of samples processed during parabolic flight are analysed by means of SEM. One sample is investigated with respect to its microstructure which solidified at slow undercooling $\Delta T = 70$ K under microgravity conditions and another sample which solidified at large undercooling $\Delta T = 270$ K (with solute trapping). Samples processed in μg -EML show typically a more detailed undisturbed microstructure due to less fluid flow conditions during solidification.

To give a confirmation of solute trapping the interdendritic fraction is estimated and analysed. Therefore a sample solidified with and without solute trapping is investigated. A homogeneous distribution of primarily Fe solidifies dendritic. The remaining liquid in the space between network of dendrite branches after primary solidification leads to coarsening of the actual dendrites unless the remaining liquid solidifies eutectic. For high undercoolings, where solute trapping occurs the fraction of interdendritic B content should be less compared to low

undercoolings with no solute trapping. The reason is that B is “trapped” already in the dendritic structure which means less B remains for the interdendritic eutectic solidification.

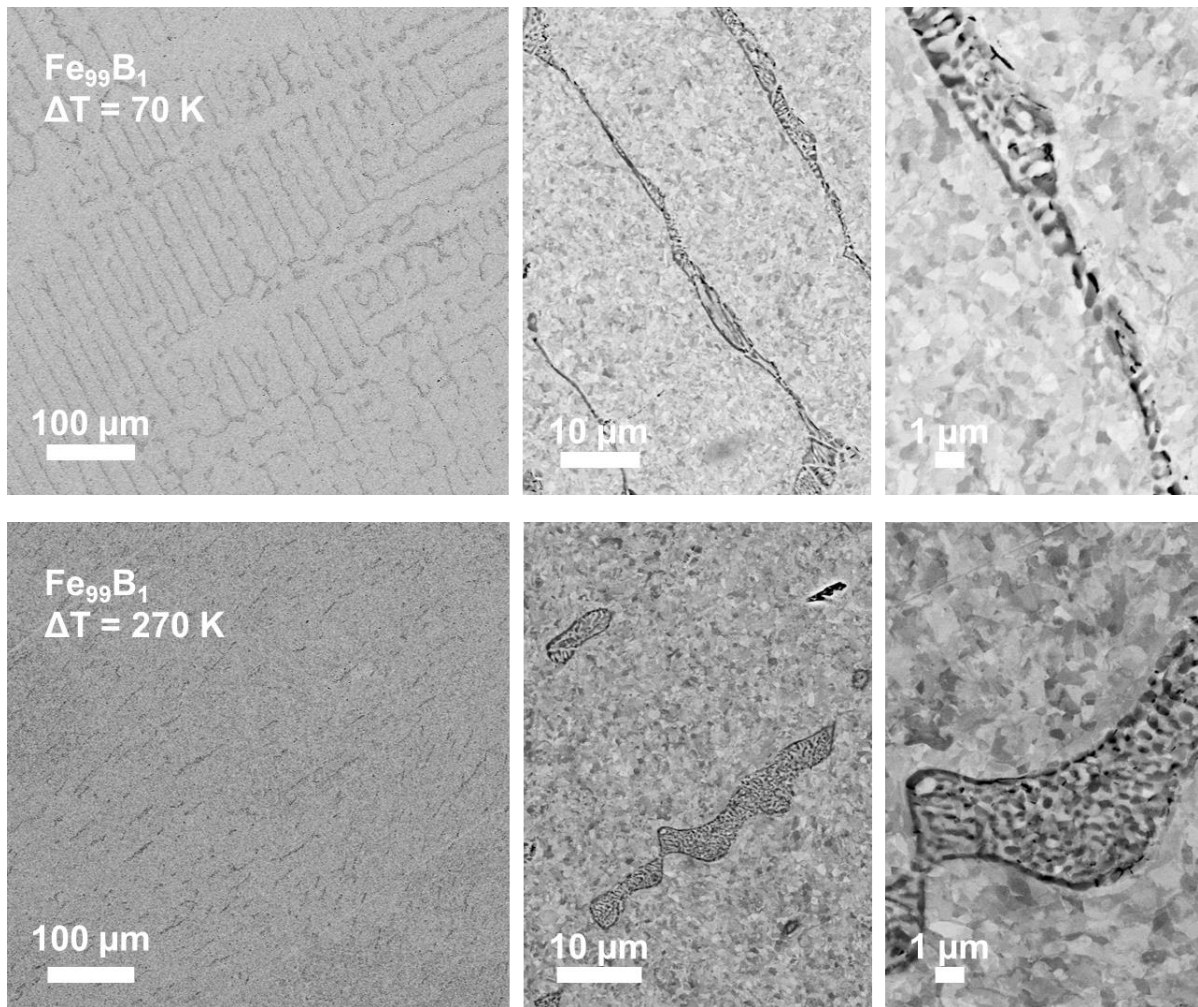


Figure 6-24: Interdendritic fraction of parabolic flight samples... Low undercooling ($\Delta T = 70 \text{ K}$) and high undercooling ($\Delta T = 270 \text{ K}$) where solute trapping occurs.

6.3.3 Fe-5 at.% B

Fe-5 at.% B shows in the case of 1g-EML experiments a very strong bent growing dendrite behaviour (zigzagging) as mentioned in section 6.1. Therefore the measured growth velocities have a large error/scatter and should be interpreted with care. Figure 6-25 shows the experimental results (1g-EML, μ g-EML and MF) for dendrite growth velocities as a function of undercooling. Table 6-4 lists the material parameter used for modelling of dendrite growth velocities. The model describes the data in good agreement also concerning different fluid flow velocities U_0 . The used parameters for modelling Fe-5 at.% B growth velocities include the desired values for the solid-liquid interface free energy $\gamma = 0.31 \text{ Jm}^{-2}$, its anisotropy $\varepsilon = 0.01$ which is weaker than the found value for Fe-1 at.% B, and the kinetic growth coefficient $\mu_k = 0.04 \text{ mK}^{-1}\text{s}^{-1}$ which is also smaller compared to Fe-1 at.% B. However, the appearance of solute trapping cannot be proofed in the case of Fe-5 at.% B as well as the competition between primary bcc and fcc structure crystallization. The contributions of undercooling are shown in Figure 6-26. The solute concentration at the dendrite tip is plotted in Figure 6-28. Figure 6-27 shows a half-logarithmic plot of the theoretical operating dendrite tip radius R as a function of undercooling.

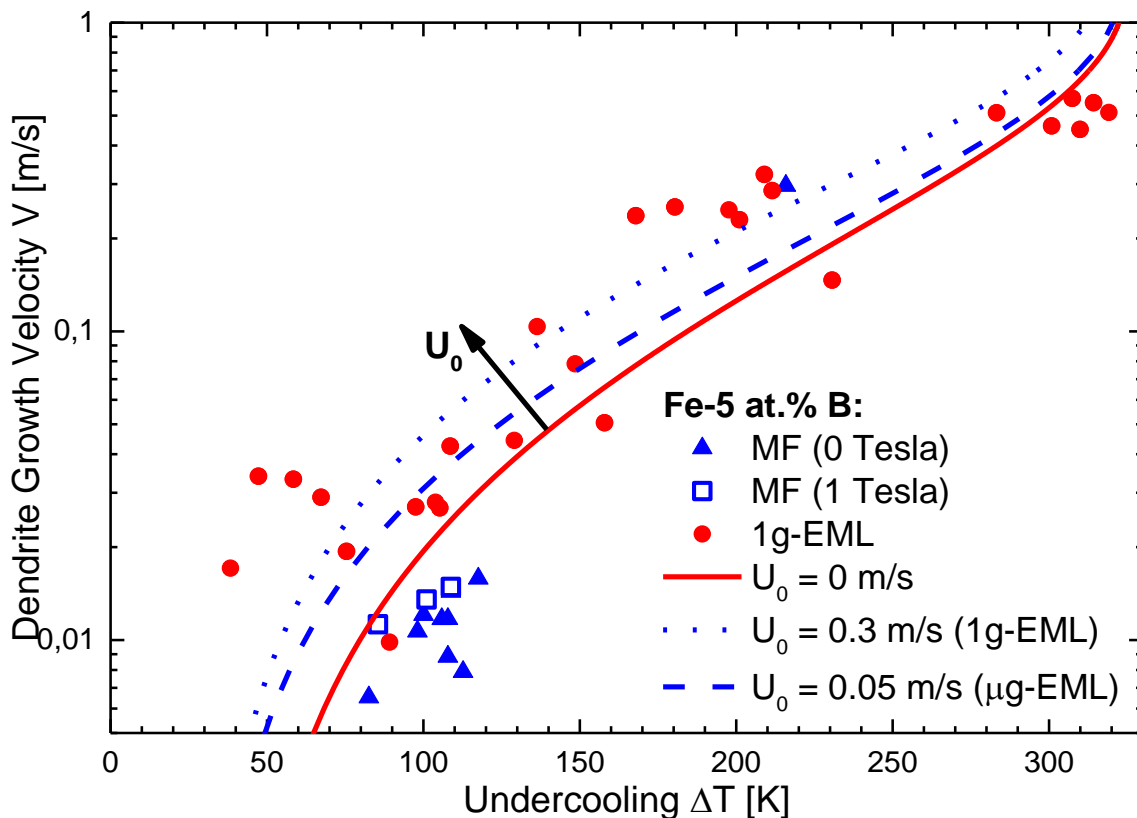
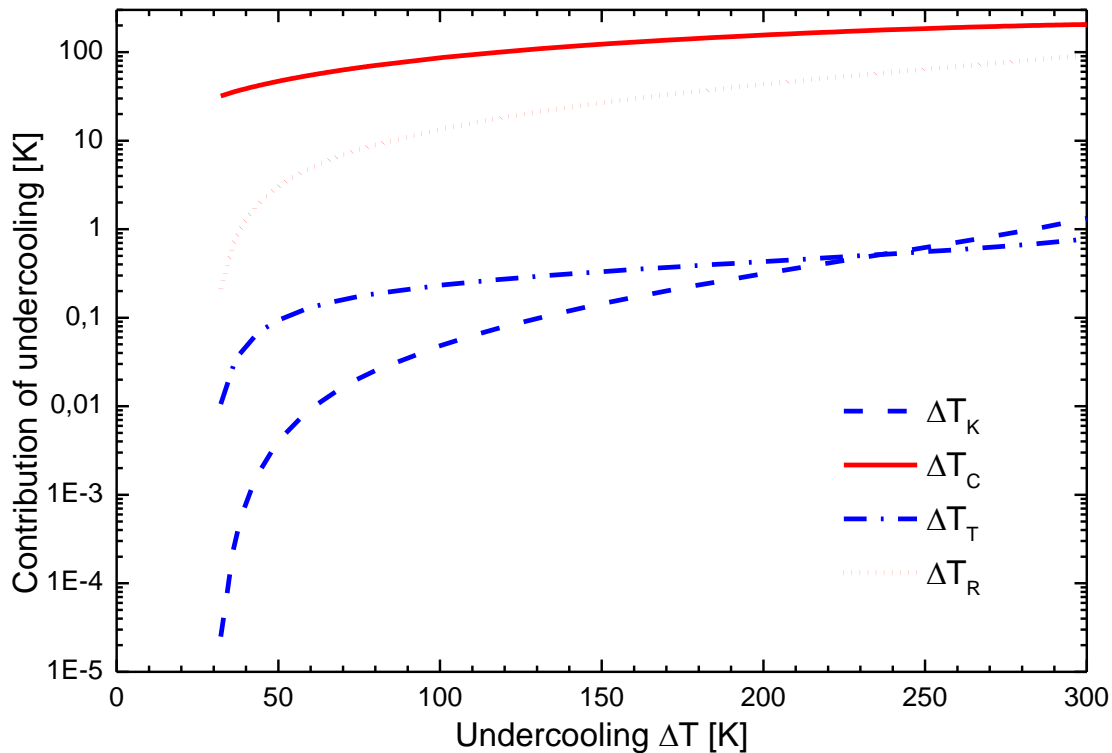


Figure 6-25: Dendrite growth velocity V as a function of undercooling ΔT for Fe-5 at.% B.

Table 6-4: Thermodynamical constants and material parameters of the Fe-5 at.% B composition used for calculations of dendrite tip radius R , dendrite growth velocity V , undercooling contributions.

Parameter	Symbol	Numerical value	Unit	Ref.
Concentration of Boron	C_0	5	at. %	
Liquidus temperature	T_m	1723	K	
Latent heat	ΔH_f	13800	J/mol	
Specific heat of the liquid	$c_{p,L}$	45	J/(mol K)	
Hypercooling limit	$\Delta T_{hyp} = \Delta H_f / c_{p,L}$	306.7	K	
Liquidus slope	m_e	-16.56	K/at. %	
Partition coefficient	k_e	0.001		
Diffusion coefficient	D_C	1×10^{-9}	m^2/s	
Thermal diffusivity	D_T	4.5×10^{-6}	m^2/s	
Interfacial energy	γ_{LS}	0.31	J/m ²	
Molar volume	V_{mol}	7.09×10^{-6}	m ³ /mol	
GIBBS-THOMSON coefficient	$\Gamma = \gamma_{LS} T_L V_{mol} \Delta H_f^{-1}$	2.7×10^{-7}	K m	
Growth parameter	V_0	-	m/s	
Diffusion speed in bulk liquid	V_D	14	m/s	
Interface diffusion speed	V_{DI}	2.5	m/s	
Interfacial kinetic coefficient	$\mu_k = V_0 \Delta H_f / R_G T_L^2$	0.04	m/(K s)	
Interface anisotropy parameter	ε_C	0.01		
Stability constant parameter	σ_0	5		
Stability constant	$\sigma^* = \sigma_0 \cdot \varepsilon_C^{7/4}$	0.0086		
First asymptotic parameter	a_1	0.3		
Second asymptotic parameter	a_2	0.01		

**Figure 6-26:** Contributions of undercooling as a function of the total undercooling ΔT for Fe-5 at.% B: Constitutional undercooling ΔT_C , kinetic undercooling ΔT_K (blue dashed), thermal undercooling ΔT_T (blue dash-dotted), and curvature undercooling ΔT_R (red dotted)

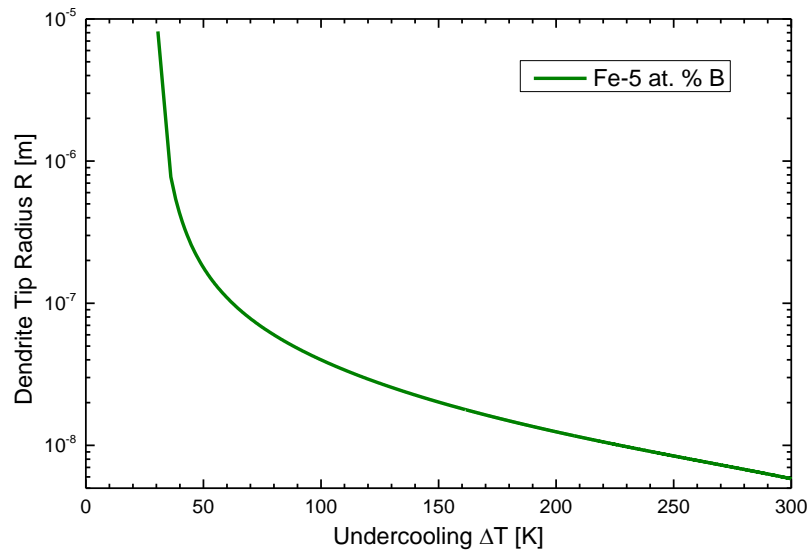


Figure 6-27: Half-logarithmic plot of the theoretical operating dendrite tip Radius R as a function of undercooling ΔT for Fe-5 at.% B.

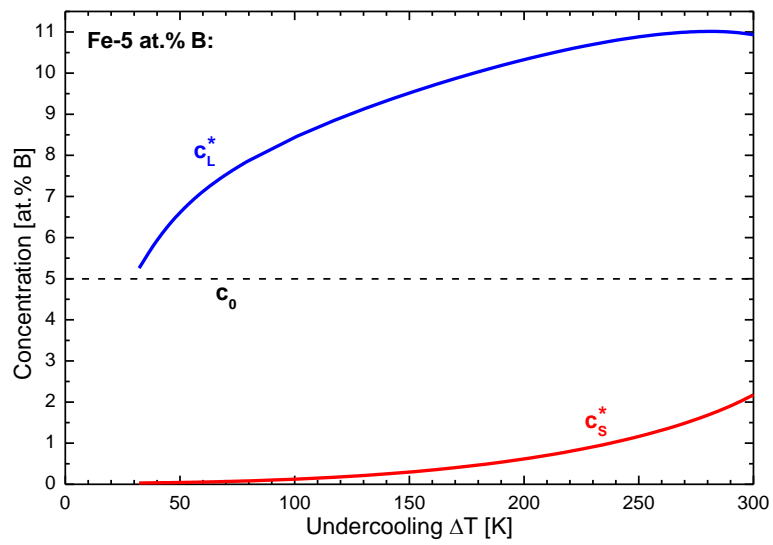


Figure 6-28: Concentration of B at the growing dendrite tip in the liquid c_L^* (blue) and the solid c_S^* (red).

6.3.4 Fe-10 at.% B

Fe-10 at.% B experiments were performed in 1g-EML, μg -EML TEMPUS parabolic flight, and melt fluxing experiments in a static magnetic field (1 and 2 T).

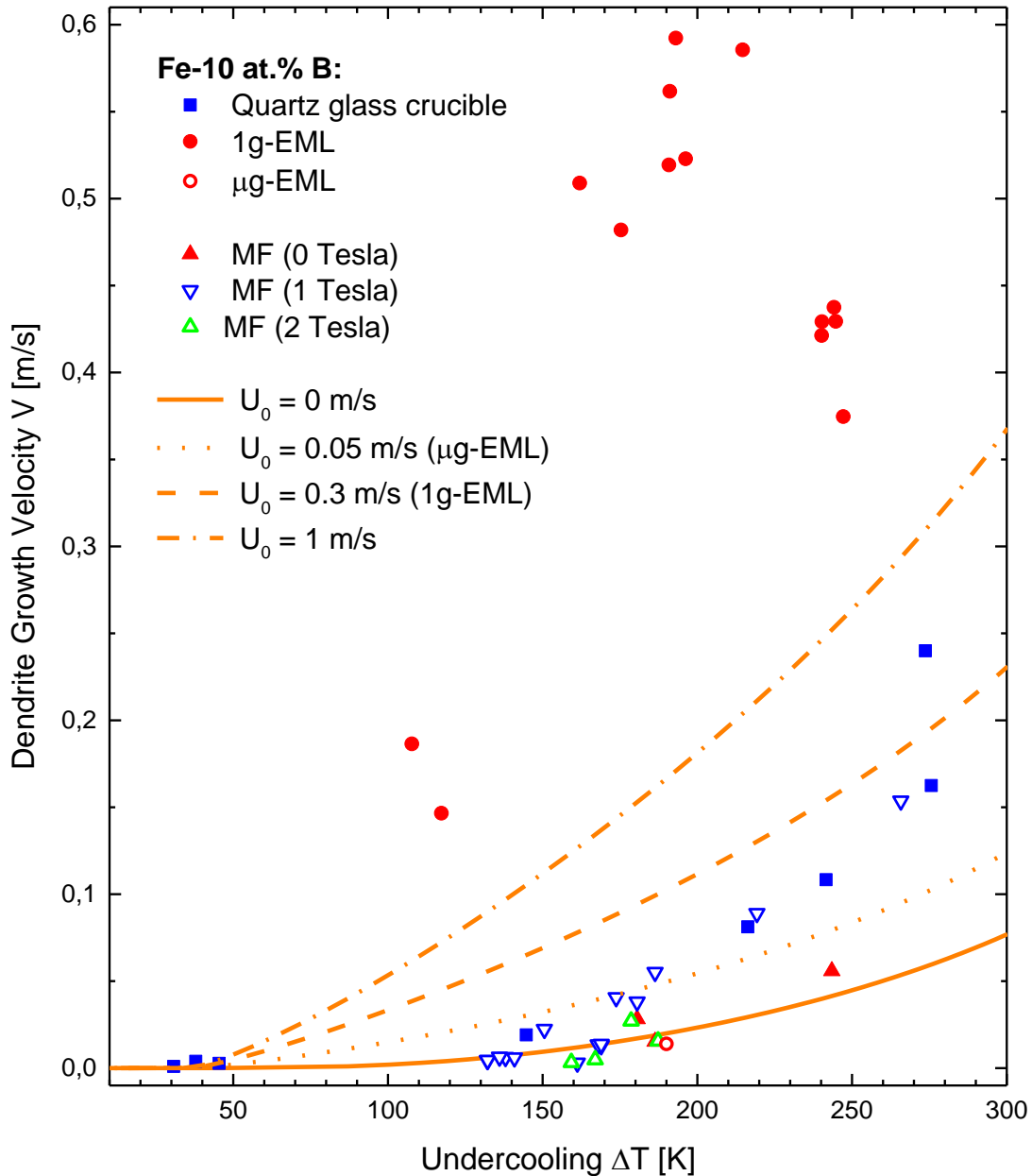


Figure 6-29: Dendrite growth velocity V as a function of undercooling ΔT for Fe-10 at.% B.

The measured growth velocities for Fe-10 at.% B have a large error/scatter and should be interpreted with care. This can be explained by influence of fluid flow in 1g-EML, rotation and oscillation of the samples. The growth velocities might overestimated because of the curved growth (U-Turn). Figure 6-29 shows the experimental results (1g-EML, μg -EML and MF) for dendrite growth velocities as a function of undercooling. Table 6-5 lists the material parameter used for modelling of dendrite growth velocities. The model describes the experimental data qualitatively with different fluid flow velocities U_0 . The used parameters for modelling Fe-10

at.B growth velocities include the desired values for the solid-liquid interface free energy $\gamma = 0.31 \text{ Jm}^{-2}$, its anisotropy $\varepsilon = 0.01$ which is the same for Fe-5 at.% B, and the kinetic growth coefficient $\mu_k = 0.006 \text{ mK}^{-1}\text{s}^{-1}$ which is smaller compared to Fe-1 and 5 at.% B. The contributions of undercooling are shown in Figure 6-30. The solute concentration at the dendrite tip is plotted in Figure 6-31. Figure 6-32 shows a half-logarithmic plot of the theoretical operating dendrite tip radius R as a function of undercooling.

The results for MF with 2 Tesla are as expected similar to μg -EML. The influence of convection is strongest for 1g-EML compared to MF and μg .

Table 6-5: Thermodynamical constants and material parameters of the Fe-10 at.% B composition used for calculations of dendrite tip radius R , dendrite growth velocity V , undercooling contributions.

Parameter	Symbol	Numerical value	Unit	Ref.
Concentration of Boron	C_0	10	at. %	
Liquidus temperature	T_m	1590	K	
Latent heat	ΔH_f	13800	J/mol	
Specific heat of the liquid	$c_{p,L}$	45	J/(mol K)	
Hypercooling limit	$\Delta T_{hyp} = \Delta H_f/c_{p,L}$	306.7	K	
Liquidus slope	m_e	-15.22	K/at. %	
Partition coefficient	k_e	0.001		
Diffusion coefficient	D_C	1.2×10^{-9}	m^2/s	
Thermal diffusivity	D_T	5×10^{-6}	m^2/s	
Interfacial energy	γ_{LS}	0.31	J/ m^2	
Molar volume	V_{mol}	7.09×10^{-6}	m^3/mol	
GIBBS-THOMSON coefficient	$\Gamma = \gamma_{LS} T_L V_{mol} \Delta H_f^{-1}$	2.532×10^{-7}	K m	
Growth parameter	V_0	-	m/s	
Diffusion speed in bulk liquid	V_D	14	m/s	
Interface diffusion speed	V_{DI}	2.5	m/s	
Interfacial kinetic coefficient	$\mu_k = V_0 \Delta H_f / R_G T_L^2$	0.006	m/(K s)	
Interface anisotropy parameter	ε_C	0.01		
Stability constant parameter	σ_0	5		
Stability constant	$\sigma^* = \sigma_0 \cdot \varepsilon_C^{7/4}$	0.00158		
First asymptotic parameter	a_1	0.1		
Second asymptotic parameter	a_2	0.029		

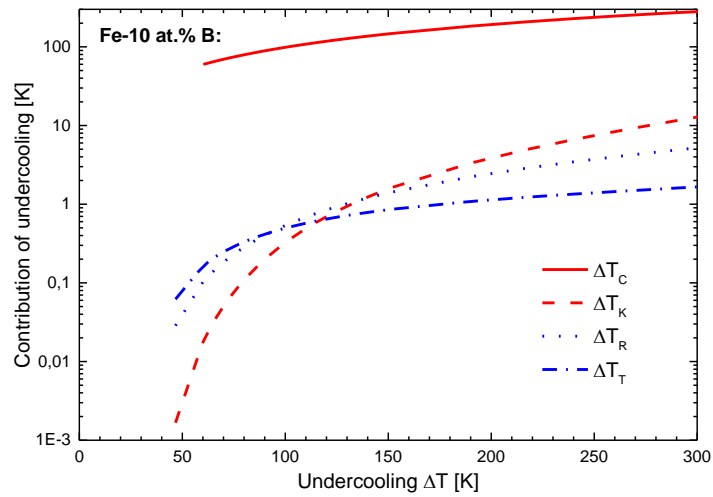


Figure 6-30: Contributions of undercooling as a function of the total undercooling ΔT for Fe-10 at.% B: Constitutional undercooling ΔT_C , kinetic undercooling ΔT_K (blue dashed), thermal undercooling ΔT_T (blue dash-dotted), and curvature undercooling ΔT_R (red dotted)

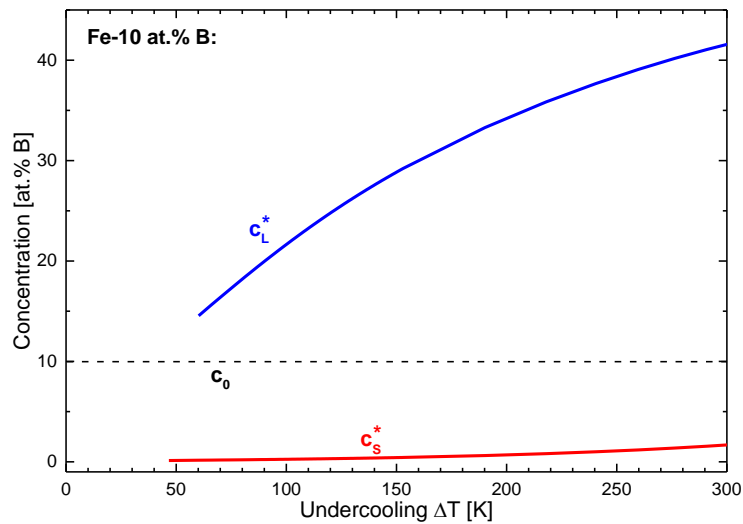


Figure 6-31: Concentration of B at the growing dendrite tip in the liquid c_L^* (blue) and the solid c_S^* (red).

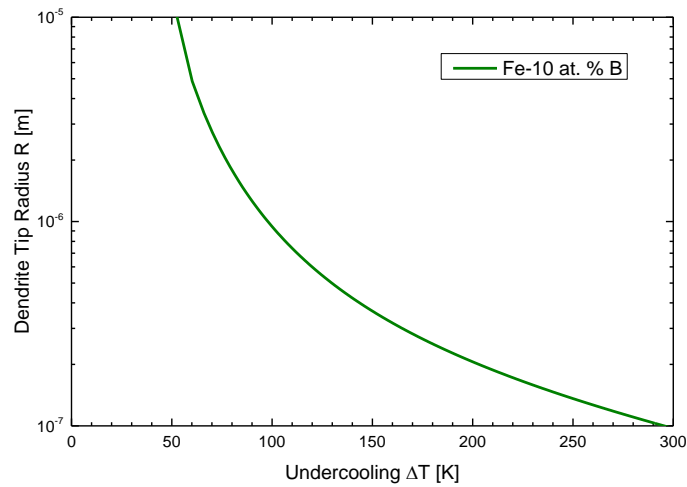


Figure 6-32: Half-logarithmic plot of the theoretical operating dendrite tip Radius R as a function of undercooling ΔT for Fe-10 at.% B.

6.4 Eutectic composition Fe-17 at.% B

In this work, rapid solidification of undercooled Fe-17 at.% B eutectic alloy was studied. The presented eutectic dendrite growth model (Chapter 3: Eutectic growth) is an extension of previous models [72, 73] for concentrated alloys with non-linear phase-diagram (NLPD). The measured growth velocity as a function of undercooling is accurately predicted by the current eutectic dendrite model for concentrated alloys with NLPD. Previous models for dilute alloys with linear phase-diagram could not predict the measured behavior. To the best knowledge of the author, this is the first report where experimental results of eutectic dendrite growth velocities in undercooled melts can be predicted successfully. The experimental and modelling results were published in *Scripta Materialia* [63].

Eutectic solidification is a cooperative growth of two phases. However the Fe₂B phase additionally competes with the metastable Fe₃B phase [112, 113]. The maximum achieved undercooling was $\Delta T = 217 \text{ K}$. Note that, the maximal undercooling in the current work is much smaller than $\Delta T = 386 \text{ K}$ where a metastable Fe₃B phase was found [114]. Therefore the studied eutectic dendrite is assumed to be solely crystallized by a cooperative growth of γ -Fe and Fe₂B.

In order to investigate the microstructure of a Fe-17 at.% B sample, an μg -EML parabolic flight sample is analysed by SEM.

6.4.1 Eutectic Dendrite Growth Velocities $v(\Delta T)$

The eutectic composition shows a smooth growth front (see section 6.1) which can be estimated as a spherical morphology. Therefore all videos are analysed as described in chapter A.1 with the assumption of isotropic growth.

In 1997 BATTEZZATI et al. calculated the dendrite growth velocities for different undercoolings of Fe-17 at.% B which are tabulated in Table 6-6 [115]. The measured growth velocities in this thesis are about one order of magnitude larger than predicted by BATTEZZATI.

Table 6-6: Calculated growth velocities from Battezzati et al. [115] as a first estimation to describe growth behaviour of Fe-17 at.% B

Undercooling ΔT [K]	Calculated growth velocity v [m/s]
50	1.5×10^{-4}
100	5×10^{-4}
200	1.1×10^{-3}

Therefore a more advanced theoretical approach is needed to describe the growth behaviour of Fe-17 at.% B eutectic alloy as a function of undercooling. In fact it is not one single primary phase growing but two phases grow cooperative.

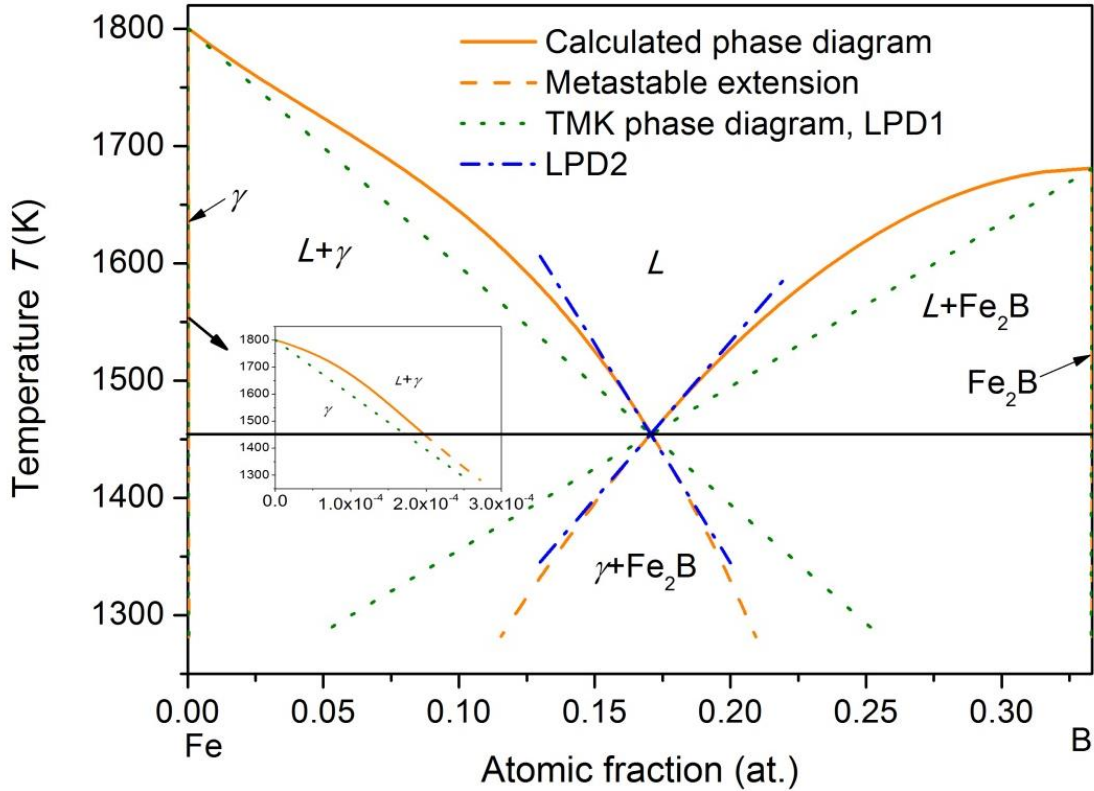


Figure 6-33: Equilibrium phase diagram of the Fe-B eutectic alloy and its metastable extension according to the thermodynamic optimization of Rompaey et al. [116]. It is approximated as the second type of LPD in the TMK model [68] LPD1, and LPD2 (slopes of equilibrium liquidus are given by the values at the eutectic point).

The equilibrium Fe-B eutectic phase-diagram is shown in Figure 6-33. Its metastable extensions are calculated according to the thermodynamic treatment of ROMPAEY et al. [116] which is indicated by solid and dashed lines. The γ -Fe solid-solution phase on the left hand side has a negligible solubility of B, whereas the Fe_2B phase on the right hand side is the stoichiometric compound with a molar fraction $C_{\text{Fe}_2\text{B}} = 1/3$. At the equilibrium eutectic temperature $T_E^e = 1454.4 \text{ K}$, the equilibrium partition coefficients are $k_\gamma^e = 0.00115$ and $k_{\text{Fe}_2\text{B}}^e = (C_{\text{Fe}_2\text{B}} - a)/(C_L^* - a) = 0$, respectively. Here $a = 1/3$ is the composition at which the solidus and liquidus line of Fe_2B intersect [117], and C_L^* is the liquid composition at the interface. Since k_γ^e and $k_{\text{Fe}_2\text{B}}^e$ are negligibly small, the Fe-B eutectic alloy might be approximated reasonably as the second type of LPD in the TMK model [68]. For $k_\gamma^e = k_{\text{Fe}_2\text{B}}^e = k^e = 0.001$, the absolute values of the slopes of γ -Fe and Fe_2B equilibrium liquidus are $m_{L\gamma}^e = 2030 \text{ K at.}^{-1}$ and $m_{L\text{Fe}_2\text{B}}^e = 1395 \text{ K at.}^{-1}$ respectively indicated by dotted lines in Figure 6-33 as LPD1. In this case, the eutectic dendrite growth model of Li and Zhou (LZ) [75] is applicable for TMK-kind LPDs.

The experimental and computed results are summarized in Figure 6-34. In the case of the LZ model LPD1 the experimental results cannot be predicted which is similar to previous works for eutectics [73, 74, 118]. Therefore an eutectic dendrite growth model for undercooled

concentrated alloys with a non-linear phase diagram (NLPD) is proposed. In particular, the non-equilibrium interface kinetics for concentrated alloys [79, 80, 78] and the effect of non-equilibrium solute diffusion in liquid [76] are combined with the dendrite growth model of Galenko et al. [82, 83]. In the calculation, some thermodynamic properties, e.g. the chemical potential μ_i^j ($i = \gamma, Fe_2B$; $j = Fe, B$), latent heat of fusion ΔH_f^i , specific heat of undercooled melt C_p^{Li} and entropy of fusion ΔS_f^i , are obtained directly from the thermodynamic assessment of Rompaey et al. [116]. The mentioned properties were not set to be constant as in the previous works for LPD [73, 74, 118]. Consequently, the experimental results can be well predicted (solid line in Figure 6-34). It must be pointed out that the velocity-dependent partition coefficients and slopes of liquidus ascribing the non-equilibrium kinetics are currently incorporated into the LZ model [75]. In this case, the only difference between the current and the LZ model is whether the assumption of dilute alloys with LPD is adopted or not. A concise description of the LZ model [75] and a detailed derivation of the current model can be found in chapter 3.1. The physical parameters used in model calculations are given in Table 6-7. The two model predictions are almost coincident at low undercoolings ($\Delta T \leq 50 K$) and the deviation between them is extremely significant at high undercoolings. Therefore it can be concluded that the assumption of dilute alloys with LPD is only applicable for small undercoolings.

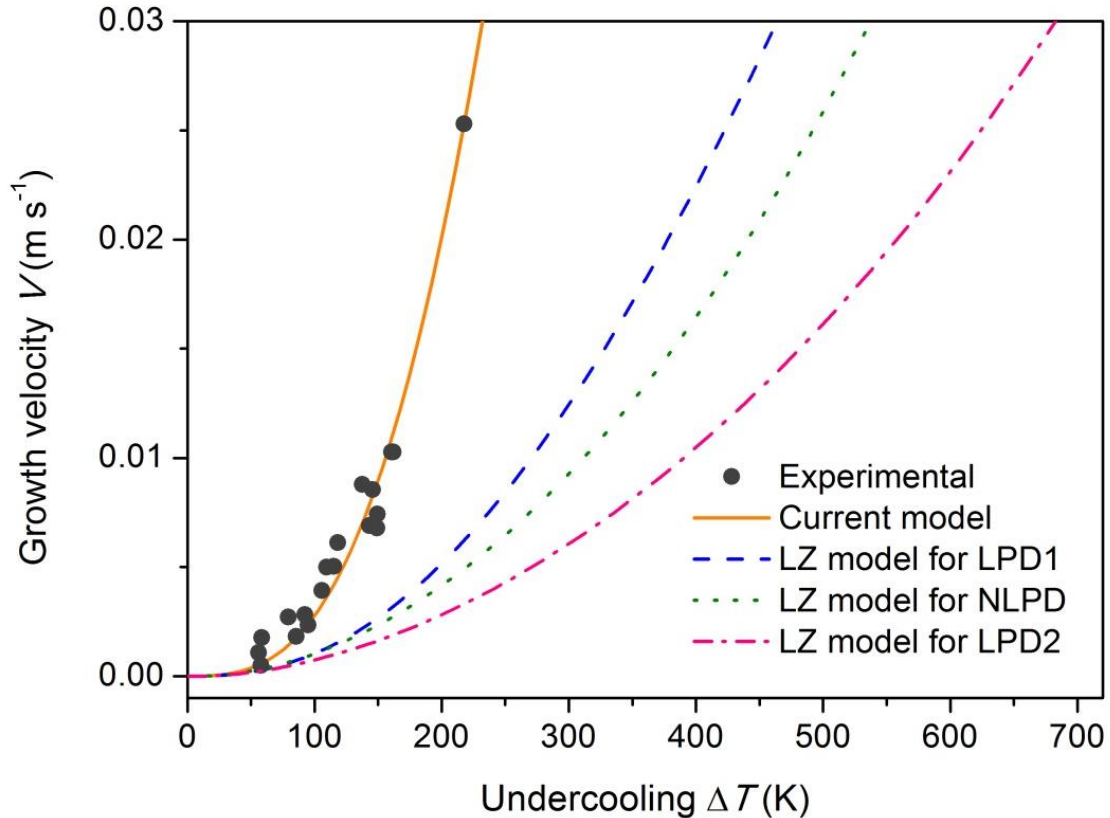


Figure 6-34: Eutectic dendrite growth velocities V as a function of undercooling ΔT . The predictions are plotted for the current model for NLPD (solid line), LZ model [75] for LPD1 (dashed line), NLPD (dotted line), and LP2 (dash-dotted line).

Table 6-7: Thermodynamical, physical and material parameters of the Fe-17 at.% B eutectic alloy used for modelling.

Parameter	Symbol	Numerical value	Unit	Ref.
Concentration of Boron	C_0	17	at. %	
Eutectic equilibrium temperature	T_e	1454.4	K	
Interfacial solute diffusion velocity	V_{DL}^I	0.5	m/s	
Solute diffusion velocity in liquid	V_{DL}	1	m/s	
Upper limit velocity for interface migration	V_0	450	m/s	
Solute diffusion coefficient in liquid	D_L	3×10^{-10}	m^2/s	
Thermal diffusion coefficient	α_L	1.5×10^{-5}	m^2/s	
Molar volume	V_m	6.675×10^{-6}	m^3/mol	
Interface tension of γ/L interface	$\sigma_{\gamma/L}$	0.3	J/m ²	
Interface tension of Fe ₂ B interface	$\sigma_{Fe_2B/L}$	0.5	J/m ²	
Anisotropy coefficient	ε_C	0.006		
Equilibrium solute partition coefficient	k_e	0.001		
Volume fraction of γ	f_γ	0.492		
Slope of equilibrium liquidus of γ	m_{LY}^e	2030	K/at. %	
Slope of equilibrium liquidus Fe ₂ B	$m_{LFe_2B}^e$	1395	K/at. %	

At high undercoolings, the eutectic dendrite growth is dominated by non-equilibrium kinetics. In this case, the interface temperature T_I decreases significantly with increasing undercooling ΔT (solid and dashed lines in Figure 6-35(a)). In particular, the interface temperature T_I deviates considerably from the equilibrium eutectic temperature T_E^e (e.g. $T_E^e - T_I = 382 K$ for the current model and $T_E^e - T_I = 443 K$ for the LZ model [75] using LPD1 at $\Delta T = 600 K$). Furthermore the equilibrium partition coefficients and the slopes of equilibrium liquidus which are a function of T_I may differ significantly from the values at the equilibrium eutectic temperature T_E^e . In the current model, k_γ^e increases from 0.00115 at $\Delta T = 0 K$ to 0.00162 at $\Delta T = 600 K$ (dotted line in Figure 6-35(a)). However $k_{Fe_2B}^e$ stays zero for all undercoolings ΔT . In conclusion, the variation of equilibrium solute partition coefficients with ΔT is not significant which means $k_\gamma^e = k_{Fe_2B}^e = k^e = 0.001$ is a reasonable approximation by LPD1 in Figure 6-33. On the contrary the slopes of equilibrium liquidus m_{LY}^e and $m_{LFe_2B}^e$ increase substantially from $m_{LY}^e = 3733 K at.^{-1}$ and $m_{LFe_2B}^e = 2684 K at.^{-1}$ at $\Delta T = 0 K$ to $m_{LY}^e = 7115 K at.^{-1}$ and $m_{LFe_2B}^e = 4914 K at.^{-1}$ at $\Delta T = 600 K$, respectively (solid and dashed lines in Figure 6-35(b)). Obviously $m_{LY}^e = 2030 K at.^{-1}$ and $m_{LFe_2B}^e = 1395 K at.^{-1}$ are adopted by the LPD1 in Figure 6-33 whereas the deviation from the actual temperature-dependent slopes of the equilibrium liquidus line is already considerable even at $\Delta T = 0 K$ (compare dashed and dash-dotted lines in Figure 6-35(b)). The LPD1 is plausible for rapid solidification in the case of Fe-B eutectic alloy. However if the slopes of equilibrium liquidus are given by the values at the eutectic point (i.e. $m_{LY}^e = 3733 K at.^{-1}$ and $m_{LFe_2B}^e = 2684 K at.^{-1}$), a more reasonable LPD2 can be introduced (dash-dotted lines in Figure 6-33). Its prediction for high undercoolings (dash-dotted line in

Figure 6-34) becomes even worse as LPD1. This behaviour is an unreasonable amplification of non-equilibrium effects by the assumption of LPD which will be discussed in the following.

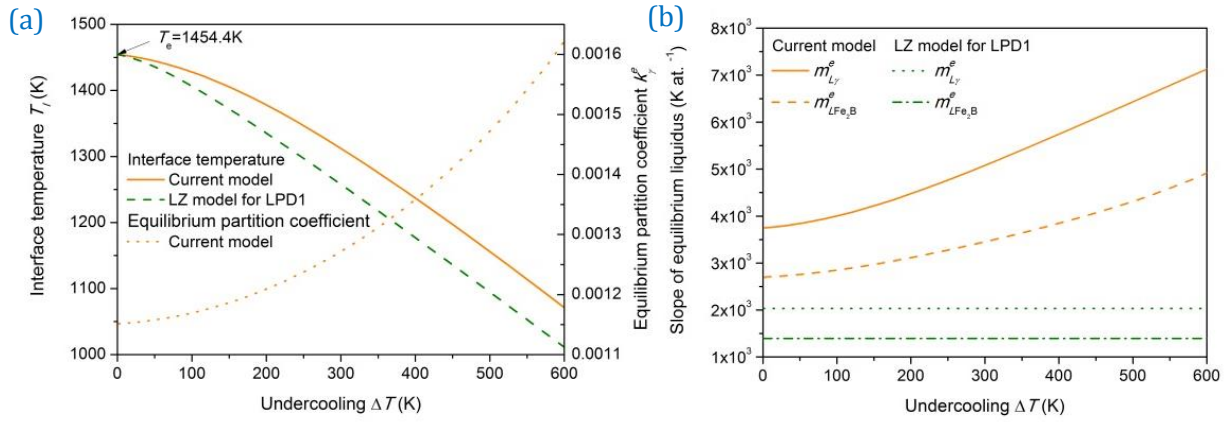


Figure 6-35: Interface temperature T_I , equilibrium partition coefficient k_γ^e (a), slopes of equilibrium liquidus $m_{L\gamma}^e$ and $m_{LFe_2B}^e$ (b) as a function of undercooling ΔT in the current model and the LZ model [75] for LPD1.

The non-equilibrium partition coefficients and the slopes of kinetic liquidus as a function of undercooling are shown in Figure 6-36. For the solid-solution phase γ -Fe, the kinetic partition coefficient k_γ increases from 0.00115 at $\Delta T = 0\text{ K}$ to 0.00209 at $\Delta T = 600\text{ K}$. The slope of kinetic liquidus $m_{L\gamma}$ increases from 3733 K at.^{-1} at $\Delta T = 0\text{ K}$ to 5700 K at.^{-1} at $\Delta T = 600\text{ K}$ (solid lines in Figure 6-36 (a) and (b)). For the stoichiometric phase Fe_2B , the kinetic partition coefficient $k_{Fe_2B} = k_{Fe_2B}^e = 0$ is constant and independent from ΔT [80, 78]. Whereas the slope of kinetic liquidus m_{LFe_2B} increases from 2684 K at.^{-1} at $\Delta T = 0\text{ K}$ to 6469 K at.^{-1} at $\Delta T = 600\text{ K}$ (dashed line in Figure 6-36 (a) and (b)). Regarding that $k_\gamma^e = 0.00162$, $k_\gamma = 0.00209$, $m_{L\gamma}^e = 7115\text{ K at.}^{-1}$, $m_{L\gamma} = 5700\text{ K at.}^{-1}$, $m_{LFe_2B}^e = 4914\text{ K at.}^{-1}$ and $m_{LFe_2B} = 6469\text{ K at.}^{-1}$ at $\Delta T = 600\text{ K}$, the non-equilibrium effect on the partition coefficient and the slopes of liquidus is so significant that it should be considered. As has been shown by the dashed and dash-dotted lines in Figure 6-34, an implementation of the non-equilibrium effect into the LZ model [75] is however not sufficient. If not only velocity-dependent but also temperature-dependent $m_{L\gamma}$ and m_{LFe_2B} in the current model, i.e. the NLPD effect, are incorporated into the LZ model [75], the experimental results can be described better but is still not satisfactory (dotted line in Figure 6-34). These results differ to the recent work of Wang et al. [119, 120] in which the transition from eutectics to glass can be described successfully by taking into consideration the non-equilibrium kinetics for dilute alloys with NLPD.

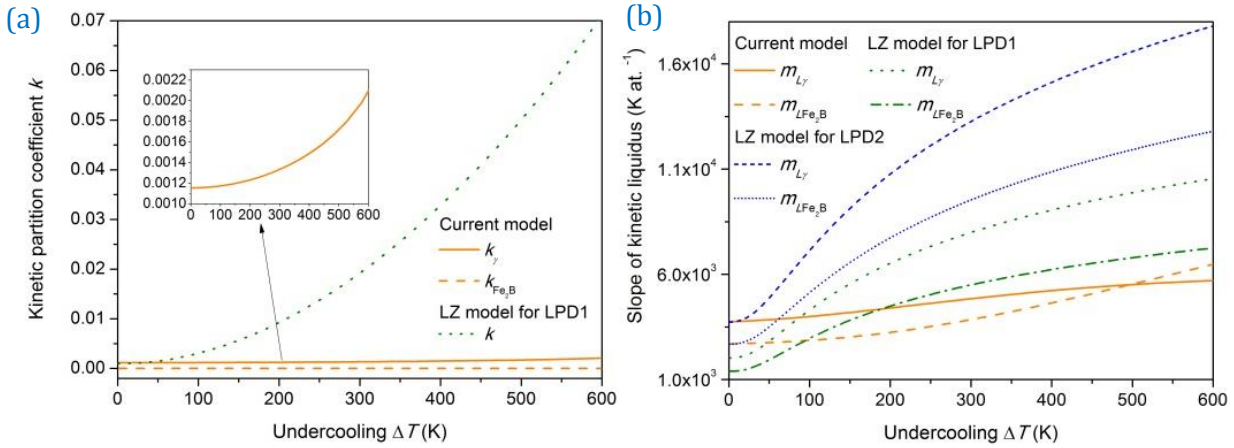


Figure 6-36: Non-equilibrium partition coefficients (a) and slopes of non-equilibrium liquidus (b) as a function of undercooling ΔT in the current model, the LZ model [75] for LPD1 and LPD2.

In the current work, the interface kinetic models for concentrated alloys [79, 80, 78] are followed. If dilute alloys are assumed for the interface kinetics as that in the LZ model [75], the non-equilibrium kinetic effect on k_γ and $m_{L\gamma}$ are amplified artificially (dotted lines in Figure 6-36(a), dotted and short-dashed lines Figure 6-36(b)), whereas for Fe_2B , unreasonable solute trapping occurs (dotted line in Figure 6-36(a)) and the kinetic effect on m_{LFe_2B} is also increased arbitrarily (the dash-dotted and short-dotted lines in Figure 6-36(b)). Even though the kinetic slopes for the LZ model with LP2 are much closer to the current model with NLPD at low undercooling, they deviate more significantly than the LZ model with LPD1 for high undercooling. This is the reason why the LZ model for LPD2 predicts worse than the LZ model for LPD1 as shown previously. The assumption of dilute alloys can amplify unreasonably non-equilibrium effect. Consequently this should be abandoned to describe rapid eutectic solidification. It must be pointed out that a very interesting result is that at $\Delta T = 600 K$, $m_{L\gamma}$ is much smaller than $m_{L\gamma}^e$ in the case of concentrated alloys, in contrast to the case of dilute alloys.

In conclusion, the eutectic dendrite growth velocities of 1g-EML experiments in undercooled Fe-17 at.% B eutectic alloy can be well predicted by the model presented in this thesis for concentrated alloys with NLPD. The extension of model of eutectic solidification to describe concentrated alloys with NLPD may be of general meaning. Therefore the presented experimental results and modelling will be published in *Scripta Materialia* (2015).

As an outlook, the current model can be extended by implementing fluid flow. Figure 6-37 shows melt fluxing experiments in comparison to 1g-EML experiments. Obviously the MF experiments show slower growth velocities $V(\Delta T)$ compared to 1g-EML. According to these results, the eutectic growth behavior depends strongly on the fluid flow conditions.

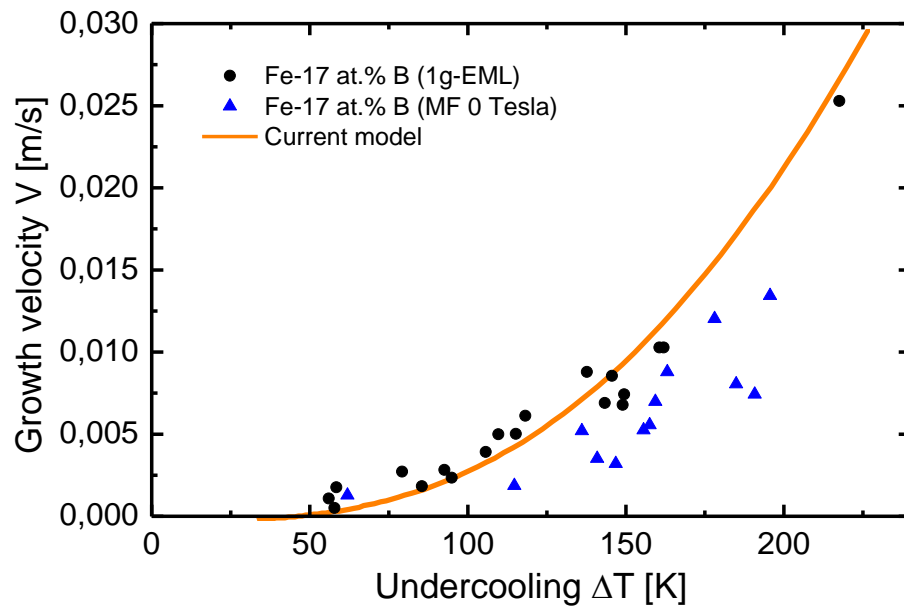


Figure 6-37: Growth velocity V as a function of undercooling ΔT 1g-EML and Melt Fluxing (MF) experiments

6.4.2 Microstructure Analysis of Fe-17 at.% B

The microstructure analysis of a parabolic flight sample with an undercooling $\Delta T = 43 K$ shows similar results as described by YANG et. al [112]. A cross-section of the parabolic flight sample in Figure 6-38 shows mainly solidified eutectic structures and square/rod-like structures with eutectic structure inside. Significant at the surface of the sample are rod-like needles which are exposed in a shrinkage hole (Figure 6-39).

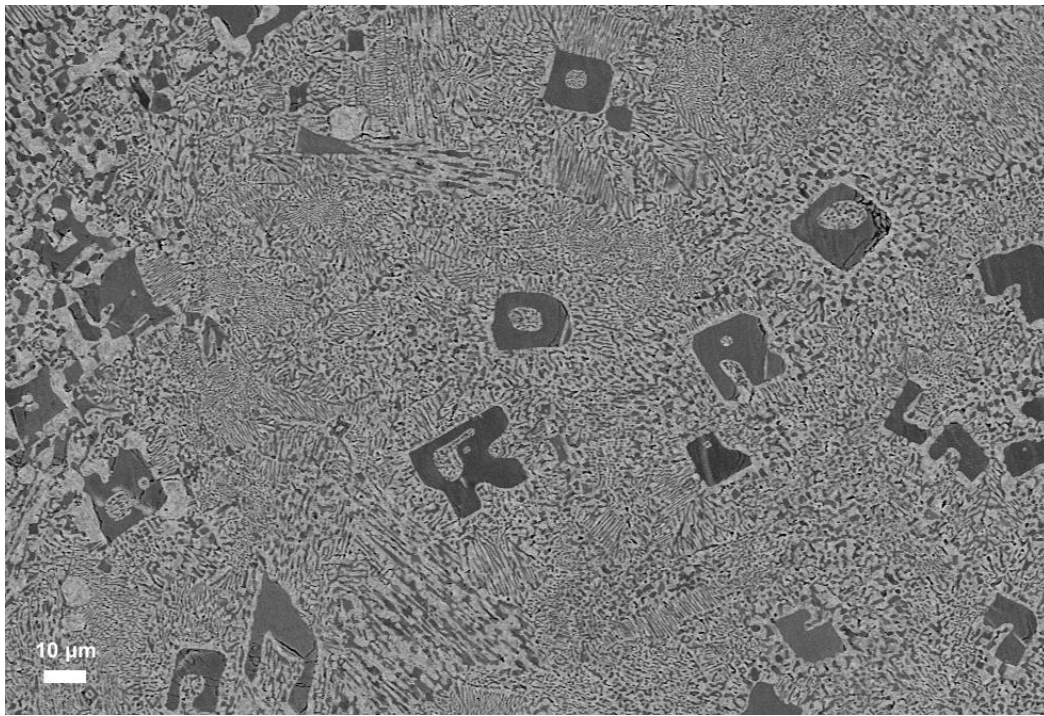


Figure 6-38: Crosssection of Fe-17 at.% B eutectic parabolic flight sample

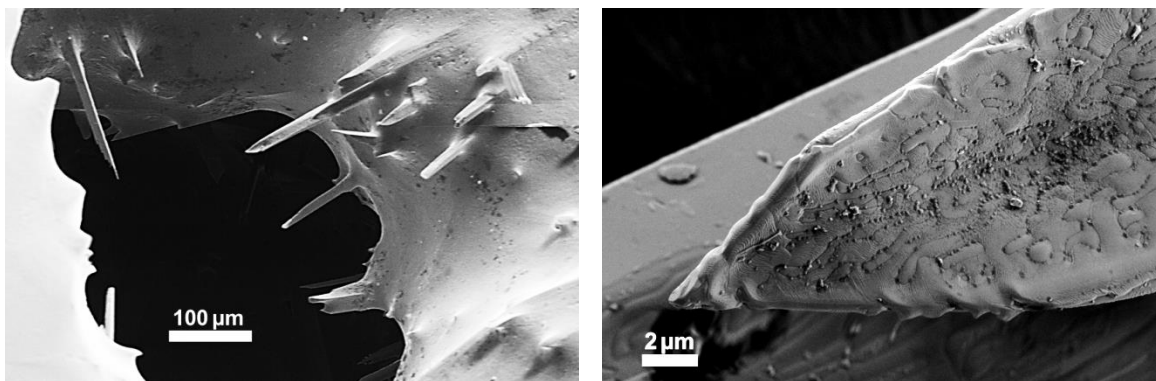


Figure 6-39: Surface SEM images of Fe-17 at.% B solidified sample under microgravity conditions during parabolic flight. The left image shows a shrinkage hole originating from the end of solidification where rod-like structure are exposed. The right image shows a more detailed picture of such a rod-like tip.

SUMMARY

If I have seen further it is by standing on the shoulders of giants.

ISAAC NEWTON (1643-1727)

The fundamental understanding of *solidification kinetics* and how complex structures (crystals) built from a disordered metallic melt is of general scientific interest. Applied science can profit from this knowledge to design materials from the melt and improve material properties. Recent developments in the field of solidification science like atomistic and phase-field modelling techniques as well as new experiments have led to major progress during the first years of this century [2]. However, there are still many open questions to be answered and experimental challenges to be overcome, before the mechanism of *non-equilibrium solidification* is completely understood. Therefore, it is essential to measure key factors which can be compared to predictions of phase-field modelling and molecular dynamic simulations. Furthermore, these parameters can be used to improve and falsify solidification models. The focus of the present work lies on the *growth kinetics of non-equilibrium dendritic and eutectic solidification* in the binary Fe-B system under *different convective fluid flow conditions*. The binary Fe-B system offers to study manifold growth phenomena in dendritic (Fe-1, 5, 10 at.% B) and eutectic (Fe-17 at.% B) alloys. Mainly, solidification is governed by heat and mass transport, while the evolution of the microstructure is determined by the solid-liquid interface and convective effects. In particular, key factors of the solid-liquid interface are of major interest, including its anisotropic nature which governs the solidification pattern evolution. These are the solid-liquid interface free energy γ , its anisotropy ε , and the kinetic growth coefficient μ_k . However, they are not directly accessible by experiments. In order to determine those parameters, the *growth velocity* V can be studied as a function of *undercooling* ΔT . In the case of metals, the dependence of $V(\Delta T)$ varies from 10^{-2} m/s up to several 10 m/s depending on the undercooling ΔT (50 – 300 K) prior to solidification and the concentration of the alloy. The influence of convection (fluid flow inside the melt) on the growth morphology and the growth velocity is investigated by applying different experimental methods (containerless and melt fluxing experiments). The growth velocity results are discussed within current solidification models which provide the desired parameters as “best fit” values.

Rapid solidification of undercooled melts is accessible by containerless processing and melt-fluxing techniques. Heterogeneous nucleation on container walls is avoided in levitation experiments and the solidification process can be directly observed (*in-situ*). During rapid solidification of an undercooled melt, latent heat is released (recalescence). This leads to a contrast between the undercooled liquid (dark) and solid (bright). The advancement of the solidification front is observed by a high-speed video camera. In earth laboratory

electromagnetic levitation (1g-EML), experiments are carried out to undercool and solidify samples of about 7 mm of diameter and 1 g in mass. However, strong electromagnetic fields are necessary to levitate a liquid droplet against gravity, which induces convective fluid flow inside the liquid sample due to electromagnetic stirring (forced convection). The fluid flow velocity U_0 in the case of 1g-EML is about 0.3 m/s [9]. In order to investigate the influence of convection, experiments under reduced gravity conditions are performed with the TEMPUS facility (μ g-EML). This experimental method is used during parabolic flight missions aboard an AIRBUS A300 Zero-G which fulfils a parabolic flight manoeuvre providing about 22 s of reduced gravity (microgravity). Only a weak positioning field is necessary for levitation. This limits the fluid flow velocity in μ g-EML to about 0.05 m/s [9], which is one order of magnitude smaller than in 1g-EML. In addition, melt-fluxing (MF) experiments without levitation in earth laboratory are performed. MF combined with a static magnetic field (produced by a superconducting magnet) provides different fluid flow conditions due to magnetic damping. At 2 T for instance, the fluid flow is comparable to μ g-EML [92].

Experiments with an Infrared-camera (IRC) instead of a high-speed video camera (HSC) are performed. This is especially interesting for low undercoolings ($\Delta T < 50$ K) and low melting materials which show no strong contrast between solid and liquid in the visible light region. It could be shown, that IR-cameras make it possible to observe the solidification processes of low melting materials and are suitable for measurements of growth velocities up to 1 m/s. Furthermore the thermal field around a growing dendrite may be visible for faster IRC with higher resolution.

A *sharp interface model* by GALENKO and DANILOV [44, 45, 59, 60] is used to model the experimental dendrite growth velocity data $V(\Delta T, U_0)$ as a function of undercooling ΔT and fluid flow velocity U_0 . This model is an extended and modified version of the LKT-model by LIPTON, KURZ and TRIVEDI [46]. In contrast to *phase-field modelling*, the sharp interface model includes solute trapping and is much less complex than Phase-field models applied for near equilibrium solidification [121]. The experimental results (1g-EML, μ g-EML and MF) and modelling show strong influence of convection on the growth velocity at small undercoolings, especially if the dendrite growth velocity is in the same order of magnitude as the fluid flow velocity. Increasing fluid flow conditions lead to faster dendrite growth due to enhanced heat and mass transport in the melt.

The dendrite growth velocity results for Fe-B as a function of undercooling show a strong *dependence on B concentration* (pure Fe, Fe-1, 5 and 10 at.% B). Pure Fe dendrite growth velocities vary from about one m/s at low undercoolings ($\Delta T < 100$ K) up to 30 m/s for large undercoolings ($\Delta T \approx 300$ K). By adding B to Fe the growth velocity slows down drastically. This

can be explained due to the small equilibrium partitioning coefficient $k_E \ll 1$ of B in Fe. The first regime is the diffusion limited ($80\text{ K} < \Delta T < 160\text{ K}$) which is described well by the model. Second regime is the transition from diffusion limited to thermally controlled ($160\text{ K} < \Delta T < 190\text{ K}$) with the active development of *solute trapping*. At an undercooling of about 160 K the Fe-1 at.% B alloy shows a sharp increase in the growth velocity from 10^{-2} m/s to about 14 m/s . Solute trapping occurs ($\Delta T > 160\text{ K}$) where B atoms are forced to higher concentration as their equilibrium solubility in the solid. This leads to a supersaturated solid solution. Another aspect is that the dendrite growth velocity of Fe-1 at.% B seems to be even faster than that of pure Fe at an undercooling of about 160 K , which can be explained by slim solutal dendrites growing even faster as thick thermal dendrites of a pure metal. This effect has also been observed for Ni-C [111]. The third regime ($\Delta T > 280\text{ K}$) is the totally thermal controlled part with almost partition less solidification. The parameter used for modelling include the desired values for the solid-liquid interface free energy $\gamma = 0.31\text{ Jm}^{-2}$, its anisotropy $\varepsilon = 0.03$, the kinetic growth coefficient $\mu_k = 0.118\text{ mK}^{-1}\text{s}^{-1}$, and the equilibrium partition coefficient $k_E \approx 0.001$. In the case of rapid solidification, the solute partition coefficient, becomes a function of the growth velocity V which was introduced by AZIZ and KAPLAN [38, 39] expressed by the non-equilibrium partition coefficient $k(V)$. However $k = 1$ is only realized in their model for an infinite growth velocity $V = \infty$ (complete solute trapping). Therefore GALENKO [42] proposed an additional kinetic parameter by introducing a finite diffusion velocity in the bulk liquid V_D . The model by GALENKO describes the growth behaviour of Fe-1 at.% B including solute trapping much better as the model by AZIZ and KAPLAN. Furthermore the model by GALENKO was recently confirmed by molecular dynamics simulations (MD) [43].

Not only the growth velocity but also the *growth morphology* is influenced by fluid flow in the melt. The studies on Fe with 1, 5, and 10 at.% B alloys show unexpected *bent dendrite growth* up to certain undercoolings in ground-based 1g-EML and μg -EML [8]. This phenomenon has been observed *in-situ*, as far as we know, for the first time in solidifying metals during levitation. In the future, the effect of bent growing dendrites may be used to manipulate the microstructure development during solidification. For example, dendrites could be bent during growth to follow the curving of a turbine blade or guided growing dendrites of semiconductor on substrates could lead to new technologies.

Fe-5 and 10 at.% B show a strong influence of convection on the growth velocity as a function of undercooling. The measured growth velocities (1g-EML, μg -EML, and MF) have a large error/scatter and should be interpreted with care. The influence of convection on the growth velocity is underestimated by the used two-dimensional solidification model. Unrealistic fluid flow velocities of above 1 m/s are necessary to describe the experimental results of Fe-10 at.%

B. The appearance of solute trapping cannot be proofed for Fe-5 at.% B as well as the competition between primary bcc and fcc structure crystallization. The Fe-10 at.% B alloy was qualified within this thesis due to a parabolic flight experiment as a sample for EML batch 2 in 2015/16 aboard the International Space Station (ISS) as part of the MAGNEPHAS project. These future experiments under reduced gravity conditions will help to clarify the influence of convection on bent growth behaviour and growth velocity as a function of undercooling.

Going one step further by adding more B (Fe-17 at.% B) the dendritic growth shifts to eutectic solidification where two phases grow cooperatively (Fe-B and Fe₂B). Fe-B as a *metallic glass* former has the ability to solidify amorphous. The glass temperature for Fe-17 at.% B is about 800 K [7]. However to form an amorphous Fe-B glassy alloy, a high cooling rate of approximately 1000 K/s (e.g. rapid quenching technique) is necessary, which cannot be achieved by the used methods. Besides dendrites, eutectic structures are the most commonly observed microstructure in casting [122]. In the case of eutectics, two solid phases grow cooperatively with a nearly planar solid-liquid interface. The size of the eutectic lamellar spacing is close to the growing dendrite tip radius. However, this is much finer than the primary and secondary arm spacing of dendrites which gives eutectics improved mechanical properties. In the case of near equilibrium eutectic solidification, the solute diffusion and interface energy effects dominate while the thermal gradient effects are negligible. However, turning to non-equilibrium rapid solidification the thermal effects have to be taken into account. In the present work non-equilibrium eutectic growth was investigated in undercooled Fe-17 at.% B eutectic alloy by measuring the growth velocity V as a function of undercooling ΔT . The experimental results of the concentrated eutectic alloy Fe-17at.% B cannot be approximated as a dilute alloy with classical eutectic growth models (JACKSON-HUNT model with linear phase diagram). In order to describe the growth velocity as a function of undercooling, a new model is presented in this thesis for concentrated alloys with non-linear phase diagram (NLPD) [63]. The experiments were done by the author of the thesis and the modelling part was done in cooperation by Prof. HAIFENG WANG and KUAN WANGWANG from the Northwestern Polytechnical University of Xi'An.

A APPENDIX

A.1 Video Analysis of Dendrite Growth Velocity

According to section 6.1 (growth morphology) the analysis of the videos leading to the correct growth velocity needs certain assumptions. In most cases two types of crystallisation fronts can be observed: an octahedral shaped pattern and a spherical pattern.

One method of analysing videos was done with the 3D modelling software *POV-Ray* and the implementation of Dr. SVEN BINDER [98, 123]. The underlying octahedral shape for pure Fe with its center at the surface of the spherical sample visualises the intersection with a sphere.

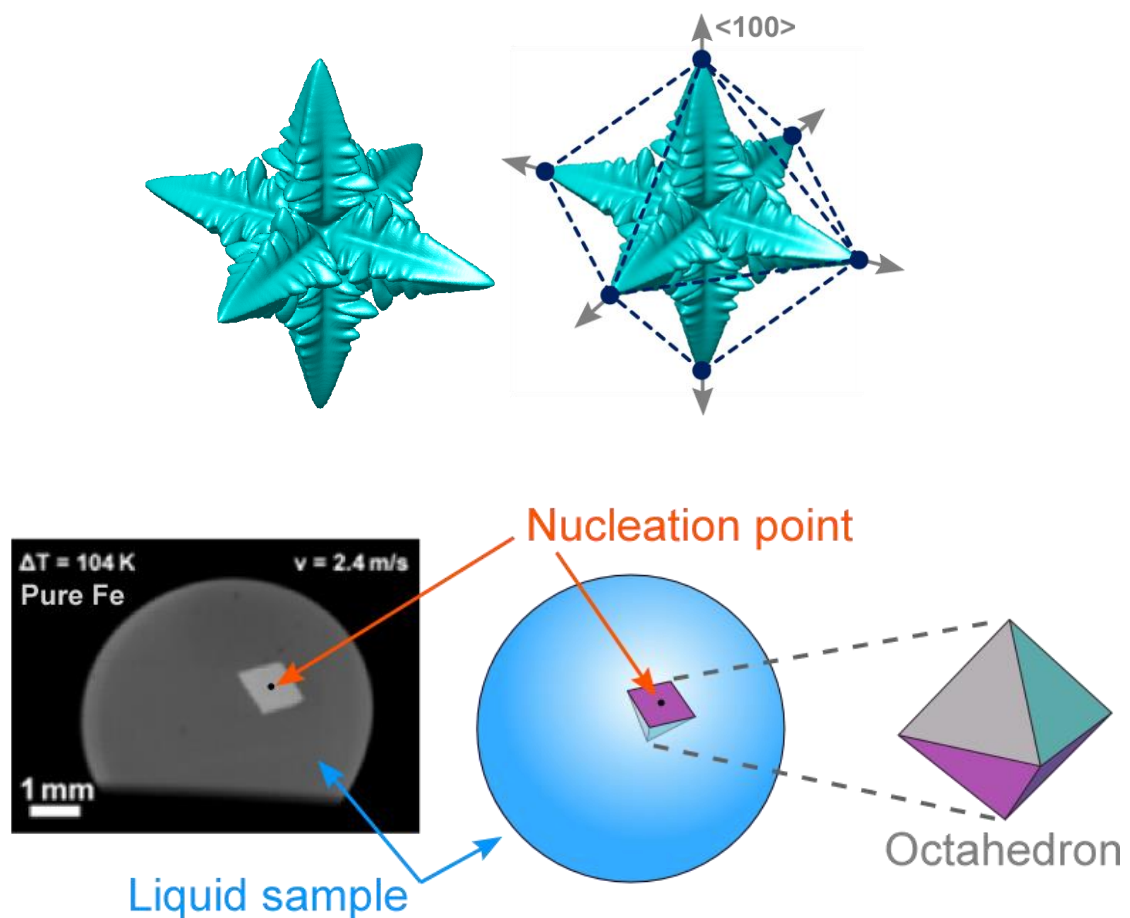


Figure A-1: Growing dendritic crystal forming an octahedron with preferred $\langle 100 \rangle$ direction [4]. The center of the octahedron (assumed nucleation point) put at the surface of a sphere leads to the following intersection pattern. This pattern can be observed during crystal growth for pure Fe samples.

For larger B concentrations the octahedral front becomes more spherical. Therefore the program *FRONT TRACKING TOOL* (FTT) written by Dr. JAN GEGNER in *MatLab* was used to analyse solidification videos with spherical front. Assuming isotropic growth... The program can load an AVI-video and displays individual frames to project the growth of an idealized spherical solid within a liquid spherical sample. To calibrate the size of the sample the diameter is required. The frame rate defines the time t [s] elapsing between each frame. Once the circle sample radius, sample center, nucleation point and solidification front is matched to the video image and repeated frame by frame, the program calculates the growth distance.

The plot of the data represents the growth distance s [mm] on the y-axis against time t [s] on the x-axis. The slope m [mm/s] of the linear regression line is the growth velocity v [mm/s] which is defined by:

$$m = \frac{\sum_{i=1}^n (x_i - \bar{x})(y_i - \bar{y})}{\sum_{i=1}^n (x_i - \bar{x})^2},$$

where \bar{x}, \bar{y} are the mean values and x_i, y_i each data point. The intercept $b = \bar{y} - m\bar{x}$ guarantees that the distance from each data point to the line squared is minimized. This simple linear regression line $\bar{y} = m\bar{x} + b$. least squares regression.

Figure A-2 shows a screenshot of the FFT program as example for a spherical front. The diameter of the sample is 6.7 mm and the high-speed video camera recorded with a framerate of 30,000 fps. After calibrating the sample diameter, the growth front and its center was stepwise selected for each frame. The growth velocity plotted as the slope of growing radius per time which is about 13.4 m/s for this example using 10 frames of solidification.

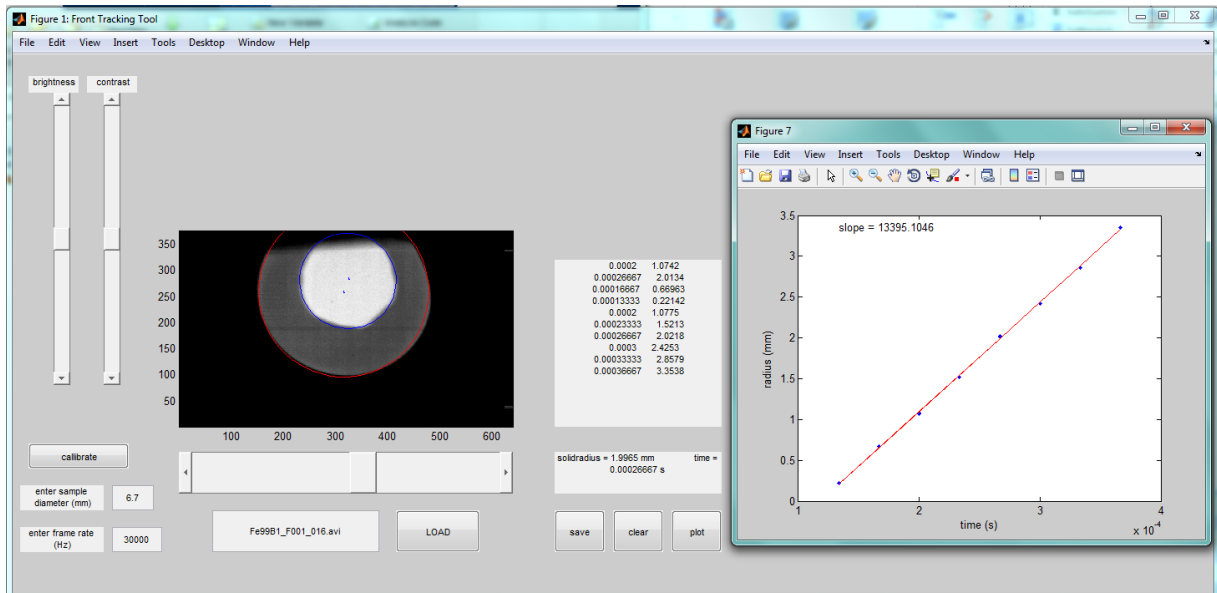


Figure A-2: Screenshot of the program Front Tracking Tool (FFT)

BIBLIOGRAPHY

- [1] M. Rappaz and W. Kurz, "Dendrites solidified by computer," *Nature*, vol. 375, p. 103 pp., 1995.
- [2] M. Asta, C. Beckermann, A. Karma, W. Kurz, R. Napolitano, M. Plapp, G. Purdy, M. Rappaz and R. Trivedi, "Solidification microstructures and solid-state parallels: Recent developments, future directions," *Acta Materialia*, vol. 57, no. 146, pp. 941-971, 2009.
- [3] D. M. Herlach, "Containerless Undercooling and Solidification of Pure Metals," *Annual Review of Material Science*, vol. 21, pp. 23-44, 1991.
- [4] T. Haxhimali, A. Karma, F. Gonzales and M. Rappaz, "Orientation selection in dendritic evolution," *Nature Materials*, vol. 5, pp. 660-664, 2006.
- [5] S. Binder, M. Kolbe, S. Klein and D. M. Herlach, "Solidification of tetragonal Ni₂B from the undercooled melt," *Europhysics Letters*, vol. 97, no. 3, 2012.
- [6] T. B. Cameron and J. E. Morral, *Metallurgical Transactions*, vol. 17, no. A, pp. 1481-1483, 1986.
- [7] M. Palumbo, G. Cacciamani, E. Bosco and M. Baricco, "Thermodynamic Analysis of Glass Formation in Fe-B System," *Calphad*, vol. 25, no. 4, pp. 625-637, 2001.
- [8] C. Karrasch, T. Volkman, J. Valloton, M. Kolbe and D. M. Herlach, "Bent Dendrite Growth in Undercooled Fe-B Alloy Melts," *IOP Conference Series: Material Science and Engineering*, submitted 2014.
- [9] R. W. Hyers, *Meas. Sci. Technol.*, no. 16, pp. 394-401, 2005.
- [10] J. A. Dantzig and M. Rappaz, SOLIDIFICATION, Lausanne, Switzerland: EPFL Press, 2009.
- [11] D. Herlach, P. Galenko and D. Holland-Moritz, METASTABLE SOLIDS FROM UNDERCOOLED MELTS, Amsterdam, London: Elsevier, 2007.
- [12] D. Turnbull, "Formation of crystal nuclei in liquid metals," *Journal of Applied Physics*, vol. 21, pp. 1022-1028, 1950.
- [13] R. R. Hultgren, Selected Values of the Thermodynamic Properties of Binary Alloys, Ohio: American Society for Metals, 1973.
- [14] M. Volmer and A. Weber, "Keimbildung in gesättigten Gebilden," *Zeitschrift für physikalische Chemie*, vol. 119, pp. 277-301, 1926.
- [15] R. Becker and W. Döring, "Kinetische Behandlung der Keimbildung in übersättigten Dämpfen," *Annalen der Physik*, vol. 416, no. 8, pp. 719-752, 1935.

- [16] D. Turnbull and J. C. Fisher, "Rate of Nucleation in Condensed Systems," *Journal of Chemical Physics*, vol. 17, no. 71, 1949.
- [17] R. Becker, "On the Formation of Nuclei during Precipitation," *Proceedings of the Physical Society*, vol. 52, pp. 71-76, 1940.
- [18] M. Volmer, "Über Keimbildung und Keimwirkung als Spezialfälle der heterogenen Katalyse," *Zeitschrift für Elektrochemie und angewandte physikalische Chemie*, vol. 35, no. 9, pp. 555-561, 1929.
- [19] C. V. Thompson, Harvard University: Ph.D. Thesis, 1979.
- [20] C. V. Thompson and F. Spaepen, "Homogeneous Crystal Nucleation in Binary Metallic Melts," *Acta Metallurgica*, vol. 31, pp. 2021-2027, 1983.
- [21] F. Spaepen, "Structural Model for the Solid-Liquid Interface in Mono-Atomic Systems," *Acta Met.*, vol. 23, pp. 729-743, 1975.
- [22] F. Spaepen and R. B. Meyer, "The Surface Tension in a Structural Model for the Solid-Liquid Interface," *Scripta Metallurgica*, vol. 10, pp. 257-263, 1976.
- [23] F. C. Frank, "Supercooling of Liquids," *Proc. Roy. Soc. Lond.*, vol. A 215, pp. 43-46, 1952.
- [24] D. R. Nelson and F. Spaepen, "Polytetrahedral Order in Condensed Matter," *Solid State Physics*, vol. 42, pp. 1-90, 1989.
- [25] W. E. McMullen and D. W. Oxtoby, "A Theoretical Study of the Hard Sphere Fluid-Solid Interface," *J. Chem. Phys.*, vol. 88, pp. 1967-1975, 1988.
- [26] D. Holland-Moritz, *Ordnungsphänomene, fest-flüssig Grenzflächen und Phasenselektion in unterkühlten Metallschmelzen*, Ruhr-Universität Bochum: Habilitationsschrift, 2003.
- [27] Z. Jian, K. Kuribayashi and W. Jie, "Solid-liquid Interface Energy of Metals at Melting Point and Undercooled State," *Materials Transactions*, vol. 42, no. 4, pp. 721-726, 2002.
- [28] J. W. Christian, *The Theory of Transformations in Metals and Alloys*, Oxford: Pergamon, 1975.
- [29] A. A. Chernov, *Modern Crystallography III*, vol. 36, Berlin: Springer, 1984.
- [30] H. A. Wilson, "On the velocity of solidification and viscosity of supercooled liquids," *Philos. Mag.*, vol. 50, pp. 238-250, 1900.
- [31] J. Frenkel, "Note on a relation between the speed of crystallization and viscosity," *Phys. Z. Sowj.*, vol. 1, pp. 498-500, 1932.
- [32] K. A. Jackson, "The Interface Kinetics of Crystal Growth Processes," *Interface Science*, vol. 10, pp. 159-169, 2002.

- [33] W. Klement, R. H. Willens and P. Duwez, "Non-Crystalline Structure in Solidified Gold-Silicon Alloys," *Nature*, vol. 187, no. 4740, p. 869–870, 1960.
- [34] M. Telford, "The Case for Bulk Metallic Glass," *Materials Today*, vol. 7, no. 3, pp. 36-43, 2004.
- [35] Y. H. Liu, G. Wang, R. J. Wang, D. Q. Zhao, M. X. Pan and W. H. Wang, "Super Plastic Bulk Metallic Glasses at Room Temperature," *Science*, vol. 315, no. 5817, pp. 1385-1388, 2007.
- [36] H. Guo, P. F. Yan and Y. B. Wang, "Tensile Ductility and Necking of Metallic Glass," *Nature Materials*, vol. 6, no. 10, pp. 735-739, 2007.
- [37] D. C. Hofmann, "Bulk Metallic Glasses and Their Composites: A Brief History of Diverging Fields," *Journal of Materials*, pp. 1-8, 2013.
- [38] M. J. Aziz, "Model for Solute Redistribution During Rapid Solidification," *Journal of Applied Physics*, vol. 53, pp. 1158-1168, 1982.
- [39] M. J. Aziz and T. Kaplan, "Continuous Growth Model for Alloy Solidification," *Acta Metallurgica*, vol. 36, pp. 2335-2347, 1988.
- [40] W. Kurz and D. J. Fisher, *Fundamentals of Solidification*, Lausanne: Trans Tech Publications, 1989.
- [41] K. Eckler, *Dendritisches Wachstum in unterkuehlten Metallschmelzen*, Ruhr-Universität Bochum: Dissertation, 1992.
- [42] P. K. Galenko, "Solute trapping and diffusionless solidification in a binary system," *Phys. Rev. E*, no. 76, 2007.
- [43] J. J. Hoyt, M. Asta and A. Karma, "Atomistic Simulations of Solute Trapping and Solute Drag," in *Solidification of Containerless Undercooled Melts*, Weinheim, Wiley-VCH, 2012, pp. 363-380.
- [44] P. K. Galenko and D. A. Danilov, "Local Nonequilibrium Effect on Rapid Dendritic Growth in a Binary Alloy Melt," *Physics Letters A*, vol. 235, pp. 271-280, 1997.
- [45] P. K. Galenko and D. A. Danilov, "Model for Free Dendritic Alloy Growth under Interfacial and Bulk Phase Nonequilibrium Conditions," *Journal of Crystal Growth*, vol. 197, pp. 992-1002, 1999.
- [46] J. Lipton, W. Kurz and R. Trivedi, "Rapid Dendrite Growth in Undercooled Alloys," *Acta Metallurgica*, vol. 35, no. 4, pp. 957-964, 1987.
- [47] J. Brillo, A. I. Pommrich and A. Meyer, "Relation between Self-Diffusion and Viscosity in Dense Liquids: New Experimental Results from Electrostatic Levitation," *Physical Review Letters*, vol. 107, no. 165902, pp. 5902-1-4, 2011.

- [48] A. Kerrache, J. Horbach and K. Binder, "Molecular Dynamics Computer Simulation of Crystal Growth and Melting in Al₅₀Ni₅₀," *Europhys. Lett.*, vol. 81, pp. 58001:1 - 6, 2008.
- [49] S. C. Huang and M. E. Glicksman, "Overview 12: Fundamentals of Dendritic Solidification-II. Steady-State Tip Growth," *Acta Metallurgica*, vol. 29, pp. 701-715, 1981.
- [50] D. E. Temkin, "Growth Velocity of a Needle Crystal in a Supercooled Melt," *Dokl. Akad. Nauk SSSR*, vol. 132, pp. 1307-1310, 1960.
- [51] J. S. Langer and H. Müller-Krumbhaar, "Stability Effects in Dendritic Crystal Growth," *Journal of Crystal Growth*, vol. 42, pp. 11-14, 1977.
- [52] J. S. Langer and H. Müller-Krumbhaar, "Theory of Dendritic Growth-I. Elements of a Stability Analysis," *Acta Metallurgica*, vol. 26, pp. 1681-1687, 1978.
- [53] B. Caroli, C. Caroli, B. Roulet and J. S. Langer, "Solvability Condition for Needle Crystals at Large Undercooling in a Nonlocal Model of Solidification," *Physical Review A*, vol. 33, no. 1, pp. 442-452, 1986.
- [54] D. A. Kessler and H. Levine, "Velocity Selection in Dendritic Growth," *Physical Review B*, vol. 33, no. 11, pp. 7867-7870, 1986.
- [55] M. Ben Amar, "Dendritic Growth Rate at Arbitrary Undercooling," *Physical Review A*, vol. 41, no. 4, pp. 2080-2092, 1990.
- [56] A. Barbieri, D. C. Hong and J. S. Langer, "Velocity Selection in the Symmetric Model of Dendritic Crystal Growth," *Physical Review A*, vol. 1987, pp. 1802-1808, 35.
- [57] D. V. Alexandrov and P. K. Galenko, "Selection criterion of stable dendritic growth at arbitrary Péclet numbers with convection," *Phys. Rev. E*, vol. 87, no. 6, pp. 062403:1-062403:5, 2013.
- [58] J.-H. Jeong, N. Goldenfeld and J. A. Dantzig, "Phase field model for three-dimensional dendritic growth with fluid flow," *Phys. Rev. E*, no. 64, 2001.
- [59] P. K. Galenko, O. Funke, J. Wang and D. M. Herlach, "Kinetics of Dendritic Growth under the Influence of Convective Flow in Solidification of Undercooled Droplets," *Materials Science Engineering A*, pp. 375-377, 2004.
- [60] P. Galenko, S. Binder and G. J. Ehlen, "Forced Flow Effect on Dendritic Growth Kinetics in a Binary Non-Isothermal System," in *Solidification of Containerless Undercooled Melts*, Weinheim, Wiley-VCH, 2012, pp. 349-362.
- [61] P. Bouissou and P. Pelcé, "Effect of a Forced Flow on Dendritic Growth," *Phys. Rev. A*, no. 40, p. 6673-6680, 1989.
- [62] K. A. Jackson and J. D. Hunt, *Trans. Metall. Soc. AIME*, vol. 236, pp. 1129-1142, 1966.
- [63] W. Kuang, C. Karrasch, H. Wang, F. Liu and D. M. Herlach, "Eutectic Dendrite Growth in

- Undercooled Fe₈₃B₁₇ Alloy: Experiments and Modeling," *Scripta Materialia*, vol. 105, pp. 34-37, 2015.
- [64] W. Kurz and D. J. Fisher, "Dendrite Growth in Eutectic Alloys: The Coupled Zone," *International Materials Reviews*, vol. 24, no. 1, pp. 177-204, 1979.
- [65] A. Karma and A. Sarkissian, "Morphological Instabilities of Lamellar Eutectics," *Metallurgical Materials and Transactions A*, vol. 27, no. 3, pp. 635-656, 1996.
- [66] H. Walker, S. Liu, J. H. Lee and R. Trivedi, "Eutectic Growth in Three Dimensions," *Metallurgical and Materials Transactions A*, vol. 38, no. 7, pp. 1417-1425, 2007.
- [67] S. Akamatsu, S. Bottin-Rousseau and G. Faivre, "Determination of the Jackson-Hunt Constants of the In-In₂Bi Eutectic Alloy based on In Situ Observation of its Solidification Dynamics," *Acta Materialia*, vol. 59, pp. 7586-7591, 2011.
- [68] R. Trivedi, P. Magnin and W. Kurz, "Theory of Eutectic Growth under Rapid Solidification Conditions," *Acta Metallurgica*, vol. 35, no. 4, pp. 971-980, 1987.
- [69] W. Kurz and R. Trivedi, "Eutectic Growth under Rapid Solidification Condition," *Metall. Trans.*, vol. 22, pp. 3051-3057, 1991.
- [70] H. F. Wang, F. Liu, Z. Chen, G. C. Yang and Y. H. Zhou, "Analysis of Non-Equilibrium Dendrite Growth in Bulk Undercooled Alloy Melt: Model and Application," *Acta Materialia*, vol. 55, pp. 497-506, 2007.
- [71] H. F. Wang, F. Liu, Z. Chen, W. Yang, G. C. Yang and Y. H. Zhou, "Effect of Non-Linear Liquidus and Solidus in Undercooled Dendrite Growth: A Comparative Study in Ni-0.7 at.% B and Ni-1 at.% Zr Systems".
- [72] B. Wei, D. Herlach, B. Feuerbacher and F. Sommer, "Dendritic and Eutectic Solidification of Undercooled Co-Sb Alloys," *Acta Metallurgica & Materialia*, vol. 41, pp. 1801-1809, 1993.
- [73] L. Liu, J. F. Li and Y. H. Zhou, "Solidification Interface Morphology Pattern in Undercooled Co-24.0 at% Sn Eutectic Melt," *Acta Materialia*, vol. 59, pp. 5558-5567, 2011.
- [74] R. Goetzinger, M. Barth and D. M. Herlach, "Physical Mechanism of Formation of the Anomalous Eutectic Structure in Ni-Si, Co-Sb and Ni-Al-Ti Alloys," *Acta Materialia*, vol. 46, pp. 1647-1655, 1998.
- [75] J. F. Li and Y. H. Zhou, "Eutectic Growth in Bulk Undercooled Melts," *Acta Materialia*, vol. 53, no. 8, pp. 2351-2359, 2005.
- [76] P. K. Galenko and D. M. Herlach, "Diffusionless Crystal Growth in Rapidly Solidifying Eutectic Systems," *Physical Review Letters*, vol. 96, p. 150602, 2006.
- [77] H. F. Wang, F. Liu and D. M. Herlach, "On the Solution of Solute Diffusion during Eutectic Growth," *Journal of Crystal Growth*, vol. 389, pp. 68-73, 2014.

- [78] H. F. Wang, F. Liu and D. M. Herlach, "Kinetics of Triple-Junctions in Eutectic Solidification: A Sharp Interface Model," *Journal of Materials Science*, vol. 50, pp. 176-188, 2015.
- [79] H. F. Wang, F. Liu, H. M. Zhai and K. Wang, "Application of the Maximal Entropy Production Principle to Rapid Solidification: A Sharp Interface Model," *Acta Materialia*, vol. 60, pp. 1444-1454, 2012.
- [80] H. F. Wang, F. Liu and D. M. Herlach, "Modeling the Growth Kinetics of a Multicomponent Stoichiometric Compound," *J. Materials Science*, vol. 49, pp. 1537-1543, 2014.
- [81] G. P. Ivantsov, *Dokl. Akad. Nauk. SSSR*, vol. 58, p. 567, 1947.
- [82] P. K. Galenko, S. Reutzel, D. M. Herlach, D. Danilov and B. Nestler, "Modelling of Dendritic Solidification in Undercooled Dilute Ni-Zr Melts.," *Acta Materialia*, vol. 55, p. 6834-6842, 2007.
- [83] P. K. Galenko, S. Reutzel, D. M. Herlach, S. G. Fries, I. Steinbach and M. Apel, "Dendritic Solidification in Undercooled Ni-Zr-Al Melts: Experiments and Modelling," *Acta Materialia*, vol. 57, p. 6166-6175, 2009.
- [84] G. Lohöfer and J. Piller, "The new ISS electromagnetic levitation facility: MSL - EML," *Proceedings 40th AIAA Aerospace Sciences Meeting & Exhibit*, 2002.
- [85] Novespace, "Multimedia," Novespace, 2007. [Online]. Available: <http://www.novespace.fr/en/home/download.html>. [Accessed 11 2015].
- [86] A. Gerst, "twitter.com: 3-2-1 GO! Switching on power to Electromagnetic Levitator #EML - finding alloys on #ISS for the engine of the future," ESA, 05 11 2014. [Online]. Available: https://twitter.com/Astro_Alex/status/529930334960640000?nav=true. [Accessed 09 11 2015].
- [87] NASA, "DLR," NASA, [Online]. Available: http://www.dlr.de/next/desktopdefault.aspx/tabid-7443/12421_read-30013/. [Accessed 11 2015].
- [88] H. Yasuda, I. Ohnaka, Y. Ninomiya, R. Ishii, S. Fujita and K. Kishio, "Levitation of Metallic Melt by Using the Simultaneous Imposition of the Alternating and Static Magnetic Fields," *Journal of Crystal Growth*, vol. 260, pp. 475-485, 2004.
- [89] H. W. Kui, A. L. Greer and D. Turnbull, "Formation of Bulk Metallic Glass by Fluxing," *Applied Physics Letters*, vol. 45, no. 6, pp. 615-616, 1984.
- [90] J. Wu, T. J. Piccone, Y. Shiohara and M. C. Flemings, "Dendritic Growth of Undercooled Nickel-Tin: Part I," *Metallurgical Transactions A*, vol. 18A, pp. 915-924, 1987.
- [91] A. Yeckel and J. J. Derby, "Dynamics of Three-Dimensional Convection in Microgravity Crystal Growth: g-Jitter with Steady Magnetic Fields," *Journal of Crystal Growth*, vol. 263, pp. 40-52, 2004.

- [92] Y. K. Zhang, J. Gao, D. Nagamatsu, T. Fukuda, H. Yasuda, M. Kolbe and J. C. He, "Reduced Droplet Coarsening in Electromagnetically Levitated and Phase-Separated Cu-Co Alloys by Imposition of a Static Magnetic Field," *Scripta Materialia*, vol. 59, pp. 1002-1005, 2008.
- [93] E. Boehm-Courjault, F. Gonzales, A. Jacot, F. Kohler, A. Mariaux, C. Niederberger, M. A. Salgado-Ordorica and M. Rappaz, "EBSD: A Powerful Microstructure Analysis Technique in the Field of Solidification," *Journal of Microscopy*, vol. 233, pp. 160-169, 2009.
- [94] J. Berlin, "Analysis of Boron with Energy Dispersive X-ray Spectrometry," *Imaging & Microscopy*, vol. 13, no. 2, pp. 19-21, 2011.
- [95] H. Okamoto, "B-Fe (boron-iron)," *Journal of Phase Equilibria and Diffusion*, vol. 25, no. 3, pp. 297-298, 2004.
- [96] A. M. Mullis, "Growth induced dendritic bending and rosette formation during solidification in a shearing flow," *Acta Materialia*, vol. 47, pp. 1783-1789, 1999.
- [97] M. Yamaguchi and C. Beckermann, "Simulation of solid deformation during solidification: Compression of a single dendrite," *Acta Materialia*, vol. 61, pp. 4053-4065, 2013.
- [98] S. Binder, Dissertation: Undercooling and Solidification of tetragonal Ni₂B under different convective flow conditions, Bochum, 2010.
- [99] L. Liu, J. F. Li and Y. H. Zhou, "Solidification Interface Morphology Pattern in the undercooled Co-24.0 at.% Sn Eutectic Melt," *Acta Materialia*, vol. 59, pp. 5558-5567, 2011.
- [100] L. Gánásy, T. Pusztai, J. A. Warren, J. F. Douglas, T. Börzsönyi and V. Ferreiro, "Growth of 'dizzy dendrites' in a random field of foreign particles," *Nature Materials*, vol. 2, pp. 92-96, 2003.
- [101] B. T. Bassler, W. H. Hofmeister and R. J. Bayuzick, "The Solidification Velocity of Pure Nickel," *Materials Science and Engineering A*, vol. 342, pp. 80-92, 2003.
- [102] P. M. Nasch, M. H. Manghnani and R. A. Secco, "Sound Velocity Measurements in Liquid Iron by Ultrasonic Interferometry," *Journal of Geophysical Research*, vol. 99, no. B3, p. 4285-4291, 1994.
- [103] R. S. Hixson, M. A. Winkler and M. L. Hodgdon, "Sound Speed and Thermophysical Properties of Liquid Iron and Nickel," *Physical Review B*, vol. 42, no. 10, pp. 6485-6491, 1990.
- [104] T. Schenk, D. Holland-Moritz, V. Simonet, R. Belissent and D. M. Herlach, "Icosahedral Short-Range Order in Deeply Undercooled Metallic Melts," *Physical Review Letters*, vol. 89, no. 7, pp. 61:20-25, 2002.
- [105] Y. Ashkenazy and R. S. Averback, "Kinetic Stages in the Crystallization of Deeply Undercooled Body-Centered-Cubic and Face-Centered-Cubic metals," *Acta Materialia*, vol. 58, pp. 524-530, 2010.

- [106] Y. Mu, A. Houk and X. Song, "Anisotropic Interfacial Free Energies of the Hard-Sphere Crystal-Melt Interfaces," *Journal of Physical Chemistry B*, vol. 109, p. 6500–6504, 2005.
- [107] R. Hyers, D. M. Matson, K. F. Kelton, D. Holland-Moritz and T. Volkman, "Fluid-Flow Effects on Phase Selection and Nucleation in Undercooled Liquid Metals," *Journal of Physics: Conference Series*, vol. 327, pp. 012013:1-7, 2011.
- [108] J. Gao, M. Han, A. Kao, K. Pericleous, D. V. Alexandrov and P. K. Galenko, "Dendritic Growth Velocities in an Undercooled Melt of Pure Nickel under Static Magnetic Fields: A Test of Theory with Convection," *Acta Materialia*, vol. 103, pp. 184-191, 2016.
- [109] D. V. Alexandrov and P. K. Galenko, "Dendrite Growth under Forced Convection: Analysis Methods and Experimental Tests," *Physics Uspekhi*, vol. 57, no. 8, pp. 771-786, 2014.
- [110] K. Eckler, R. F. Cochrane, D. M. Herlach and B. Feuerbacher, "Evidence for a transition from diffusion-controlled to thermally controlled solidification in metallic alloys," *Physical Review B*, vol. 45, no. 9, pp. 5019-5022, 1992.
- [111] K. Eckler, D. M. Herlach, R. G. Hamerton and A. L. Greer, "Dendrite Growth Velocities in Highly Undercooled, Dilute Ni-C melts," *Material Science and Engineering*, vol. A, no. 133, pp. 730-733, 1991.
- [112] C. Yang, F. Liu, G. Yang and Y. Zhou, "Structure evolution upon non-equilibrium solidification of bulk undercooled Fe-B system," *Journal of Crystal Growth*, vol. 311, pp. 404-412, 2009.
- [113] M. Palumbo, G. Cacciamani, E. Bosco and M. Baricco, "Thermodynamic Analysis of Glass Formation in Fe-B System," *Calphad*, vol. 25, no. 4, pp. 625-637, 2001.
- [114] C. Yang, F. Liu, G. Yang, Y. Chen, N. Liu and Y. Zhou, "Microstructure and Phase Selection in Bulk Undercooled Fe-B Eutectic Alloys," *Journal of Alloys and Compounds*, vol. 441, no. 1-2, pp. 101-106, 2007.
- [115] L. Battezzati, C. Antonione and M. Baricco, "Undercooling of Ni-B and Fe-B alloys and their metastable phase diagrams," *Journal of Alloys and Compounds*, vol. 247, pp. 164-171, 1997.
- [116] T. V. Rompaey, K. C. H. Kumar and P. Wollants, "Thermodynamic Optimization of the B-Fe System," *Journal of Alloys and Compounds*, vol. 334, p. 173.181, 2002.
- [117] R. Trivedi and W. Kurz, "Modeling of Solidification Microstructures in Concentrated Solutions and Intermetallic Systems," *Matallurgical Transactions A*, vol. 21 A, pp. 1113-1118, 1990.
- [118] C. Yang, J. Gao, Y. K. Zhang, M. Kolbe and D. M. Herlach, "New Evidence for the Dual Origin of Anomalous Eutectic Structures in Undercooled Ni-Sn Alloys: In Situ Observations and EBSD Characterization," *Acta Materialia* 59, vol. 59, pp. 3915-3926, 2011.
- [119] N. Wang, Y. E. Kalay and R. Trivedi, "Eutectic-to-Metallic Glass Transition in the Al-Sm

- System," *Acta Materialia*, vol. 59, pp. 6604-6619, 2011.
- [120] R. Trivedi and N. Wang, "Theory of Rod Eutectic Growth Under Far-From-Equilibrium Conditions: Nanoscale Spacing and Transition to Glass," *Acta Materialia*, vol. 60, pp. 3140-3152, 2012.
- [121] I. Steinbach, "Phase-Field Models in Materials Science," *Modelling and Simulation in Materials Science and Engineering*, vol. 17, pp. 073001:1-31, 2009.
- [122] R. Trivedi and W. Kurz, "Casting and Solidification," in *Materials Processing Handbook*, Boca Raton, CRC Press, 2007, pp. 16:1-18.
- [123] D. M. Herlach and D. M. Matson, *Solidification of Containerless Undercooled Melts*, Weinheim: Wiley-VCH, 2012.
- [124] D. Y. Sun and M. Asta, "Crystal-Melt Interfacial Free Energies and Mobilities in fcc and bcc Fe," *Physical Review B*, vol. 69, 2004.
- [125] J.-H. Jeong, N. Goldenfeld and J. A. Dantzig, "Phase Field Model for Three-Dimensional Dendritic Growth with Fluid Flow," *PHYSICAL REVIEW E*, vol. 64, pp. 041602:1-14, 2001.
- [126] M. Barth, F. Joo, B. Wei and D. M. Herlach, "Measurement of the enthalpy and specific heat of undercooled nickel and iron melts," *Journal of Non-Crystalline Solids*, pp. 398-401, 1993.
- [127] O. Tolochko and J. Agren, "Thermodynamic Properties of Supercooled Fe-B Liquids - A Theoretical and Experimental Study," *Journal of Phase Equilibria*, vol. 21, no. 1, pp. 19-24, 2000.

PUBLICATION LIST

The following publications are already published/submitted including results of this thesis with permission of Prof. Dr. Dieter M. Herlach.

- [SCRIPTA MATERIALIA] W. Kuang, C. Karrasch, H. Wang, F. Liu and D. M. Herlach, "Eutectic Dendrite Growth in Undercooled Fe₈₃B₁₇ Alloy: Experiments and Modeling," *Scripta Materialia*, vol. 105, pp. 34-37, 2015.
- [IOP] C. Karrasch, T. Volkman, J. Valloton, M. Kolbe and D. M. Herlach, "Bent Dendrite Growth in Undercooled Fe-B Alloy Melts," *IOP Conference Series: Material Science and Engineering*, accepted 2014.

ACKNOWLEDGMENTS

No man is an island,

Entire of itself, ...

JOHN DONNE (1572-1631)

This thesis could not have been written without the help and support of others...

First of all, I want to thank my supervisor Prof. Dr. Dieter M. Herlach for his support and infinite patience. His experience and interest in the experimental investigations as well as discussions about modelling were extremely valuable and encouraging. He offered me the chance to work on this interesting topic and to join his group of excellent scientists. I am very thankful for the opportunity he offered me to present my scientific results in many international conferences all over the world. The participation in two parabolic flights were an awesome and unforgettable experience.

I am grateful to Prof. Dr. Kurt Westerholt to be the second referee.

I would like to thank Prof. Dr. Andreas Meyer for support and the opportunity to work at the Institute of Materials Physics in Space at the German Aerospace Center in Cologne.

I want to thank:

Dr. Thomas Volkmann as an advisor, for his help and support in experimental and theoretical questions.

Dr. Matthias Kolbe for taking SEM/EBSD images and fruitful discussions in life and science.

Dr. Jan Gegner for proofreading this thesis and using his MATLAB program to analyse videos and modelling dendrite growth velocities.

Dr. Jonas Valloton for many measurement sessions and a great time with him.

Dr. Stefan Klein for proofreading this thesis, his help and support.

Marcus Reinartz for investigations with the InfraRed-camera.

Prof. Dr. Haifeng Wang and his student Kuang Wangwang for cooperation in modelling and a lifelong treasure for me to visit Xi'An.

Prof. Dr. Jianrong Gao for the opportunity to visit and measure at the Northeastern University of Shenyang, very fruitful discussions and double checking my modelling results.

Dr. D. Holland-Moritz and Dr. P. Galenko for discussions and useful suggestions.

Raphael Kobold for being a colleague and good friend. Pierre-Yves for being a friend and office mate during our journey to become a PhD.

Ingeborg Parpart and Kim Prochnow to be the heart of our institute glueing all together.

Claudia Wulf for being an island of help and support in the ocean of RUB.

The workshop guys Matthias, Kosta, Horst and Ralf for their humor and supply of coffee in bad times.

Heliana Cardenas for her motivational friendship and proofreading for parts of this thesis.

Stefan Burggraf for being a friend in hard times, proofreading and support in sample preparation.

Simon Haßelmann for proofreading this thesis and being his best man.

This work was financially supported by the German Research Foundation DFG within contract HE1601/18 and the European Space Agency ESA under contract numbers 4200020277 and 4200014980.

Finally I would like to thank my family and friends for their support, love and never-ending patience to hear the words: "Sorry, I cannot join, I am about to finish and I have to finally work on my thesis."

Special thanks to Dr. med. Karolina Jablonska for her love, support and infinite patience.

CURRICULUM VITAE

Name: Christian Karrasch

Date of Birth: 28.06.1982

Place of Birth: Bonn-Duisdorf, Germany

Nationality: German

08/88 – 06/92 Grundschule Finkenhof, Bonn Hardtberg

06/92 – 06/98 Realschule Hardtberg, Bonn

08/98 – 29/06/01 Abitur, Helmholtz Gymnasium, Bonn

11/01– 09/02 Wehrdienst

10/02 – 27/06/11 Diploma in Physics, Rheinische Friedrich-Wilhelms-Universität Bonn. Diploma Thesis in the works of PD. Dr. R. Vianden at the Helmholtz-Institute for Radiation and Nuclear Physics: „Kristallgitterschäden durch hohe elektrische Stromdichten im III-V-Halbleiter Galliumnitrid“

02/12 - PhD Student in Physics of the Institute for Experimental Physics IV (Ruhr-Universität Bochum) of Prof. Dr. Dieter M. Herlach in cooperation with the Institute of Materials Physics in Space, German Aerospace Center (DLR) in Cologne